Theoretical Insight into the Manipulation of the Optical and Magnetic Properties of Transition-Metal-doped II-VI Semiconductor Quantum Dots

Joseph William May

A dissertation
submitted in partial fulfillment of the
requirements for the degree of

Doctor of Philosophy

University of Washington

2014

Reading Committee:

Xiaosong Li, Chair

Daniel R. Gamelin

David J. Masiello

Program Authorized to Offer Degree:
Department of Chemistry

University of Washington

Abstract

Theoretical Insight into the Manipulation of the Optical and Magnetic Properties of Transition-Metal-doped II-VI Semiconductor Quantum Dots

Joseph William May

Chair of the Supervisory Committee:
Associate Professor Xiaosong Li
Department of Chemistry

The ability to tune the electronic, magnetic, and optical properties of II-VI semiconductor quantum dots (QDs) makes these materials ideal candidates in the fabrication of new solar energy, spin electronic, and phosphorescent devices. This dissertation makes use of electronic structure theory to provide insight into the physical underpinnings of magnetic exchange and photoexcitation in Mn^{2+}- and Co^{2+}-doped CdSe and ZnO QDs. Specifically, new methods for controlling these physical effects via the incorporation of various dopants or changes in the QD's size and shape are presented. Several examples of these control techniques are discussed in this dissertation. Ferromagnetic alignment of multiple unpaired Mn^{2+} $3d$ electrons is predicted when the p-type defect N^{2-} is present in ZnO QDs. Control over the magnetic exchange interactions between charge carriers and TM^{2+} dopants that give rise to ferromagnetism is achieved by distorting the QD's shape along one or two dimensions. Aliovalent doping with Al^{3+} produces QDs that are spectroscopically identical to photochemically charged QDs, yet exhibit different reactivities. A unique temperature dependence of the luminescence and photoconductivity in large Co^{2+}-doped ZnO QDs is predicted upon excitation of its mid-gap excited state. Lastly, a new method for the optimization of transition state molecular geometries is shown to exhibit fast optimization and to be advantageous for difficult optimizations where the reaction path is flat, ideal for optimizing large QD structures.

TABLE OF CONTENTS

LIST OF FIGURES

LIST OF TABLES

GLOSSARY

AFM: antiferromagnetic

Al^{3+}:ZnO: Al^{3+}-doped zinc oxide

CB: conduction band

Co^{2+}:ZnO: Co^{2+}-doped zinc oxide

CT: charge transfer

DFT: density functional theory

DIIS: direct inversion in the iterative subspace

DMS: diluted magnetic semiconductor

DOS: density of states

d_{QD}: quantum dot diameter

e^-_{CB}: conduction-band electron

EPR: electron paramagnetic resonance

FM: ferromagnetic

gEn-DIIS: guided energy-represented direct inversion in the iterative subspace

HOMO: highest occupied molecular orbital

HS: high spin

h^+_{VB}: valence-band hole

$\mathrm{LM_{VB}CT}$: ligand-to-metal (valence band) charge transfer

LUMO: lowest unoccupied molecular orbital

$\mathrm{ML_{CB}CT}$: metal-to-ligand (conduction band) charge transfer

$\mathrm{Mn^{2+}}$:ZnO: $\mathrm{Mn^{2+}}$-doped zinc oxide

MO: molecular orbital

PES: potential energy surface

QD: quantum dot

RFO: rational function optimization

TDDFT: time-dependent density functional theory

TM: transition metal

TRM: trust radius method

TS: transition state

VB: valence band

ACKNOWLEDGMENTS

Although I would not be completing the 22nd grade without hard work, determination and, perhaps, a bit of insanity, I would not have had the opportunity if not for the many wonderful and inspiring people I have had the pleasure of getting to know along this journey. Hopefully I can get through my list before the music plays to usher me off the stage.

To Xiaosong Li I am forever grateful. As my research advisor he taught me to trust my "chemical intuition" and provided me with tremendous support in research and beyond. I also want to thank him for being such an excellent "watercooler" buddy. By the way... ***Spoiler Alert!*** "Did you see *The Walking Dead* last night? I cannot believe Rick..."

I thank my committee members, Daniel Gamelin, David Masiello, and Peter Pauzauskie, for making those closed-door sessions a little less frightening. Their expertise and insight proved to be invaluable to my work.

Continuing in reverse chronological order, I wish to thank the many members of the Li Research Group (and other theory folks) with whom I have had the pleasure of working with daily in the trenches: Erica Chong, Feizhi Ding, Sean Fischer, Joshua Goings, Patrick Lestrange, David Lingerfelt, Jonathan Litz, Phu Nguyen, Bo Peng, and Ben van Kuiken (a.k.a., Papa Bear). I would like to single out Wenkel Liang for his help and patience as I *re*-learned how to operate a computer...without a mouse; Ekateriana Badaeva for teaching me everything I know about quantum dots; and to Ekateriana and Yong Feng for their pioneering work in developing the quantum dot model used in this dissertation.

To the people who make these quantum dots for real, my collaborators, I thank members of the Gamelin Research Group: Rémi Beaulac, Liam Bradshaw, Jeffrey Rinehart, and Alina Schimpf. Without them, all of my calculations would have been for nothing.

As I leave the University of Washington to begin my career in secondary science education, I must recognize the truly gifted educators who have transformed me into the individual I am today and who will inspire me every day as a teacher. I thank the entire chemistry faculty at Southern Oregon University: Doug Chapman, Laura Hughes, Lynn Kirms, Greg Miller, Steve Petrovic, and Hala Schepmann. I also thank a few highly memorable grade school teachers: Jeanie Camarillo, Scott Dippel, Karyn Hale, and Ed Zobel.

Lastly, I thank my family: Rose, Glenn, and Jessica. Their endless love and support has driven me to pursue my passions and to always do my best to make them proud. If this doesn't do the trick...

DEDICATION

to my loving parents, Rose and Glenn

Chapter 1

INTRODUCTION

Continued advances in the development of smaller, faster computer processors; cheaper, more efficient solar energy conversion; and environmentally-conscious, high-capacity energy storage relies upon the design of new materials. Semiconducting nanocrystals such as II-VI (ZnO, CdSe, etc.) quantum dots (QDs) have shown promising application towards each of these endeavors.[1–4] They are earth-abundant and non-toxic materials with well-established engineering and manufacturing technologies. Their quantized energy levels offer opportunities for tunable electronic properties. As wide-gap semiconductors, II-VI materials are usually electronically inert. They are not photoactive in the visible spectrum and, as a result, they have not generally been suitable for photovoltaics and electrophotonics applications.

Recent innovations in experimental techniques and theoretical methods have opened a new avenue for activating II-VI nanocrystals for use in solar energy conversion,[5–13] spin electronic/photonic[3,14–17] and phosphorescent[18–20] devices, and for photocatalytic applications.[21–25] For example, the use of photochemical reduction has been shown to introduce kinetically stable, delocalized conduction band(CB)-like electrons (e^-_{CB}) into colloidal ZnO QDs.[26] Such charge carriers have been used to manipulate the magnetic properties of semiconductor QDs when transition-metal ions such as Mn^{2+} are doped into the QD lattice.[27] Nanocrystal-size-dependent electron transfer was recently observed in photochemically reduced ZnO QDs[28] and when coupled with the transfer of a proton, have been shown to catalyze redox reactions, serving as a proton-coupled electron transfer reagent.[29] Furthermore, electrically charged II-VI semiconductor nanocrystals have been successfully used in activating room-temperature magnetic

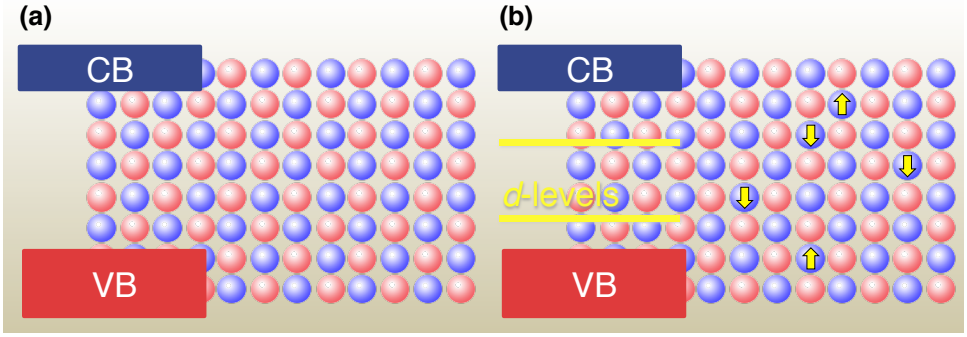

Figure 1.1. Illustration of bulk ZnO showing the composition of the lattice and the band structure around the band gap region. Pure ZnO is shown in panel (a) and TM^{2+}-doped ZnO is shown in panel (b). Blue spheres represent Zn^{2+} cations and red spheres represent O^{2-} anions. The yellow arrows indicate the spin alignment of unpaired TM^{2+} d electrons in doped ZnO.

ordering and as chemical reduction catalysts.[1,29]

Another example involves ZnO, which is unique in that the occupied Mn^{2+} $3d$ levels reside inside the semiconductor band gap (Figure 1.1) rather than deep inside the valence band (VB). This unique electronic structure gives rise to mid-gap "photoionization" or metal-to-ligand charge transfer ($ML_{CB}CT$) excited states,[7,30–33]

$$Mn^{2+} \rightarrow Mn^{3+} + e^{-}_{CB}. \tag{1.1}$$

The charge-transfer nature of the mid-gap transitions observed experimentally in Mn^{2+}:ZnO QDs is supported by a variety of spectroscopic studies.[30,34–36] Quantum confinement effects in doped QDs have been observed both theoretically and experimentally to shift semiconductor band edges relative to pinned transition metal d-levels, resulting in diameter-dependent $ML_{CB}CT$ energies.[35,37] Additionally, the dopant concentration has also been shown to affect both the energy and intensity of the $ML_{CB}CT$ and excitonic transitions in these materials.[38]

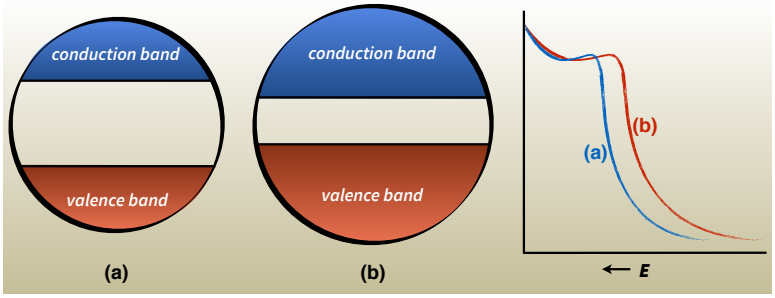

Figure 1.2. Illustration of the quantum confinement effect in quantum dots. Two QDs of increasing diameter (d_{QD}) are shown in (a) and (b). As d_{QD} increases, the separation between the VB and CB edges decreases. This decrease in the band gap energy results in a red shift of the excitonic peak (band-to-band transition) in the absorption spectrum.

1.1 Quantum Dots

In bulk semiconducting materials, the cations and anions arrange themselves into a periodic structure such as the wurtzite or zinc blende crystal structures (Figure 1.1). The individual atomic orbitals from each ion, which are nearly identical in energy, combine to form molecular orbitals that are energetically arranged into bands. Occupied molecular orbitals make up the valence band and the unoccupied orbitals give rise to the conduction band. The energy gap between these two bands is referred to as the band gap. In bulk materials the band gap energy is fixed by the composition of the material; for ZnO, the band gap is 3.37 eV and for CdSe the band gap is 1.74 eV.[39] At room temperature, k_BT is ~26 meV, meaning these materials are considered insulators. The presence of defects and/or dopants introduces new states within the band gap that increases the conductivity of these materials to that of a semiconductor.

One technique for manipulating the band structure of these materials is by reducing the dimensionality of the semiconductor lattice. This can be done in one dimension to form thin films, in two dimensions to form nanowires, or in three di-

mensions to form quantum dots. This gives rise to the so-called quantum confinement effect, wherein the energy levels of the VB and CB move in response to the change in dimensionality (Figure 1.2). As it applies to QDs, the band gap energy can be reduced via an increase in the QD's diameter (d_{QD}). Thus, using the same material, QDs with varying d_{QD} can be generated that will absorb/emit within a wide range of the ultraviolet–visible spectrum.

Electrons that have been added to or excited into the CB are delocalized over a length scale known as the Bohr radius. Confinement of e^-_{CB} in these bulk materials by reducing the dimensionality of the host semiconductor lattice serves to constrain the electrons in terms of location and energy; in effect, the electrons become quantized within the QD giving rise to the term "artificial atoms" when describing QDs. Further interpretation of the behavior of e^-_{CB} in experiment was proposed by Brus,[40–42] who treated them as non-interacting particles in a spherical potential. The solutions to this problem are the zero-order spherical Bessel functions of the first kind

$$\psi_{n\ell m}(r,\theta,\phi) = A_{n\ell} j_\ell(\beta_{n\ell} r/R) Y_\ell^m(\theta,\phi), \tag{1.2}$$

where $A_{n\ell}$ is a normalization constant, j_ℓ is the ℓ-th spherical Bessel function of the first kind, and $\beta_{n\ell}$ is the n-th zero of the ℓ-th spherical Bessel function. The energy eigenvalues given by

$$E_{n\ell} = \frac{\beta_{n\ell}\hbar^2}{m_e R^2}, \tag{1.3}$$

show that the energy is inversely proportional to the square of the QD radius. To account for the periodic potential experienced by charge carriers in a QD lattice, the effective mass theory is used. For instance, the energy of the band-to-band (excitonic) transition in a QD, which can be applied to spectral analysis,[35] is given by

$$\Delta E_{\mathrm{EXC}} = \frac{\hbar^2\pi^2}{2R^2}\left[\frac{1}{m_e^*} + \frac{1}{m_h^*}\right] - \frac{1.8e^2}{\varepsilon R} \tag{1.4}$$

where e is the electron charge, ε is the dielectric constant of the semiconductor, and m_e^* and m_h^* are the effective masses of the electron and hole, respectively. Additional details on the spherical potential model are provided in Appendix C. The model is applied to understand the absorption spectra of ZnO and Al^{3+}-doped ZnO QDs in Chapter 4, and is visually demonstrated in Figures 4.3 to 4.5.

1.2 Magnetic Exchange Interactions

Photoexcitation of Mn^{2+}–doped CdSe (Mn^{2+}:CdSe) QDs was recently shown to generate large dopant–carrier exchange fields which allow for spontaneous photoinduced polarization of Mn^{2+} spins at up to room temperature.[1] This phenomenon, known as excitonic magnetic polaron (EMP) formation, results from the interaction of a CB electron–VB hole pair (e^-_{CB}–h^+_{VB}), or exciton, with the magnetic dopant impurities. The $Mn^{2+}(3d)$–e^-_{CB} coupling (s–d exchange) and $Mn^{2+}(3d)$–h^+_{VB} coupling (p–d exchange) interactions lead to a stabilization of energy by ferromagnetically aligning the charge carriers and the unpaired Mn^{2+} $3d$ electrons.

The ordering of unpaired d electrons introduced by TM^{2+} dopants is random and not well known from experiment. In the absence of an electromagnetic field, the materials are considered paramagnetic. Application of an external magnetic field aligns the unpaired d electrons into a parallel arrangement making the material ferromagnetic (FM). As described above, the presence of charge carriers within the QD can also induce a FM alignment of the d electrons; this phenomenon results from an effect referred to as magnetic exchange. As described by Anderson,[43–45] magnetic exchange interactions come in a variety of forms: potential exchange, kinetic exchange, superexchange, and double exchange. The energies of these exchange interactions are parameterized by the exchange coupling constant J.

Potential exchange is due to the two-electron Coulomb integral,

$$J_{\mathrm{pot}} = \left\langle \psi_i(\mathbf{r}_1)\psi_j(\mathbf{r}_2) \left| (\mathbf{r}_1 - \mathbf{r}_2)^{-1} \right| \psi_j(\mathbf{r}_1)\psi_i(\mathbf{r}_2) \right\rangle , \tag{1.5}$$

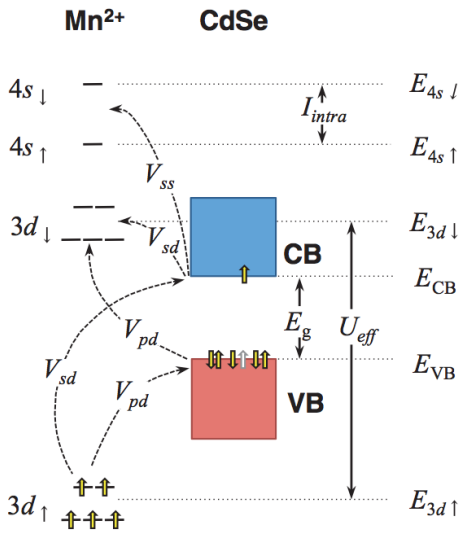

Figure 1.3. Illustration of the energy levels involved in Mn^{2+}-carrier magnetic exchange in $Cd_{1-x}Mn_xSe$ QDs. The Mn^{2+} $4s$ orbital may lie below the empty $3d$ orbitals. Adapted from Reference 49.

arising from the Pauli exclusion principle and always gives rise to FM interactions. The Mn^{2+}-e^-_{CB} coupling has long been attributed to this exchange mechanism and is due to the interaction between an s-like e^-_{CB} and the TM^{2+} d electrons[46,47] giving rise to the term "s–d exchange". However, it has recently been shown in Mn^{2+}:CdSe QDs that the FM Mn^{2+}-e^-_{CB} interactions are the result of s–s kinetic exchange (described below) involving partial spin transfer from the CB to the empty Mn^{2+} $4s$ orbital.[48,49]

Kinetic exchange results from partial transfer of spin density between two magnetic centers, and is usually treated perturbatively:[50,51]

$$J_{\text{kin}} = \sum_{ij} C_{ij} \frac{h_{ij}^2}{\Delta E_{i \to j}}, \tag{1.6}$$

where C_{ij} is a constant dependent on the orbital pathway, h_{ij} is the transfer integral describing the mixing between the two magnetic centers, and $\Delta E_{i \to j}$ is the energy associated with complete transfer of an electron from one center to the other. The

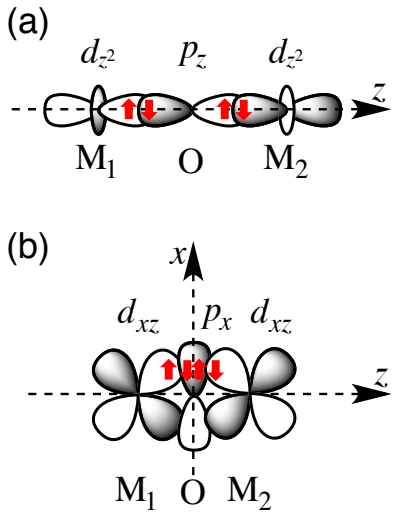

Figure 1.4. Illustration of the superexchange mechanism in an M_2O system in which each transition metal ion M has a single *d*-electron. In (a) the σ-bonding mechanism is shown and in (b) the π-bonding mechanism is shown. Both cases lead to AFM alignment of the unpaired spins on M_1 and M_2. Adapted from Reference 52.

sum is taken over all relevant orbital pathways but is most strongly influenced by the lowest energy pathways. Kinetic exchange can lead to either FM or antiferromagnetic (AFM) spin alignment and is generally the dominate exchange mechanism. The Mn^{2+}-h^+_{VB} coupling arises from this exchange mechanism due to the transfer of spin density from the half-filled TM^{2+} *d*-orbitals into a half-filled VB *p*-orbital giving rise to the term "*p*–*d* exchange", which must involve AFM spin alignment in this case. An illustration of the orbital exchange pathways in a TM^{2+}-doped QD is provided in Figure 1.3.

The superexchange mechanism involves the interaction of electrons with opposite spins on two interacting magnetic ions via an intermediate diamagnetic anion.[52] This mechanism involves orbital overlap with the filled orbitals on the intervening anion and always results in AFM spin alignment (Figure 1.4). These interactions are short ranged occurring only when the magnetic ions are nearest neighbors.[27,53]

Lastly, the double exchange mechanism involves mixed valence magnetic ions. In this case, spin coupling occurs via the transfer of an extra electron between the two magnetic centers and is expected to give rise to FM coupling of the spins.[45,54] This phenomenon has been observed in Mn^{2+}-doped ZnO QDs, in which the double exchange mechanism was shown responsible for the observed spin-dependent hole delocalization upon excitation of the $ML_{CB}CT$ excited state resulting in FM alignment of the Mn^{2+} $3d$ spins.[36] Recent work has involved an analysis of the charge carrier relaxation dynamics in ZnO and Mn^{2+}:ZnO QDs to study the formation of the $ML_{CB}CT$ state following photoexcitation of the band-to-band transition and the subsequent relaxation to the ground state.[55] An understanding of the relaxation dynamics and the spin-ordering times is essential in the application of these materials as controllable magnets.

1.3 Overview

This dissertation focuses on the application of computational chemistry to the understanding of the physical underpinnings of magnetic exchange interactions and the absorption spectra of TM^{2+}-doped II-IV semiconductor quantum dots. It aims to provide insight into the fundamental interactions that exist within these systems that will give experimentalists fine control over the optical and magnetic properties of these materials.

In Chapter 2, the magnetic exchange interactions between paramagnetic Mn^{2+} dopants in the presence of a N^{2-} p-type defect in ZnO QDs are studied using density functional theory (DFT). Analytical expressions are derived and supported by DFT calculations that show that the N^{2-} concentration has a stronger influence on the magnetic splitting compared with that of the Mn^{2+} concentration.

The roles of nanocrystal shape and crystalline anisotropy on carrier-mediated magnetism in diluted magnetic semiconductor (DMS) nanocrystals are examined in Chapter 3. A combination of DFT and analytical perturbation theory are used to

investigate the electronic structures of Mn^{2+}-doped nanocrystals of varied shapes and sizes.

The experimental absorption spectra of photochemically reduced ZnO and Al^{3+}-doped ZnO quantum dots are indistinguishable. In Chapter 4 it is shown, using time-dependent DFT (TDDFT), that despite these spectroscopic similarities, the band structure of these materials may not be as similar as previously thought.

The electronic characteristics of mid-gap transitions in Co^{2+}-doped ZnO QDs are not fully understood, and the uncertain interplay between these transitions has led to disagreement in the literature. In Chapter 5, mid-gap excited states of Co^{2+}-doped ZnO QDs are analyzed using linear response TDDFT and the effective mass theory with a focus on the geometry relaxation in the donor-type photoionization excited state.

Lastly, in Chapter 6, a transition state optimization method using a guided energy-represented direct inversion in the iterative subspace (gEn-DIIS) algorithm is introduced and compared with the quasi-Newton rational function optimization (RFO) method. A hybrid technique that employs a combination of RFO and guided DIIS methods at various stages of convergence is presented. A set of test molecules that includes a 1.2-nm $Cd_{33}Se_{33}$ nanocrystal is optimized for comparison using the hybrid method with gEn-DIIS and the traditional RFO methods.

Chapter 2

FERROMAGNETISM IN P-TYPE MANGANESE-DOPED ZINC OXIDE QUANTUM DOTS

The magnetic exchange interactions between paramagnetic Mn^{2+} dopants in the presence of a N^{2-} p-type defect in zinc oxide quantum dots are studied using density functional theory. Spin-dependent delocalization of the N^{2-} $2p$ acceptor level among the nearest-neighbor Mn^{2+} dopants is observed. The calculations show that parallel Mn^{2+} spin alignment is favored upon the formation of a nitrogen-bridged Mn–Mn dimer. Although the effect is short-ranged, the observed magnitude of stabilization of the ferromagnetic alignment of nearest-neighbor Mn^{2+} spins arises from p–d exchange and suggests p-type Mn^{2+}-doped ZnO quantum dots as excellent candidates for exhibiting room-temperature ferromagnetism. Analytical expressions are derived and supported by density functional theory calculations that show that the N^{2-} concentration has a stronger influence on the magnetic splitting compared with that of the Mn^{2+} concentration. The work presented in this chapter is reproduced with permission from May, J. W.; McMorris, R. J.; Li, X. *J. Phys. Chem. Lett.* **2012**, *3*, 1374–1380.

2.1 Introduction

Semiconducting nanostructures doped with transition metal (TM) ions such as Mn^{2+}-doped ZnO (Mn^{2+}:ZnO) quantum dots (QDs) have been the subject of intense experimental and theoretical investigation for their potential use in spin-electronic and spin-photonic devices.[2–4,56–59] The interplay between localized magnetic impurities and delocalized charge carriers via magnetic exchange interactions gives rise to prop-

erties such as giant Zeeman and Faraday rotation effects distinct to these diluted magnetic semiconductor (DMS) materials.[46,47,60] Recent studies have examined ways in which either carrier spin polarizations or the spins of the magnetic dopants themselves may be manipulated.[1,61,62] These control techniques are based on fundamental magnetic exchange interactions between dopant unpaired spins and charge carriers. In particular, the interaction between a valence band (VB) hole (h^+_{VB}) and magnetic dopants in a DMS QD is known to have a strong magnetic exchange effect.

We recently reported on the observation of spin-dependent hole delocalization among Mn^{2+} dopants in the donor-type charge transfer (CT, "photoionization", or $ML_{CB}CT$) excited states of Mn^{2+}:ZnO QDs that favored parallel Mn^{2+} spin alignment.[36] Given that typical DMS spin ordering times are on the order of only a few hundred picoseconds under *p–d* exchange fields,[1,63,64] ferromagnetic (FM) ordering of Mn^{2+} spins in these CT excited states will be relatively short-lived. However, high-T_C ferromagnetism was observed in 0.20% Mn^{2+}:ZnO nanocrystals (diameter ∼6 nm) capped with dodecylamine (N-capped).[7,65] It was hypothesized that calcination of the surface-capping amines left behind nitrogen that could serve as a p-type defect.[30]

Room-temperature ferromagnetism in p-type zinc-blende materials was first predicted by Dietl,[59] in which it was proposed that nitrogen hole carriers could mediate the exchange interaction with the localized spins of TM dopants. To simulate p-type doping in bulk Mn^{2+}- and Co^{2+}-doped ZnO, Spaldin[66] introduced Zn^{2+} vacancies in the crystal lattice, which stabilized the FM configuration. This observation led to the conclusion that p-type carriers must be included to observe ferromagnetism in these materials. However, Sharma and coworkers[67] observed FM ordering in bulk ZnO with low (<4%) Mn concentrations when the films were prepared at low temperature. The manner by which nitrogen concentration affects FM stability is contentious, with Sato and Katayama-Yoshida[68] predicting an increase in stability with an increase in the nitrogen concentration (up to a point) and Maouche et al.[69] predicting the stability to decrease with increasing concentration. Although, Wang et al.[70] and Petit et al.[71,72]

reach agreement in suggesting that the concentration of nitrogen must be greater than the TM-dopant concentration to observe ferromagnetism in bulk Mn^{2+}:ZnO.

To probe the physical underpinnings of the exchange interaction between the N^{2-} and Mn^{2+} dopants in the presence of a semiconductor band-like electronic structure, we have performed density functional theory (DFT) calculations on Mn^{2+}:ZnO QDs with the added p-type dopant, nitrogen. These materials are unique for their quantum confinement effects, which allow the optical, electronic, and magnetic properties to be tuned via the diameter of the QD. For the case of a nitrogen-bridged Mn^{2+} dimer (Mn–N–Mn), the interaction among three spin centers is observed to give rise to three unique spin states that could provide use in increasing the memory storage or processing capabilities of spin-electronic devices. We present analytical expressions and DFT calculations to obtain a fundamental understanding of the effect of p-type dopants in DMS QDs.

2.2 Results and Discussion

DFT calculations were performed on $Mn_mZn_{84-m}N_nO_{84-n}$ QDs (where $m = 0$–4 and $n = 0$–4) of diameter ∼2.0 nm. The p-type defect was introduced by substituting an O^{2-} ion at a lattice position near the center of the QD with a N^{2-} ion. The paramagnetic Mn^{2+} dopants were then positioned at nearest-neighbor Zn^{2+} lattice sites to form a Mn–Mn dimer with a nitrogen bridge. The energies and electronic structures for these $Mn_mZn_{84-m}N_nO_{84-n}$ QDs were computed at the PBE1PBE/LANL2DZ level of theory by solving the Kohn-Sham equations to self-consistency. (For more information, see Chapter 2.4.)

Figure 2.1a,b shows the density-of-states (DOS) diagrams calculated for a $MnZn_{83}O_{84}$ QD and a $Zn_{84}NO_{83}$ QD obtained using one-electron orbitals from DFT ground-state calculations. Figure 2.1a shows an orbital energy gap of ∼5.2 eV between the VB and conduction band (CB) of ZnO. This energy gap is larger than the bulk band gap of ∼3.4 eV due to quantum confinement and lack of electron-hole binding energy.[73] De-

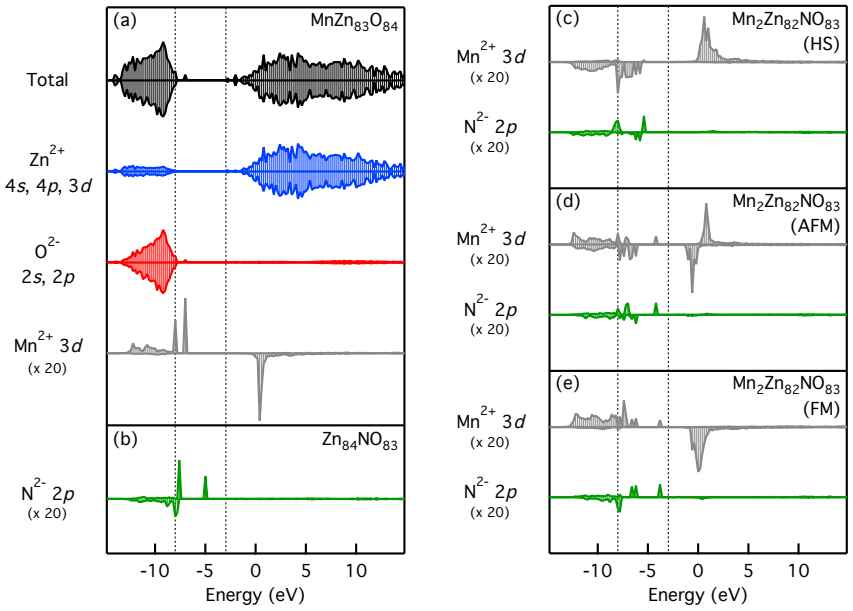

Figure 2.1. Density-of-states (DOS) diagrams for (a) a $MnZn_{83}O_{84}$ QD, (b) a $Zn_{84}NO_{83}$ QD, (c) a $Mn_2Zn_{82}NO_{83}$ QD in the high-spin configuration, (d) a $Mn_2Zn_{82}NO_{83}$ QD in the antiferromagnetic configuration, and (e) a $Mn_2Zn_{82}NO_{83}$ QD in the ferromagnetic configuration showing the total and projected DOS plotted as the number of one-electron orbitals within a bin size of $\Delta E = 0.2$ eV. The total DOS and the Zn^{2+} and O^{2-} projected DOS are shown only once for the $MnZn_{83}O_{84}$ QD in panel a because their general features do not change due to the incorporation of N^{2-} or an additional Mn^{2+} into the host semiconductor lattice. Note the $20\times$ magnification of the N^{2-} and Mn^{2+} projected DOS. Spin-up and spin-down densities are plotted as positive and negative values, respectively. The vertical lines indicate the energy position of the VB and CB edges.

composition of the total densities into individual atomic orbital contributions shows that the VB is formed primarily from O^{2-} $2p$ orbitals, whereas the CB consists predominantly of a mixture of Zn^{2+} $4s$ and $4p$ orbitals. The occupied Mn^{2+} $3d$ orbitals are localized at the top edge of the VB and are split into e and t_2 sets separated by $\sim$1 eV due to the pseudotetrahedral crystal field of the wurtzite structure. This description agrees well with photoelectron spectra[31,74] and with recent LSDA+U calculations on Mn^{2+}:ZnO.[75] The unoccupied Mn^{2+} $3d$ levels are found at $\sim$3 eV above

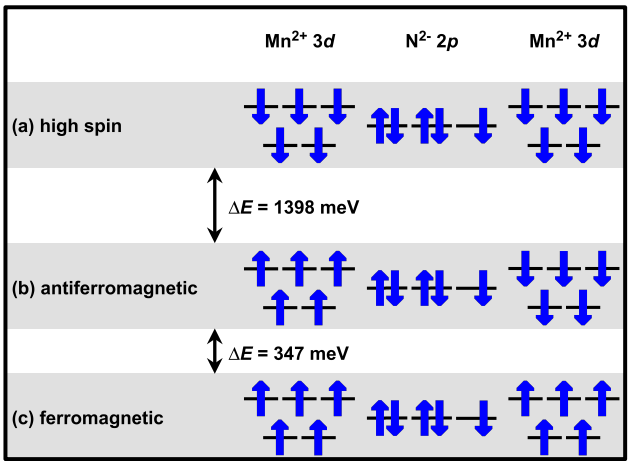

Figure 2.2. Energy splitting schematic of the (a) high-spin, (b) antiferromagnetic, and (c) ferromagnetic spin configurations of Mn^{2+} $3d$ and N^{2-} $2p$ electrons with the two Mn^{2+} ions in the nearest-neighbors arrangement.

the CB edge. From the ground-state electronic structure point of view, an increase in the number of Mn^{2+} dopants yields an increase in the density of the Mn^{2+} $3d$ levels (Figure 2.1c–e) and can lead to d-band broadening as a result of the Coulomb and exchange interactions between Mn^{2+} ions.[27] In the absence of Mn^{2+}, the occupied N^{2-} $2p$ orbitals reside near the top edge of the VB with the spin-down $2p$ orbitals more delocalized throughout the VB than the spin-up $2p$ orbitals for which the N^{2-} $2p_x$ and $2p_y$ orbitals are localized at the top edge of the VB (Figure 2.1b). The peak at $\sim$3 eV above the VB results from the unoccupied N^{2-} $2p_z$ orbital. This empty band gives rise to a midgap acceptor level introduced by a p-type dopant.

With the incorporation of two high-spin (HS) ($S_{\mathrm{Mn}} = 5/2$) Mn^{2+} dopants together with a nitrogen defect, three unique spin configurations arise (Figure 2.2) and were considered in this work. The HS configuration corresponds to a total spin of $S_T = 11/2$, where all the unpaired Mn^{2+} $3d$ electrons and the unpaired N^{2-} $2p$ electron are aligned parallel (Figure 2.2a). The FM configuration corresponds to $S_T = 9/2$, where all of the Mn^{2+} $3d$ electrons are aligned antiparallel with the spin of the unpaired

N^{2-} $2p$ electron (Figure 2.2c). Lastly, when the d electrons that belong to different dopant centers are aligned in opposite spin orientations, the electronic state, for which $S_T = 1/2$, is defined as the antiferromagnetic (AFM) configuration (Figure 2.2b). For each configuration, the Mn^{2+} dopants were positioned at nearest-neighbor Zn^{2+} lattice sites, where the exchange interactions are known to be the strongest, to form a nitrogen-bridged Mn–Mn dimer.

Figure 2.1c–e shows the partial DOS for Mn^{2+} $3d$ and N^{2-} $2p$ electron distributions in the HS, AFM, and FM configurations defined above, respectively. The occupied set of spin-down N^{2-} $2p$ orbitals delocalizes throughout the VB, whereas the partially occupied spin-up N^{2-} $2p$ manifold is localized at the top edge of the VB. The empty midgap acceptor level is shifted to ∼4 eV above the VB in the AFM and FM configurations. This shift is a result of hybridization of N^{2-} $2p$ and Mn^{2+} $3d$ levels. DOS analysis suggests that there is ∼25% Mn^{2+} $3d$ character in this empty midgap level. Accompanied by a blue shift of the empty acceptor level as a result of hybridization is the stabilization of the occupied Mn^{2+} $3d$ levels.

The relative energy differences between these three spin configurations of the $Mn_2Zn_{82}NO_{83}$ QD were calculated and are summarized in Figure 2.2. This scheme shows that the AFM configuration is stabilized by 1398 meV to lower energy with respect to the HS configuration. The FM configuration is stabilized by an additional 347 meV to lower energy for a total stabilization of 1745 meV with respect to the HS configuration. If the spin-spin interaction is the same in all three configurations considered here, then Hund's rule suggests that the configuration with the highest multiplicity (the HS configuration) should be the most stable; thus, different exchange mechanisms must exist between the Mn^{2+} and N^{2-} dopants to account for the observed stabilization and energy difference of the AFM and FM configurations.

In the perturbative limit, the interaction between two spin subsystems can be parametrized by the Heisenberg-type spin Hamiltonian (or Heisenberg-Dirac-Van

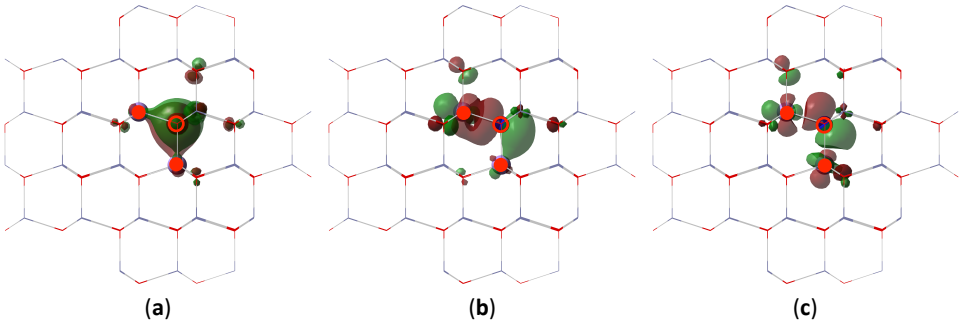

Figure 2.3. Molecular orbital (MO) diagrams of the unoccupied N^{2-} $2p$ orbital (acceptor level wave function) for $Mn_2Zn_{82}NO_{83}$ QDs with Mn^{2+} dopants in the nearest-neighbors arrangement and the unpaired Mn^{2+} and N^{2-} electrons in (a) the high-spin configuration, (b) the antiferromagnetic configuration, and (c) the ferromagnetic configuration. The red closed and open circles indicate the Mn^{2+} and N^{2-} dopants, respectively. The MOs were plotted with an isosurface value of 0.04.

Vleck, or Kondo spin Hamiltonians) of Equation (2.1)

$$\hat{H} = -2J\hat{S}_i \cdot \hat{S}_j \tag{2.1}$$

where $\hat{S}_i$ is the spin operator of the ith spin subsystem and J is the exchange coupling constant. In the case of a Mn–N–Mn three-center interaction, two fundamental exchange interactions can be identified. The interaction between the two Mn^{2+} centers arises from the well-known superexchange mechanism (J_{SE}), which favors the AFM alignment of two Mn^{2+} ions.[27,47,53] The underlying interaction mechanism between Mn^{2+} and N^{2-} unpaired spins is the kinetic p–d exchange (J_{p-d}), which also favors the AFM alignment of the Mn^{2+} $3d$ electrons and the unpaired electron of N^{2-}. The p–d exchange mechanism discussed here is similar to the interaction between a h^+_{VB} and a magnetic TM-dopant.[47,60] The electronic characteristics of p–d exchange is the wave function hybridization of Mn^{2+} $3d$ and N^{2-} $2p$ electrons, as indicated in Figure 2.3b. In a $Mn_2Zn_{82}NO_{83}$ QD, where Mn^{2+} ions are positioned as nearest-neighbors in the nitrogen-bridged dimer, both superexchange and p–d exchange mechanisms coexist

in all of the spin configurations considered here.

In the FM configuration, additional exchange mechanisms may also exist. If the hole is trapped at a dopant center or if charge transfer occurs from the dopant to the p-type defect, resulting in a Mn^{3+} charge state, the interaction between Mn^{2+} and Mn^{3+} centers gives rise to double exchange, which is a non-Heisenberg mechanism.[45,54,68] As reported in our previous study,[36] hole delocalization over multiple Mn^{2+} dopants in the $ML_{CB}CT$ excited state was responsible for stabilizing the FM configuration of Mn^{2+} spins via the double-exchange mechanism.[45,54] The double-exchange phenomenon arises when the acceptor level is lower in energy than Mn^{2+} $3d$ levels. The same effect may occur here to account for the stabilization of the FM configuration due to delocalization of the N^{2-} $2p$ acceptor level over the Mn^{2+} dopants. Figure 2.3c plots the molecular orbital (MO) of the acceptor level for the FM spin configuration of the $Mn_2Zn_{82}NO_{83}$ QD. In the FM configuration, the acceptor level is now aligned parallel with respect to the Mn^{2+} $3d$ electrons, allowing for delocalization of the acceptor level onto both Mn^{2+} ions. However, as suggested by Figure 2.3c, this acceptor level is still dominated by N^{2-} $2p$ character with contributions of more than 75% from the empty N^{2-} $2p$ orbital. In other words, Mn^{2+} dopants are still in the +2 charge state. This is understandable because the acceptor level is higher in energy than the Mn^{2+} $3d$ levels, as shown in Figure 2.1e. This observation suggests that the double-exchange mechanism can be considered to be absent in the FM configuration of a $Mn_2Zn_{82}NO_{83}$ QD.

Following from the above discussions, Equation (2.1) can be extended to describe the exchange coupling involving interacting unpaired spins on three different atomic centers

$$\hat{H} = -2J_{\mathrm{SE}}\hat{S}_{\mathrm{Mn_1}} \cdot \hat{S}_{\mathrm{Mn_2}} - 2J_{p-d}\hat{S}_{\mathrm{Mn_T}} \cdot \hat{S}_{\mathrm{N}} \tag{2.2}$$

where J_{SE} and J_{p-d} are the superexchange and carrier-dopant exchange coupling constants, respectively, and $\hat{S}_{\mathrm{Mn_T}}$ is the total spin of the Mn^{2+} dopants. Because both

the superexchange and kinetic p–d exchange mechanisms favor the AFM interactions, a spin-frustrated situation arises in this three-center spin-exchange scenario; that is, all AFM interactions cannot be satisfied simultaneously. The relative splitting energies among the HS and AFM configurations, the AFM and FM configurations, and the HS and FM configurations are

$$\Delta E_{\text{HS–AFM}} = -30J_{\text{SE}} - 5J_{p-d} \tag{2.3}$$

$$\Delta E_{\text{AFM–FM}} = 30J_{\text{SE}} - 6J_{p-d} \tag{2.4}$$

$$\Delta E_{\text{HS–FM}} = -11J_{p-d} \tag{2.5}$$

and were obtained from Equation (2.2) using $-2\hat{S}_i \cdot \hat{S}_j = S_i^2 + S_j^2 - (S_i + S_j)^2$, $S_{\text{Mn}} = 5/2$, and $S_{\text{N}} = 1/2$. We refer the reader to Chapter 2.5 for further details on the derivation of Equations (2.3) to (2.5). Using the energy diagram in Figure 2.2, J_{p-d} and J_{SE} are calculated to be -159 and -20 meV, respectively. The analysis suggests that the p–d exchange mechanism is mainly responsible for the stabilization of the FM configuration over the HS configuration. Although the superexchange disfavors the spin alignment between Mn^{2+} ions in the FM state compared with that in the AFM state, the additional strong p–d exchange contribution in the FM state between the Mn^{2+} and the empty acceptor level gives rise to the extra stability of the FM configuration over the AFM configuration. To ensure that the observed stabilization of the FM configuration was due to the presence of N^{2-}, this substitutional-defect ion was replaced with the original O^{2-} ion to create a Mn–O–Mn dimer separated by an oxygen bridge. In this arrangement, superexchange coupling stabilizes the AFM configuration by ∼50 meV to lower energy. Without the acceptor level for Mn^{2+} $3d$ electrons to delocalize into, an antiparallel alignment of spins is favored, allowing for delocalization of Mn^{2+} $3d$ electrons from one dopant into the unoccupied $3d$ orbitals of the other Mn^{2+} dopant and vice versa.

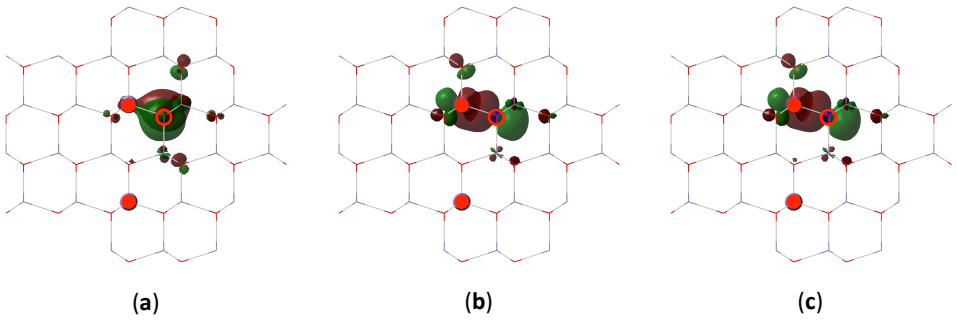

Figure 2.4. Molecular orbital (MO) diagrams of the unoccupied N^{2-} $2p$ orbital (acceptor level wave function) for $Mn_2Zn_{82}NO_{83}$ QDs with Mn^{2+} dopants in the second nearest-neighbors arrangement and the unpaired Mn^{2+} and N^{2-} electrons in (a) the high-spin configuration, (b) the antiferromagnetic configuration, and (c) the ferromagnetic configuration. The red closed and open circles indicate the Mn^{2+} and N^{2-} dopants, respectively. The MOs were plotted with an isosurface value of 0.04.

The strength of exchange coupling depends on the inter-Mn and Mn–N internuclear separation. The relative energy differences between the respective spin configurations in the $Mn_2Zn_{82}NO_{83}$ QD with Mn^{2+} ions at second-nearest neighbor sites were calculated. In second-nearest neighbor sites, the AFM and FM configurations are degenerate, each stabilized by 1269 meV to lower energy with respect to the HS configuration (all spins aligned parallel). This observation suggests that the superexchange coupling $J_{\mathrm{SE}} = 0$ when the dopants are not in the dimer arrangement, and one of the p–d exchange couplings also becomes zero when Mn^{2+} and N^{2-} are nonbonding. The superexchange mechanism is known to be effective only when magnetic ions are in the nearest-neighbor sites.[27,47,53] Considering that h^{+}_{VB}-induced p–d exchange is known to affect all dopant positions in a small QD, it is a surprise to see that the N^{2-} $2p$-induced p–d exchange is short-ranged, affecting only the nearest tetrahedron of the N^{2-} defect site. The DOS in Figure 2.1 suggests that the acceptor level introduced by N^{2-} is energetically isolated from both the VB and CB of ZnO, suggesting that delocalization of the acceptor level via the VB or CB is unlikely. In addition,

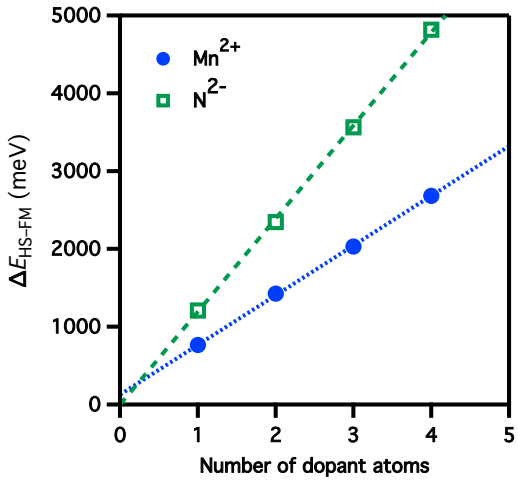

Figure 2.5. Exchange splitting energies between the HS (all unpaired spins of one dopant type aligned parallel to the unpaired spin(s) of the other dopant type) and FM (all unpaired spins of one dopant type aligned antiparallel to the unpaired spin(s) of the other dopant type) configurations of increasing Mn^{2+} dopants around N^{2-} (filled blue circles) and increasing N^{2-} dopants around Mn^{2+} (open green squares). The dotted and dashed lines represent fits to the Mn^{2+} and N^{2-} data using Equations (2.6) and (2.7), respectively. Because of the wurtzite crystal structure of the QDs, the four positions around the tetrahedrally coordinated dopants are not all equivalent with one axial bond longer than the other three equatorial bonds of equal length. Therefore, we average the splitting energy over all possible arrangements of dopants in the axial and equatorial positions to generate a point for a given number of Mn^{2+} or N^{2-}. Therefore, the p–d exchange coupling obtained from the data fits is an average.

the analysis of the electronic wave functions in Figure 2.4 shows that the empty N^{2-} $2p$ level is localized within the first tetrahedron near the p-type defect. As a result, the N^{2-} $2p$-induced p–d exchange is short-ranged, affecting only the nearest-neighbor Mn^{2+} ions.

We extend the discussion above to study the concentration effect by introducing multiple Mn^{2+} dopants around the first tetrahedron of a N^{2-} dopant and, similarly, multiple N^{2-} dopants around the first tetrahedron of a Mn^{2+} dopant, both near the center of the QD. The two spin states considered are the HS configuration, where all unpaired Mn^{2+} (N^{2-}) spins are aligned parallel to the N^{2-} (Mn^{2+}) unpaired spin(s), and the FM configuration, where all unpaired Mn^{2+} (N^{2-}) spins are aligned antipar-

allel to the N^{2-} (Mn^{2+}) unpaired spin(s). Figure 2.5 shows the dependence of the exchange splitting energies between the HS and FM configurations on the number of Mn^{2+} or N^{2-} dopants. To obtain an expression for the exchange splitting energies, we again consider these Mn–N moieties to be interacting spin systems. For the case of M number of Mn^{2+} dopants around one N^{2-}, we obtain Equation (2.6)

$$\Delta E^{\mathrm{Mn}}_{\mathrm{HS–FM}} = -(5M+1)\bar{J}_{p-d} \tag{2.6}$$

and for N number of N^{2-} dopants around one Mn^{2+}, we obtain Equation (2.7)

$$\Delta E^{\mathrm{N}}_{\mathrm{HS–FM}} = -6N\bar{J}_{p-d} \tag{2.7}$$

where $\bar{J}_{p-d}$ is the average p–d exchange coupling. (See Chapter 2.5 for the derivations of Equations (2.6) and (2.7).) The trend of magnetic splitting as a function of the dopant concentration predicted by Equations (2.6) and (2.7) are very well reproduced by the DFT calculations in Figure 2.5, confirming that the dominant mechanism for the observed magnetic ordering is the p–d exchange between N^{2-} and Mn^{2+} ions. Fitting Equations (2.6) and (2.7) to their respective data sets in Figure 2.5, we obtain average values for $\bar{J}_{p-d}$ of -128 and -199 meV, respectively. These values agree in sign, but are considerably smaller in magnitude, with the experimentally determined h^{+}_{VB}-induced p–d exchange constants for similar Mn^{2+}-doped II-VI DMSs (-1220 meV)[76,77] obtained from band-edge spin-splittings in the presence of a magnetic field. This difference is attributed to the very localized nature of the acceptor level, or hole wave function, about the N^{2-} dopant. Figure 2.5 and Equations (2.6) and (2.7) suggest that the N^{2-} concentration has a stronger effect (larger linear slope) on the exchange splitting energy. This observation lends a way to control the magnetic splitting by adjusting the concentration of the magnetic ions and p-type defects even though the interaction is short-ranged.

2.3 Conclusions

In summary, dopant-defect interactions between Mn^{2+} and N^{2-} unpaired electrons through the *p*–*d* exchange mechanism were observed upon the formation of a nitrogen-bridged Mn–Mn dimer, which favored parallel spin alignment of the unpaired Mn^{2+} $3d$ electrons despite the competing presence of AFM superexchange coupling. Whereas the FM ordering observed in the CT state of Mn^{2+}:ZnO QDs was short-lived,[36] the permanent hole introduced by nitrogen results in a stable FM ground state. Delocalization of the N^{2-} acceptor level among nearest-neighbor Mn^{2+} dopants favored the FM configuration with respect to the AFM configuration, making p-type Mn^{2+}:ZnO QDs suitable materials for exhibiting room-temperature ferromagnetism. Analytical expressions and DFT calculations support the fact that the N^{2-} concentration has a stronger effect on the magnetic splitting compared with that of the Mn^{2+} concentration. This observed phenomena can be related to proposals of bound magnetic polarons (BMPs), impurity bands, and ferromagnetism in bulk $Zn_{1-x}Mn_xO$ and some bulk manganese-doped III-V DMSs.[78] Compared with the BMP induced by a charge carrier, such as a VB hole or an exciton,[1,76] the p-type acceptor introduced by a N^{2-} dopant is very short-ranged, affecting only the nearest-neighbor magnetic ions. These findings support the proposed formation of a magnetic impurity band resulting from manganese-based hole delocalization in bulk p-$Zn_{1-x}Mn_xO$[7,68,70] and adds p-type Mn^{2+}:ZnO QDs to a growing class of materials with controllable room-temperature ferromagnetism.[79,80]

2.4 Theoretical Methods

Quasi-spherical $Mn_mZn_{84-m}N_nO_{84-n}$ QDs (where $m = 0$–4 and $n = 0$–4) were constructed using the bulk ZnO wurtzite crystal structure with lattice parameters $a = 3.249$ Å, $c = 5.204$ Å, and $u = 0.382$.[81] Each QD has C_{3v} symmetry in the absence of Mn^{2+} and N^{2-}.[82] The effective diameter of the QD is ∼2.0 nm. This diame-

ter is similar to that of the smallest ZnO QDs typically obtainable from molecular beam epitaxy[83] and colloidal synthesis techniques[30,84–86] and represents ZnO in the strong quantum confinement regime (ZnO exciton Bohr radius a_0 = 1.3–2.5 nm).[87–89] Pseudohydrogen atoms with nuclear charges of +1.5 and +0.5 were used to passivate uncompensated surface Zn^{2+} and O^{2-} ions (dangling bonds) by the formation of fully optimized Zn–H and O–H bonds, according to the scheme described in the recent literature.[90–92] This pseudohydrogen capping leads to a well-defined band gap and stable QD geometry. Substitution of Mn^{2+} and N^{2-} dopants for the Zn^{2+} and O^{2-} ions, respectively, retains the overall neutral charge of the QDs. All DFT calculations were performed with the development version of the Gaussian program.[93] Ground-state energies and electronic structures were obtained by solving the Kohn-Sham equations self-consistently using the PBE1PBE hybrid functional[94–96] with the LANL2DZ basis set,[97–99] in which core electrons are replaced by an effective core potential, and only Zn^{2+} (4s, 3d, 4p), O^{2-} (1s, 2s, 2p), Mn^{2+} (3s, 3p, 4s, 3d, 4p), N^{2-} (1s, 2s, 2p) and H (1s) electrons are described with explicit basis functions. This computational scheme has been successful in describing the electronic structure of TM-doped ZnO QDs ($Zn_{1-x}TM_xO$, where TM = Co^{2+}, Mn^{2+}).[35,90]

2.5 Supplement: Derivation of the Relative Splitting Energies

This supplemental information section contains the derivation of Equations (2.3) to (2.7).

The Heisenberg-type spin Hamiltonian

$$\hat{H} = -2J\hat{S}_i \cdot \hat{S}_j \tag{2.8}$$

describes the interaction between unpaired spins on two sub-systems, $\hat{S}_i$ and $\hat{S}_j$. Equation (2.8) can be extended to describe the interacting spin system of the nitrogen-

Table 2.1. Description of the spin configurations for the Mn–N–Mn dimer. The second column shows the alignment of unpaired Mn^{2+} and N^{2-} spins as spin-up (↑) or spin-down (↓).

Configuration		S_{Mn_1}	S_{Mn_2}	S_{Mn_T}	S_N	S_T
HS	$Mn_1(\downarrow)$–$N(\downarrow)$–$Mn_2(\downarrow)$	5/2	5/2	5	1/2	11/2
AFM	$Mn_1(\uparrow)$–$N(\downarrow)$–$Mn_2(\downarrow)$	5/2	5/2	0	1/2	1/2
FM	$Mn_1(\uparrow)$–$N(\downarrow)$–$Mn_2(\uparrow)$	5/2	5/2	5	1/2	9/2

bridged Mn–Mn dimer (Mn–N–Mn),

$$\hat{H} = -2J_{SE}\hat{S}_{Mn_1}\cdot\hat{S}_{Mn_2} - 2J_{p-d}\hat{S}_{Mn_T}\cdot\hat{S}_N \tag{2.9}$$

where J_{SE} is the exchange coupling constant describing the superexchange coupling between two Mn^{2+} ions, J_{p-d} is the exchange coupling constant describing the kinetic p–d exchange between the interacting Mn^{2+} spin system and the nitrogen acceptor level (hole), $\hat{S}_{Mn_1}$ and $\hat{S}_{Mn_2}$ are the spin operators for two individual Mn^{2+} ions, $\hat{S}_{Mn_T}$ is the total spin operator of the interacting system of Mn^{2+} ions, and $\hat{S}_N$ is the spin operator of the N^{2-} dopant.

For the Mn–N–Mn dimer, three unique spin configurations arise: the high-spin (HS), antiferromagnetic (AFM), and ferromagnetic (FM) configurations. Each of these configurations is summarized in Table 2.1.

Equation (2.9) and the data in Table 2.1 are used to derive the exchange splitting energies $\Delta E_{HS\text{–}AFM}$, $\Delta E_{AFM\text{–}FM}$, and $\Delta E_{HS\text{–}FM}$. An expression to compute $\hat{S}_i \cdot \hat{S}_j$ can be obtained by expanding the square of the sum of the spin operators, $\left(\hat{S}_i + \hat{S}_j\right)^2$ to give

$$-2\hat{S}_i \cdot \hat{S}_j = S_i^2 + S_j^2 - (S_i + S_j)^2 \tag{2.10}$$

where the fact that $\hat{S}_i \cdot \hat{S}_j = \hat{S}_j \cdot \hat{S}_i$ was used, and the quantity $(S_i + S_j)$ is the total

spin of sub-systems i and j. The splitting energies are derived by acting the spin Hamiltonian on the spin eigenfunction corresponding to the given configuration such that $\hat{S}_i^2 |\psi\rangle = S_i(S_i+1)|\psi\rangle$. We now illustrate the derivation of Equations (2.3) to (2.5) below.

$$\begin{aligned}
\Delta E_{\text{HS–AFM}} &= E_{HS} - E_{AFM} \\
&= J_{\text{SE}}\left[S_{\text{Mn}_1}(S_{\text{Mn}_1}+1) + S_{\text{Mn}_2}(S_{\text{Mn}_2}+1) - S^{\text{HS}}_{\text{Mn}_\text{T}}\left(S^{\text{HS}}_{\text{Mn}_\text{T}}+1\right)\right] \\
&\quad + J_{p-d}\left[S^{\text{HS}}_{\text{Mn}_\text{T}}\left(S^{\text{HS}}_{\text{Mn}_\text{T}}+1\right) + S_{\text{N}}(S_{\text{N}}+1) - S^{\text{HS}}_{\text{T}}\left(S^{\text{HS}}_{\text{T}}+1\right)\right] \\
&\quad - J_{\text{SE}}\left[S_{\text{Mn}_1}(S_{\text{Mn}_1}+1) + S_{\text{Mn}_2}(S_{\text{Mn}_2}+1) - S^{\text{AFM}}_{\text{Mn}_\text{T}}\left(S^{\text{AFM}}_{\text{Mn}_\text{T}}+1\right)\right] \\
&\quad - J_{p-d}\left[S^{\text{AFM}}_{\text{Mn}_\text{T}}\left(S^{\text{AFM}}_{\text{Mn}_\text{T}}+1\right) + S_{\text{N}}(S_{\text{N}}+1) - S^{\text{AFM}}_{\text{T}}\left(S^{\text{AFM}}_{\text{T}}+1\right)\right] \\
&= J_{\text{SE}}\left[-S^{\text{HS}}_{\text{Mn}_\text{T}}\left(S^{\text{HS}}_{\text{Mn}_\text{T}}+1\right) + S^{\text{AFM}}_{\text{Mn}_\text{T}}\left(S^{\text{AFM}}_{\text{Mn}_\text{T}}+1\right)\right] \\
&\quad + J_{p-d}\left[S^{\text{HS}}_{\text{Mn}_\text{T}}\left(S^{\text{HS}}_{\text{Mn}_\text{T}}+1\right) - S^{\text{AFM}}_{\text{Mn}_\text{T}}\left(S^{\text{AFM}}_{\text{Mn}_\text{T}}+1\right)\right. \\
&\quad \left. -S^{\text{HS}}_{\text{T}}\left(S^{\text{HS}}_{\text{T}}+1\right) + S^{\text{AFM}}_{\text{T}}\left(S^{\text{AFM}}_{\text{T}}+1\right)\right] \\
&= -30J_{\text{SE}} - 5J_{p-d} \qquad (2.11)
\end{aligned}$$

where the final expression in Equation (2.11) was obtained using the spin values from Table 2.1. The derivation of Equations (2.4) and (2.5) follow the same form of the derivation of Equation (2.3) presented above.

For the general case of multiple Mn^{2+} dopants around the first tetrahedron of N^{2-}, the spin Hamiltonian becomes

$$\hat{H} = -2\sum_{i<j}^{M} J^{\text{SE}}_{ij}\hat{S}_{\text{Mn}_i}\cdot\hat{S}_{\text{Mn}_j} - 2J_{p-d}\hat{S}_{\text{Mn}_\text{T}}\cdot\hat{S}_{\text{N}} \qquad (2.12)$$

where J^{SE}_{ij} is the superexchange coupling constant between Mn^{2+} ions i and j, and $\hat{S}_{\text{Mn}_i}$ is the spin operator for the i^{th} Mn^{2+} ion. The summation runs over all unique pairs of Mn^{2+} ions up to M number of dopants. The unpaired Mn^{2+} spins are again treated as an interacting spin system, thus, $\hat{S}_{\text{Mn}_\text{T}}$ describes the total spin of all Mn^{2+}

Table 2.2. Description of the spin configurations for the case of M (N) number of Mn^{2+} (N^{2-}) around N^{2-} (Mn^{2+}). The second column shows the alignment of unpaired Mn^{2+} and N^{2-} spins as spin-up (↑) or spin-down (↓).

Configuration	Arrangement	$\hat{S}_{\mathrm{Mn_T}}$	$\hat{S}_{\mathrm{N_T}}$	$\hat{S}_{\mathrm{T}}$
HS	$\mathrm{Mn}_M(\uparrow)$–$\mathrm{N}(\uparrow)$	$\frac{5}{2}M$	$\frac{1}{2}$	$\left(\frac{5}{2}M+\frac{1}{2}\right)$
	$\mathrm{N}_N(\uparrow)$–$\mathrm{Mn}(\uparrow)$	$\frac{1}{2}N$	$\frac{5}{2}$	$\left(\frac{1}{2}N+\frac{5}{2}\right)$
FM	$\mathrm{Mn}_M(\uparrow)$–$\mathrm{N}(\downarrow)$	$\frac{5}{2}M$	$\frac{1}{2}$	$\left(\frac{5}{2}M-\frac{1}{2}\right)$
	$\mathrm{N}_N(\downarrow)$–$\mathrm{Mn}(\uparrow)$	$\frac{1}{2}N$	$\frac{5}{2}$	$\left(-\frac{1}{2}N+\frac{5}{2}\right)$

dopants. Similarly, for the general case of multiple N^{2-} dopants around the first tetrahedron of Mn^{2+}, the spin Hamiltonian becomes

$$\hat{H} = -2\sum_{i<j}^{N} J_{ij}^{\mathrm{SE}} \hat{S}_{\mathrm{N}_i} \cdot \hat{S}_{\mathrm{N}_j} - 2J_{p-d}\hat{S}_{\mathrm{N_T}} \cdot \hat{S}_{\mathrm{Mn}} \tag{2.13}$$

where J_{ij}^{SE} is the superexchange coupling constant between N^{2-} ions i and j, and $\hat{S}_{\mathrm{Mn}_i}$ is the spin operator for the i^{th} Mn^{2+} ion. The summation runs over all unique pairs of N^{2-} ions up to N number of dopants. The unpaired N^{2-} spins are similarly treated as an interacting spin system, thus, $\hat{S}_{\mathrm{N_T}}$ describes the total spin of all N^{2-} dopants. The spin values for the HS and FM configurations are summarized in Table 2.2.

To derive Equation (2.3), we use Equation (2.14) and the data in Table 2.2. Note that since we are taking the difference between the HS and FM configurations, the

superexchange terms cancel as they did in Equation (2.3).

$$\begin{aligned}
\Delta E^{\mathrm{Mn}_M\mathrm{–N}}_{\mathrm{HS–FM}} &= E^{\mathrm{Mn}_M\mathrm{–N}}_{\mathrm{HS}}(M) - E^{\mathrm{Mn}_M\mathrm{–N}}_{\mathrm{FM}}(M) \\
&= J_{p-d}\left[S_{\mathrm{Mn_T}}\left(S_{\mathrm{Mn_T}}+1\right) + S_{\mathrm{N}}\left(S_{\mathrm{N}}+1\right) - S^{\mathrm{HS}}_{\mathrm{T}}\left(S^{\mathrm{HS}}_{\mathrm{T}}+1\right)\right] \\
&\quad - J_{p-d}\left[S_{\mathrm{Mn_T}}\left(S_{\mathrm{Mn_T}}+1\right) + S_{\mathrm{N}}\left(S_{\mathrm{N}}+1\right) - S^{\mathrm{FM}}_{\mathrm{T}}\left(S^{\mathrm{FM}}_{\mathrm{T}}+1\right)\right] \\
&= J_{p-d}\left[-S^{\mathrm{HS}}_{\mathrm{T}}\left(S^{\mathrm{HS}}_{\mathrm{T}}+1\right) + S^{\mathrm{FM}}_{\mathrm{T}}\left(S^{\mathrm{FM}}_{\mathrm{T}}+1\right)\right] \\
&= J_{p-d}\left[-\left(\frac{5}{2}M+\frac{1}{2}\right)\left(\frac{5}{2}M+\frac{3}{2}\right) + \left(\frac{5}{2}M-\frac{1}{2}\right)\left(\frac{5}{2}M+\frac{1}{2}\right)\right] \\
&= -\left(5M+1\right)J_{p-d}
\end{aligned} \tag{2.14}$$

Lastly, Equation (2.15) is derived in a similar manner.

$$\begin{aligned}
\Delta E^{\mathrm{N}_N\mathrm{–Mn}}_{\mathrm{HS–FM}} &= E^{\mathrm{N}_N\mathrm{–Mn}}_{\mathrm{HS}}(N) - E^{\mathrm{N}_N\mathrm{–Mn}}_{\mathrm{FM}}(N) \\
&= J_{p-d}\left[S_{\mathrm{N_T}}\left(S_{\mathrm{N_T}}+1\right) + S_{\mathrm{Mn}}\left(S_{\mathrm{Mn}}+1\right) - S^{\mathrm{HS}}_{\mathrm{T}}\left(S^{\mathrm{HS}}_{\mathrm{T}}+1\right)\right] \\
&\quad - J_{p-d}\left[S_{\mathrm{N_T}}\left(S_{\mathrm{N_T}}+1\right) + S_{\mathrm{Mn}}\left(S_{\mathrm{Mn}}+1\right) - S^{\mathrm{FM}}_{\mathrm{T}}\left(S^{\mathrm{FM}}_{\mathrm{T}}+1\right)\right] \\
&= J_{p-d}\left[-S^{\mathrm{HS}}_{\mathrm{T}}\left(S^{\mathrm{HS}}_{\mathrm{T}}+1\right) + S^{\mathrm{FM}}_{\mathrm{T}}\left(S^{\mathrm{FM}}_{\mathrm{T}}+1\right)\right] \\
&= J_{p-d}\left[-\left(\frac{1}{2}N+\frac{5}{2}\right)\left(\frac{1}{2}N+\frac{7}{2}\right) + \left(-\frac{1}{2}N+\frac{5}{2}\right)\left(-\frac{1}{2}N+\frac{7}{2}\right)\right] \\
&= -6NJ_{p-d}
\end{aligned} \tag{2.15}$$

Chapter 3

EFFECTS OF CRYSTALLOGRAPHIC AND SHAPE ANISOTROPIES ON DOPANT-CARRIER EXCHANGE INTERACTIONS IN MAGNETIC SEMICONDUCTOR QUANTUM DOTS

The roles of nanocrystal shape and crystalline anisotropy on carrier-mediated magnetism in diluted magnetic semiconductor nanocrystals are examined in this chapter. A combination of density functional theory and analytical perturbation theory are used to investigate the electronic structure of Mn^{2+}-doped nanocrystals of varied shapes and sizes. Density functional calculations are used to compute the magnetic exchange energies and to analyze the band edge splitting in these materials. To understand the observed anisotropic magnetism, a perturbative relationship between the magnetic exchange and nanocrystal anisotropy is derived to illustrate the effect in an analytical and quantum mechanical expression. The first-principles calculations and the analytical predictions are in excellent agreement, and the anisotropic driving terms in the magnetic exchange are very well explained by the final perturbation equation. The work presented in this chapter is reproduced with permission from Peng, B.; May, J. W.; Gamelin, D. R.; Li, X. *J. Phys. Chem. C* **2014**, *118*, 7630-7636.

3.1 Introduction

Diluted magnetic semiconductor (DMS) nanostructures have been the subject of intense experimental and theoretical investigation for their potential use in spin-electronic and spin-photonic devices.[2–4,46,47,56–60] Fundamental magnetic exchange interactions between dopant unpaired spins and charge carriers (electron or hole)

give rise to new ways of manipulating either carrier spin polarizations or the spins of the magnetic dopants themselves.[1,29,61,62,100–111] For example, in self-assembled CdTe quantum dots grown by vacuum deposition, dopant-carrier exchange interactions have been used to manipulate the magnetic properties of single Mn^{2+} ions in individual quantum dots via reversible electrical control of the quantum dot charge state.[112] In colloidal DMS quantum dots grown from solution, stronger quantum confinement leads to extremely large exchange fields, and correspondingly robust excitonic magnetic polarons. Redox addition of quantum-confined conduction-band(CB) electrons (e^-_{CB}) to DMS quantum dots has also been used to activate long-range dopant-dopant magnetic exchange interactions,[27] yielding a motif analogous to a bound magnetic polaron but stable indefinitely and charge-tunable. The so-called *s*–*d* exchange coupling between e^-_{CB} and magnetic dopants is also responsible for fast Auger de-excitation of dopant excited states in photoexcited DMS nanocrystals.[113,114] Theoretical analyses combining first-principles calculations and analytical perturbation theory have provided new insight into the fundamental microscopic underpinnings of these physical phenomena.[48,49]

An important unanticipated feature of the robust EMPs found in colloidal Mn^{2+}-doped CdSe quantum dots was the apparent role of anisotropy. Anisotropy was proposed to increase the total polaron stabilization energy beyond its isotropic limit, in the process generating barriers to magnetization reversal.[1] This result implies the potential to control photomagnetism in DMS nanocrystals by synthetic tuning of nanocrystal shape or lattice anisotropies. The nanocrystal's shape can be used to modulate confinement of bandlike electrons along different nanocrystal axes (*x*, *y*, *z*). The influence of shape-deformed and quantum-confined e^-_{CB} on the dopant-carrier *s*–*d* exchange has been previously investigated, and has been suggested to give rise to the reversible piezomagnetism in Mn^{2+}-doped quantum dots.[79] However, the shape anisotropic effect on the stronger dopant-carrier *p*–*d* exchange remains unexplored. In addition, the intrinsic crystalline anisotropy of non-cubic lattice structures like

wurtzite may themselves strongly impact dopant-carrier p–d magnetic exchange. The microscopic origins of the anisotropic magnetism of such colloidal DMS nanocrystals is still unclear, however, in part because of major challenges in controlling specifically nanocrystal shape anisotropy without altering other important parameters (*e.g.*, total volume, dopant distribution, etc.), and in part because of practical challenges with effective doping of very small semiconductor nanocrystals.

Here, we use first-principles calculations and perturbation theory to examine the roles of nanocrystal shape and crystalline anisotropy on carrier-mediated magnetism in DMS nanocrystals. A perturbative relationship is presented that illustrates the connection between magnetic exchange and nanocrystal anisotropy, and this relationship is explored both analytically and quantum mechanically. For these studies, we use wurtzite Mn^{2+}-doped CdSe nanocrystals as an example, but the insights can be generalized to all DMS nanocrystals.

3.2 Methodology

The CdSe nanocrystals were constructed using the bulk CdSe wurtzite crystal structure with lattice parameters[82] $a = 4.2985$ Å and $c = 7.0152$ Å according to the previously published scheme.[90] The dangling bonds on the surface of the nanocrystals were passivated with pseudohydrogen atoms having modified nuclear charges of 0.5 and 1.5 to terminate surface Se^{2-} and Cd^{2+} ions, respectively. The surface Cd–H and Se–H bonds were fully optimized. This pseudohydrogen capping leads to a well-defined band gap and stable nanocrystal geometry. Total energies and electronic structures were obtained using the development version of the Gaussian package.[115] All calculations were carried out using the PBE1PBE hybrid functional[94–96] and the Los Alamos double-ζ pseudocore potential (LANL2DZ) basis set,[97–99] in which Cd $(4d, 5s, 5p)$, Se $(4s, 4p)$, Mn $(3s, 3p, 4s, 3d)$, and H $(1s)$ electrons are described with explicit basis functions. This computational scheme has been successful in describing the electronic structure and magnetic exchange interactions in transition-metal-doped

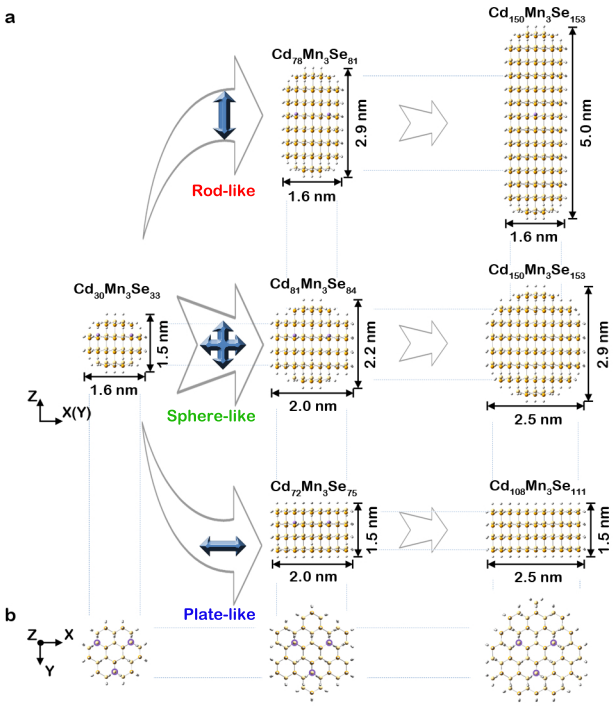

Figure 3.1. The structure of Mn^{2+}-doped CdSe nanocrystals investigated here with the C_3-axis of the parent crystal oriented (a) vertically in the plane of the page and (b) out of the page. In part a, the first row corresponds to rod-like nanocrystals, the second row to sphere-like nanocrystals, and the third row to plate-like nanocrystals. The purple circles label the Mn^{2+} dopants, which were positioned to maintain the C_{3v} symmetry of the nanocrystal.

ZnO,[35,36,38,100] CdSe,[49] and CdS[114] nanocrystals.

Figure 3.1 shows the CdSe nanocrystals investigated in this paper. The diameter of the quasi-spherical $Cd_{33}Se_{33}$ nanocrystal is ∼1.5 nm. Other nanocrystals were then constructed by adding additional anion/cation layers in the direction of the confinement length to the $Cd_{33}Se_{33}$ nanocrystal to create three groups: rod-like ($Cd_{81}Se_{81}$ and $Cd_{153}Se_{153}$), sphere-like ($Cd_{84}Se_{84}$ and $Cd_{153}Se_{153}$), and plate-like ($Cd_{75}Se_{75}$ and $Cd_{111}Se_{111}$) nanocrystals. The dimensions of these nanocrystals are smaller than the CdSe exciton Bohr radius (a_0 = 5.6 nm),[116] suggesting that electrons/holes in these CdSe nanocrystals are in the quantum confinement regime (note the dimension

of the nanocrystal is only an estimate of the confinement potential). Doped CdSe nanocrystals were constructed by substituting Mn^{2+} dopants for the Cd^{2+} ions while retaining the overall neutral charge of the nanocrystals. Because the goal of this work is to investigate the intrinsic anisotropy of doped CdSe, the C_{3v} symmetry of doped nanocrystals was maintained to avoid any broken-symmetry induced anisotropy. As shown in the top views of these nanocrystals in Figure 3.1(b), Mn^{2+} dopants were positioned symmetrically with a 3-fold degeneracy.

3.3 Results and Discussion

3.3.1 Anisotropic Splitting of the Valence Band Edge

The wurtzite crystal structure of the CdSe nanocrystals leads to a nonspherical C_{3v} crystal field at each cation site, where the axial Cd–Se bond (along the C_3-axis) is slightly longer than the three equatorial bonds. As a result, the Se^{2-} $4p$ orbitals split to form a doubly degenerate (p_x, p_y) group, and a p_z orbital, giving rise to an energy splitting at the VB edge. This anisotropic splitting is an intrinsic property of the wurtzite structure. On the other hand, an interesting aspect of semiconductor nanocrystals is that the confinement can be used to tune the energy levels. In other words, the nanocrystal's shape (rod, sphere, or plate) can give rise to additional energy splittings between nonspherical orbitals. In particular, the delocalized p_x, p_y, and p_z orbitals of the CdSe VB are strongly affected by quantum confinement along each spatial axis. The energy splitting arising from the nanocrystal's shape is referred to here as the shape anisotropic splitting.

In spherical nanocrystals, where quantum confinement in all dimensions is the same, the crystalline anisotropy is the dominant driving force of the band edge splitting in wurtzite nanocrystals. For spherical nanocrystals, Figure 3.2(b) shows that the energy levels near the top of the VB split into (p_x, p_y) and p_z groups due to the crystalline anisotropy, with the p_z level sitting $\sim$0.1 eV lower than the VB edge consisting

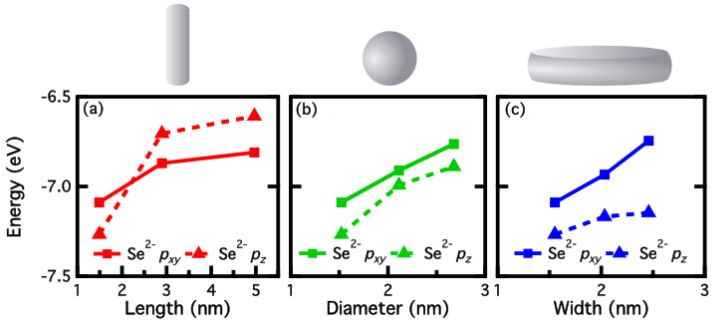

Figure 3.2. Molecular orbital energies of the Se^{2-} p_{xy} (■) and p_z (▲) groups at the valence band edge for the three sizes of (a) rod-like, (b) sphere-like, and (c) plate-like nanocrystals plotted versus decreasing quantum confinement along the x, y, and/or z dimensions.

of p_x and p_y orbitals in the $Cd_{33}Se_{33}$ nanocrystal. As the diameter of the spherical nanocrystal increases, the energy of the VB edge (p_x, p_y) and p_z levels increase as a result of a decreasing quantum confinement effect; however, the energy difference is relatively insensitive to the diameter of spherical nanocrystals in the absence of the shape anisotropic effect. The effect of quantum confinement can be understood using the particle-in-a-sphere model for the VB levels,[40–42]

$$\varepsilon_{p_{(x,y)}} \approx \varepsilon_{\mathrm{VB}} - \frac{\pi^2\hbar^2}{2m_h^* L_{xy}^2} \tag{3.1}$$

$$\varepsilon_{p_z} \approx \varepsilon_{\mathrm{VB}} - \Delta\varepsilon_c - \frac{\pi^2\hbar^2}{2m_h^* L_z^2}, \tag{3.2}$$

where $\varepsilon_{\mathrm{VB}}$ is the energy of the VB edge of bulk CdSe, L is the confinement length, m_h^* is the effective mass of a valence-band(VB) hole (h_{VB}^+), and $\Delta\varepsilon_c$ is the crystal field anisotropy splitting. Equation (3.1) and Equation (3.2) were derived using a potential that models the dielectric polarization of a VB hole inside a spherical dielectric medium and the potential is infinite outside the quantum dot. It is reasonable to assume that the effective mass of p_x, p_y, and p_z electrons are approximately equal.

When one of the nanocrystal dimensions (L_x, L_y, L_z) is elongated (compressed), the quantum confinement effect along that dimension is suppressed (enhanced) according to the quantum confinement equations. This can be observed in the rod- and plate-like nanocrystals. Figure 3.2(a) shows that in rod nanocrystals, the p_z level shifts significantly to higher energy as the L_z dimension is elongated. Meanwhile the energy change of the (p_x, p_y) group is much smaller than that of the p_z level. This leads to a crossover of the p_z and the (p_x, p_y) energies, resulting in the vanishing of any anisotropic splitting for a specific geometric shape. Given the diameter of the xy-plane, L_{xy}, this crossover point can be predicted by equating Equations (3.1) and (3.2). For the rod-like nanocrystals considered here, where $L_{xy} = 1.6$ nm, the anisotropic splitting vanishes at the VB edge when L_z is ∼2.2 nm as shown in Figure 3.2(a). On the other hand, when L_{xy} is elongated while L_z is held constant, the anisotropic splitting increases as observed in Figure 3.2(c) for the plate-like nanocrystals. This is attributed to a decreasing quantum confinement effect in the xy-plane, which leads to an increase in the energy of the p_x and p_y levels.

Analysis in this section suggests that the crystalline anisotropy can be altered or modulated by the shape anisotropy effect. In the following discussion, both the crystalline and shape anisotropic splittings will be shown to strongly influence carrier-dopant magnetic exchange interactions in DMS nanocrystals.

3.3.2 Effect of Anisotropy on Magnetic p–d Exchange

Figure 4.1 shows density of states (DOS) diagrams using molecular orbitals calculated for a $Cd_{150}Mn_3Se_{153}$ rod-like, a $Cd_{150}Mn_3Se_{153}$ sphere-like, and a $Cd_{108}Mn_3Se_{111}$ plate-like nanocrystal with the spin-up and spin-down spin densities plotted as positive and negative values, respectively. The VB and CB of CdSe nanocrystals are mainly composed of Se^{2-} 4p and Cd^{2+} 5s character, respectively. The DOS plots show that all three nanocrystal shapes share similar electronic characteristics. The partial DOS of Mn^{2+} 3d levels show that the occupied Mn^{2+} 3d levels are ∼4.6–4.7 eV lower than

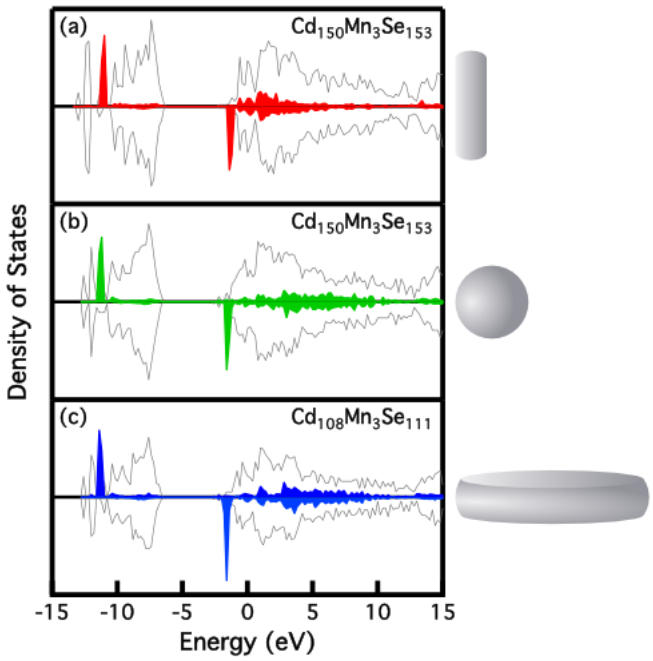

Figure 3.3. Density of states (DOS) diagrams calculated for (a) a $Cd_{150}Mn_3Se_{153}$ rod-like nanocrystal, (b) a $Cd_{150}Mn_3Se_{153}$ sphere-like nanocrystal, and (c) a $Cd_{108}Mn_3Se_{111}$ plate-like nanocrystal with the Mn^{2+} ions placed at cation sites near the vertical center of the C_3-axis so as to maintain the C_{3v} symmetry of the nanocrystal. The shaded regions show the Mn^{2+} $3d$ component for each DOS diagram magnified by 5x. Spin up, positive density values; spin down, negative density values.

the VB edge, and the empty spin-down Mn^{2+} $3d$ manifold is $\sim$1.2 eV higher than the CB edge. Although these dopant d levels are considered to be deep donor states, they are responsible for the observed magnetization in these materials.[14,20,117]

In a tetrahedral crystal field, electrons with the same spin split into two lower energy d_e ($d_{x^2-y^2}$, d_{z^2}) and three higher energy d_{t_2} (d_{xy}, d_{yz}, d_{xz}) levels, while single-site exchange interactions lead to a large splitting between electrons with different spins. In contrast to the delocalized VB levels, the dopant d levels are very localized, confined by the four nearest neighbor Se^{2-} ions. When a h^+_{VB} is created, the interaction

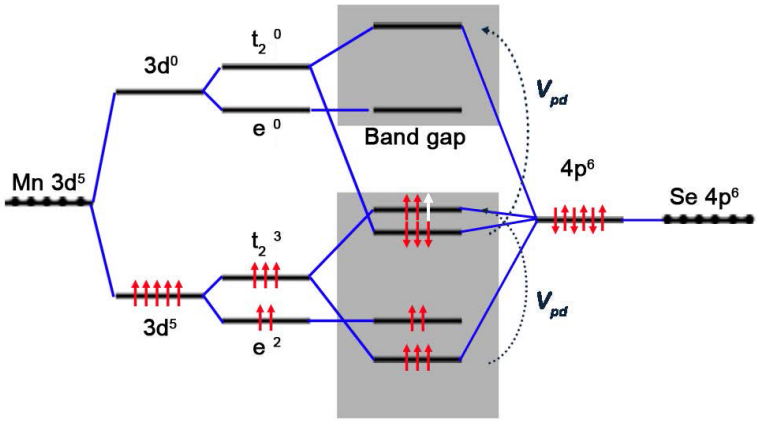

Figure 3.4. Schematic illustration of the energy levels involved in p–d magnetic exchange in Mn^{2+}-doped CdSe nanocrystals.

between transition metal dopants and the unpaired VB spin is responsible for the observed magnetic ordering. The dominant mechanism is the so-called p–d exchange arising from the spin-dependent hybridization between the dopant d electrons and the p levels of the VB. The dopant d_e levels do not hybridize with the VB p levels due to the orbital symmetry. As a result, the d_e levels are not influenced by the quantum confinement effect and show almost no dependence on the shape anisotropy. On the other hand, because of the hybridization with the VB p levels, the occupied dopant d_{t_2} levels reside below the d_e levels (inverted bonding scheme) and exhibit anisotropic dependence on the nanocrystal's shape. In addition, this hybridization gives rise to the magnetic exchange interaction that is responsible for magnetic ordering of the transition-metal-doped semiconductor nanocrystals. This analysis, illustrated in Figure 3.4 and based on field theory and the fundamental p–d exchange mechanism, suggests that the anisotropic characteristics of the wurtzite crystal field discussed in the previous section may play an important role in the magnetic ordering of DMS nanocrystals.

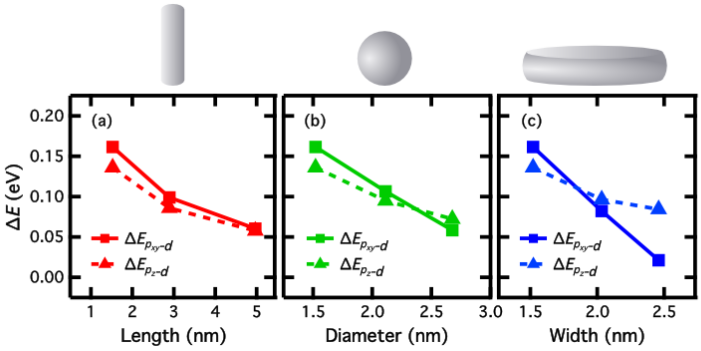

Figure 3.5. Band-edge energy splittings resulting from addition of a hole to the p_{xy} (■) and p_z (▲) valence-band-edge orbitals of (a) rod-like, (b) sphere-like, and (c) plate-like nanocrystals plotted versus decreasing quantum confinement along the x, y, and/or z dimensions. $\Delta E = E_{\mathrm{FM}} - E_{\mathrm{AFM}}$ is the energy difference between the h^{+}_{VB} aligned parallel (AFM) and antiparallel (FM) with the unpaired Mn^{2+} $3d$ electrons, which are all aligned parallel.

The calculated magnetic splitting energies arising from the interaction between dopant d electrons and VB p_z and (p_x, p_y) levels, respectively, are plotted in Figure 3.5. The antiferromagnetic (ferromagnetic) state refers to the configuration where Mn^{2+} $3d$ electrons are in the opposite (same) spin alignment with the unpaired VB electron. For the cases studied here, the antiferromagnetic (AFM) state is always lower in energy than the ferromagnetic (FM) state. As expected from the discussion above, the magnetic splitting energy exhibits a dependence on the crystalline and shape anisotropy. Such a dependence could open an avenue for controlling the magnetization in DMS nanocrystals; however, the mechanism is not yet well understood. Although the VB edge anisotropic splitting (Figure 3.2) can be analyzed using quantum confinement equations, the effect of crystalline and shape anisotropy on the magnetic exchange is rather complex as the exchange splittings (Figure 3.5) do not exhibit the same behavior as the band-edge anisotropy. Conventional models to compute p–d exchange often assume an isotropic distribution, which cannot be used to resolve the anisotropic magnetic exchange. To understand the effect of shape and

crystalline anisotropy on the magnetic exchange splitting, we apply perturbation theory to the electronic structure of DMS nanocrystals. In the following discussion, we consider a hole generated in the p_z VB orbital in a Mn^{2+}-doped CdSe nanocrystal. Equations are derived to evaluate the anisotropic p–d magnetic exchange between dopant d electrons and p_z-type VB electrons. The following discussion and equations can be generalized to p–d exchange splitting arising from the p_x and p_y character of the VB.

H_0, $\varepsilon_{\mathrm{VB}_{p_z}}$ ($\psi_{\mathrm{VB}_{p_z}}$) and $\varepsilon_{d_{t_2}}$ ($\psi_{d_{t_2}}$) are defined as the Hamiltonian, energies (wave functions) of the p_z type molecular orbitals near the top of the VB, and dopant d_{t_2} levels of a neutral DMS nanocrystal. Atomic orbitals are represented by $\{\phi\}$. In the following derivation, all Mn^{2+} $3d$ electrons are in the spin-up configuration. Paired occupied levels are generally included in the perturbation theory. In neutral doped DMS QDs, the interactions between pseudopaired levels and dopants can lead to magnetic ordering.[118,119] In the presence of a VB hole, contributions from pseudopaired levels to the magnetic exchange are considered small compared to the strong p–d exchange mechanism. Therefore, we only need to consider terms arising from unpaired electrons in the system. Although all Mn^{2+} $3d$ electrons contribute to the magnetization, only d_{t_2} levels participate in the p–d exchange interaction with the VB because of their symmetry.

When a hole is created in the p_z level of the VB, an unpaired VB p_z electron will participate in the magnetic p–d exchange interaction with the dopant d electrons (Figure 3.4). When the unpaired VB p_z electron is aligned with the Mn^{2+} d_{t_2} electrons, no spin-allowed p–d hybridization pathways exist, and the Hamiltonian for this FM configuration can be simply written as

$$H_{\mathrm{FM}} = H_0 + V_{ion}, \tag{3.3}$$

where H_0 is the neutral nanocrystal Hamiltonian before the hole is created and V_{ion} is

the ionization potential of the VB p_z electron. For the AFM state, where the unpaired p_z electron is in the spin-down configuration, the Hamiltonian can be expressed as

$$H_{\mathrm{AFM}} = H_0 + V'_{ion} - \sum_{d_{t_2}} \left(\frac{|\langle \psi_{\mathrm{VB}_{p_z}\uparrow} | \hat{V} | \psi_{d_{t_2}\uparrow} \rangle|^2}{\varepsilon_{\mathrm{VB}_{p_z}\uparrow} - \varepsilon_{d_{t_2}\uparrow}} + \frac{|\langle \psi_{d_{t_2}\downarrow} | \hat{V} | \psi_{\mathrm{VB}_{p_z}\downarrow} \rangle|^2}{\varepsilon_{d_{t_2}\downarrow} - \varepsilon_{\mathrm{VB}_{p_z}\downarrow}} \right), \tag{3.4}$$

where $\uparrow$ and $\downarrow$ label the orbital spin-state. In Equation (3.4), perturbations from both the $d_{t_2\uparrow} \rightarrow \mathrm{VB}_{p_z\uparrow}$ and $\mathrm{VB}_{p_z\downarrow} \rightarrow d_{t_2\downarrow}$ transfer pathways (Figure 3.4) are considered. Such a perturbation treatment is valid because the orbital energy gap is much bigger than the transfer integral. The p_z-d magnetic exchange splitting energy is then written as

$$\Delta E_{p_z d} = H_{\mathrm{FM}} - H_{\mathrm{AFM}} = \sum_{d_{t_2}} \left(\frac{|\langle \psi_{\mathrm{VB}_{p_z}\uparrow} | \hat{V} | \psi_{d_{t_2}\uparrow} \rangle|^2}{\varepsilon_{\mathrm{VB}_{p_z}\uparrow} - \varepsilon_{d_{t_2}\uparrow}} + \frac{|\langle \psi_{d_{t_2}\downarrow} | \hat{V} | \psi_{\mathrm{VB}_{p_z}\downarrow} \rangle|^2}{\varepsilon_{d_{t_2}\downarrow} - \varepsilon_{\mathrm{VB}_{p_z}\downarrow}} \right) + \delta_{ion}. \tag{3.5}$$

where δ_{ion} is a constant correction term arising from the difference in ionization potential of FM and AFM states. For a given dopant, there are three d_{t_2} levels participating in the p–d exchange interaction. As these levels are rather localized at the dopant site, the associated molecular orbitals $\psi_{d_{t_2}}$ can be replaced by the atomic orbitals $\phi_{d_{t_2}}$ in the equation. Assuming all interactions between d_{t_2} levels (either spin-up or spin-down) and VB p_z are of the same strength, $V_{p_z d} = \langle \psi_{\mathrm{VB}_{p_z}\uparrow} | \hat{V} | \phi_{d_{t_2}\uparrow} \rangle = \langle \phi_{d_{t_2}\downarrow} | \hat{V} | \psi_{\mathrm{VB}_{p_z}\downarrow} \rangle$, allows Equation (3.5) to be simplified as

$$\begin{aligned} \Delta E_{p_z d} &= 3m \cdot V_{p_z d}^2 \cdot \left(\frac{1}{\varepsilon_{\mathrm{VB}_{p_z}\uparrow} - \varepsilon_{d_{t_2}\uparrow}} + \frac{1}{\varepsilon_{d_{t_2}\downarrow} - \varepsilon_{\mathrm{VB}_{p_z}\downarrow}} \right) + \delta_{ion} \\ &= 3m \cdot V_{p_z d}^2 \cdot S_{p_z d} + \delta_{ion}, \end{aligned} \tag{3.6}$$

where m is the number of dopants. While there are a number of well-defined forms for the VB wave functions expanded in atomic orbitals or in the momentum space for bulk systems, they are generally not suitable for descriptions of a quantum-confined

VB edge. Because the analytical wave function of a quantum-confined VB/CB-carrier can be expressed as a zero-order Bessel function,[40] the basis set expansion of the same wave function can be written as

$$|\psi_{\mathrm{VB}_{p_z}}\rangle = \mathrm{C} \cdot \sum_i \frac{\sin(\frac{\pi r_i}{R})}{\sqrt{2\pi R} \cdot r_i} \cdot \frac{1}{\sqrt{N}} \cdot |\phi_{p_z}(r - r_i)\rangle, \tag{3.7}$$

where C is the normalization constant and $|\phi_{p_z}(r - r_i)\rangle$ is the anion p_z-type atomic orbital localized at the anion site r_i (assuming a set of orthonormalized atomic orbitals). N is the number of anions in the nanocrystal. R is the radius/length of the quantum confinement potential, and in the case of exchange splitting arising from the p_z orbital, this is the nanocrystal's length along the z-axis. Note that Equation (3.7) becomes a conventional VB wave function (i.e., Bloch function) for bulk when the envelop function is one instead of the Bessel-function type. As the p–d exchange interaction is short-ranged within the first tetrahedron of the dopant, only the four nearest $|\phi_{p_z}(r - r_i)\rangle$ atomic orbitals around a given dopant will contribute to the p–d splitting energy. As a result, Equation (3.6) can be written as

$$\begin{aligned} \Delta E_{p_z d} &= \mathrm{A} \cdot \frac{\sin^2\left(\frac{\pi r_0}{R}\right)}{2\pi R \cdot r_0^2} \cdot \frac{m}{N} \cdot v_{p_z d}^2 \cdot S_{p_z d} + \delta_{ion} \\ &= \mathrm{A} \cdot v_{p_z d}^2 \cdot S(R, m, N) + \delta_{ion}, \end{aligned} \tag{3.8}$$

where A collects all constants, and $v_{p_z d} = \langle \phi_{p_z} | \hat{V} | \phi_{d_{t_2}} \rangle$ is the p–d transfer integral defined in the atomic orbital basis. r_0 is the average center-to-center distance between the dopant and the nearest-neighbor Se^{2-} ions. In Equation (3.8), we define a shape anisotropy function $S(R, m, N) = \frac{\sin^2(\frac{\pi r_0}{R})}{2\pi R \cdot r_0^2} \cdot \frac{m}{N} \cdot S_{p_z d}$ that can be calculated using properties obtained from electronic structure calculations.

Equation (3.8) is the total magnetic exchange splitting. It encodes the anisotropy dependence of p–d exchange in DMS nanocrystals, and the effects of the quantum confinement length R and the dopant concentration m. Figure 3.7 shows that all

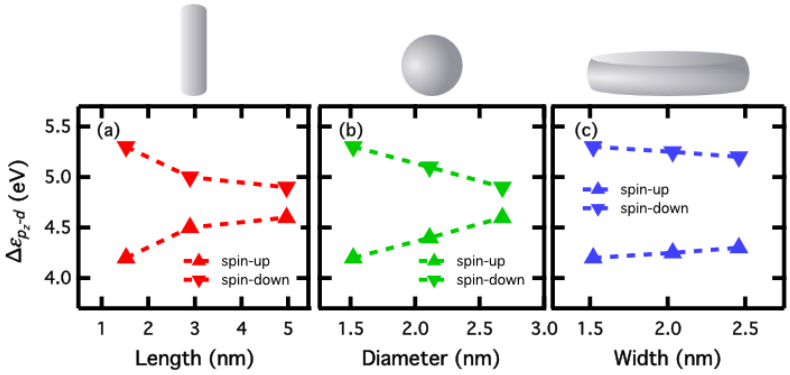

Figure 3.6. Molecular orbital energy differences between spin-up (▲) and spin-down (▼) VB-p_z and Mn^{2+} $3d_{t_2}$ orbitals for the three sizes of (a) rod-like, (b) sphere-like, and (c) plate-like nanocrystals.

computed p–d exchange splittings are in excellent agreement with predictions made by Equation (3.8). On the basis of the perturbative description of magnetic p–d exchange, the anisotropic effects in DMS nanocrystals are made clear. $v_{p_z d}$ is the transfer integral that depends on the local electronic interaction between dopant and nearest-neighbor p orbitals. As a result, $v_{p_z d}$ is affected by the intrinsic crystalline anisotropy. The shape anisotropic effect modulates the strength of the overall magnetic exchange via the orbital energy difference term $S_{p_z d} = \left(\frac{1}{\varepsilon_{\mathrm{VB}_{p_z}\uparrow} - \varepsilon_{d_{t_2}\uparrow}} + \frac{1}{\varepsilon_{d_{t_2}\downarrow} - \varepsilon_{\mathrm{VB}_{p_z}\downarrow}}\right)$. Because $\varepsilon_{\mathrm{VB}_{p_z}}$ is governed by the quantum confinement effect (Equations (3.1) and (3.2)), the overall p–d exchange will exhibit shape anisotropy in addition to the intrinsic crystalline anisotropy that splits p_z from (p_x, p_y). Because the dopant electronic structure is localized, $\Delta\varepsilon_{t_2} = \varepsilon_{d_{t_2}\downarrow} - \varepsilon_{d_{t_2}\uparrow}$, can be considered a constant. Therefore, the p–d exchange splitting is reciprocally dependent on the relative energy of the VB p_z orbital with respect to the dopant d levels (both occupied and empty orbitals). Figure 3.6 shows the molecular orbital energy differences for the systems studied here. These energy differences simply follow the quantum confinement of the VB and CB. It can be shown from Equation (3.6) that the maximum p–d exchange splitting occurs when

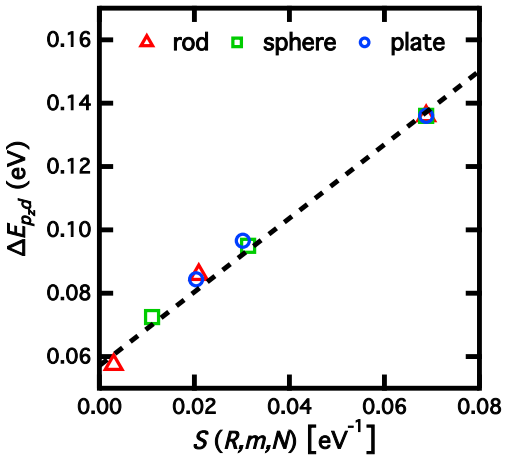

Figure 3.7. Magnetic exchange splitting energy between Mn^{2+} $3d_{t_2}$-levels and h^{+}_{VB} in the VB edge-p_z orbital plotted versus the shape anisotropy function $S(R, m, N)$ defined in Equation (3.8) for the three sizes of rod-like ($\triangle$), sphere-like ($\square$), and plate-like ($\bigcirc$) nanocrystals. The dashed line is a fit of Equation (3.8). The slope and intercept are 1.16 eV^2 and 0.057 eV, respectively.

the VB p_z level is exactly half way between the occupied and unoccupied Mn^{2+} $3d$ levels. Although this criterion is not easily satisfied, the shape anisotropy dependence could potentially be used to fine-tune the energy gap, aiding in the rational design of magnetic nanocrystals. Equation (3.8) could also be used to design stronger magnetic polarons in DMS nanocrystals by tuning the dopant concentration, the confinement length, and the dopant energy offsets with respect to band levels. Note the similarity in axial confinement between the plate-like structure and epitaxial QDs,[79,120] results obtained in this work can be extended to understand anisotropy effects in epitaxial QDs.

3.4 Conclusion

Anisotropic magnetism in DMS nanocrystals has been investigated using first-principles calculations and analytical perturbation theory. DFT calculations show that the VB

edge splits into (p_x, p_y) and p_z sub-bands, and the energy splittings are controlled by quantum confinement effects as predicted by the analytical theory. However, the magnetic exchange splittings exhibit a different trend than that of the band edge splittings. We have applied perturbation theory with analytical wave functions to analyze the physical underpinnings of the DFT-calculated anisotropic magnetic exchange. The final analytical expression, Equation (3.8), encodes the important anisotropic perturbations to the magnetic splitting in DMS nanocrystals. The transfer integral is shown to be dependent on the local electronic interaction between dopant d and nearest-neighbor p orbitals, and therefore is affected by the intrinsic crystalline anisotropy. The shape anisotropic effect modulates the strength of the overall magnetic exchange via the orbital energy difference term that is governed by the quantum confinement effect. The DFT calculations and the analytical predictions are in excellent agreement. The analytical model derived in this work can be generalized to nanocrystals with multiple charge carriers and multiple dopants. The theory presented here lays the groundwork for using crystalline and shape anisotropies to tune the magnetism in DMS nanocrystals.

Chapter 4

THEORETICAL CHARACTERIZATION OF EXTRA ELECTRONS IN PHOTOCHEMICALLY CHARGED AND ALUMINUM DOPED ZINC OXIDE QUANTUM DOTS

The experimental absorption spectra of photochemically reduced ZnO and aluminum doped ZnO quantum dots are indistinguishable. In this chapter it is shown using time-dependent density functional theory, that despite these spectroscopic similarities, the band structure of these materials may not be as similar as previously thought, which also accounts for the reported differences in the electron-transfer reactivities of these materials. The connection between the density functional theory results and a simple quantum mechanical particle in a spherical potential model are highlighted. Molecular orbitals obtained from density functional theory reveal the often-used S-, P-, D-,...type "super" orbitals used to characterize the absorption spectra of these materials.

4.1 Introduction

Colloidal semiconductor quantum dots (QDs) containing excess delocalized charge carriers play an important role towards preparing devices for solar energy conversion,[121] information processing,[122] and other technologies. Such *n*- or *p*-type semiconductor QDs have been prepared using photochemical[101,107,123,124] or electrochemical "charging".[103,104,106] Until recently, aliovalent doping of semiconductor QDs to yield band-like charge carriers has proven difficult.

Recent reports of the preparation and subsequent characterization of colloidal Al^{3+}-doped ZnO (Al^{3+}:ZnO) QDs has been reported in which Al^{3+} acts as an ion-

ized shallow donor.[125] In these Al^{3+}:ZnO QDs, electronic absorption spectroscopy reveals excess band-like electrons, similar to photochemically charged ZnO (e^-:ZnO) QDs. Indeed, explicit comparison of the electron paramagnetic resonance (EPR) and electron absorption spectroscopies of Al^{3+}:ZnO and e^-:ZnO QDs show the two species as essentially indistinguishable when examined spectroscopically.[126] Yet despite this apparent indistinguishability, the two species show qualitatively different chemical reactivity—Al^{3+}:ZnO is completely stable against air oxidation, whereas e^-:ZnO rapidly oxidizes when exposed to air.[26,101,107,123,124,127] Furthermore, while it is possible to determine the number of conduction band (CB) electrons per QD in photochemically charged ZnO QDs via anaerobic titration,[29,128] the stability of Al^{3+}:ZnO QDs prevents such characterization. Instead, the number of CB electrons in Al^{3+}:ZnO QDs must be estimated via EPR and absorption spectroscopies. Near infrared absorption increases, for example, as more electrons are added to the ZnO QDs, or as more Al^{3+} is incorporated into the QDs.[126] Implicit to these techniques is the assumption that added CB electrons in the QDs behave similarly, whether the result of aliovalent doping or photochemical charging, that is, their electronic structure is, practically speaking, identical.

Here we report the theoretical characterization of the low-energy (ultraviolet, visible, near-infrared) electronic transitions of photochemically reduced ZnO and Al^{3+}:ZnO QDs using time-dependent hybrid density functional theory (TDDFT). We examine the electronic structure of the QDs using DFT, comparing the density of states for the two types of charged QDs. We explore the connection between our computed DFT results and the simple quantum mechanical particle in a spherical potential model.[129,130] Theoretical characterization of these electron transitions allows direct comparison between CB electrons and absorption spectroscopies for both types of QDs, as well as comparing the band-gap structure of both materials. This provides fresh insight into the electronic structure of the materials, suggesting that the band structure of aliovalently-doped and photochemically-charged ZnO QDs may not be as

similar as previously thought.

4.2 Methodology

All calculations were performed using the development version of the Gaussian program.[131] Quantum dot electronic structures were obtained using the PBE1PBE hybrid DFT functional.[95,96] The Los Alamos double-ζ pseudocore potential (LANL2DZ) and associated basis set were used for all atoms,[97–99] with Zn^{2+} ($3p$, $4s$, $3d$), O^{2-} ($1s$, $2s$, $2p$), H ($1s$), and Al^{3+} ($3s$, $3p$) electrons treated using explicit basis functions. Nearly-spherical ZnO quantum dots were constructed to have C_{3v} symmetry using the experimental lattice parameters: $a = 3.249$ Å, $c = 5.204$ Å, and $u = 0.382$ Å.[81] The resulting $Zn_{33}O_{33}$ and $Zn_{84}O_{84}$ structures have diameters (d_{QD}) of ∼1.2 and ∼1.8 nm, respectively. The aluminum dopant was introduced by replacing a lattice-bound Zn^{2+} near the quantum dot center with Al^{3+}. In accordance with previous theoretical methods,[90] pseudohydrogen atoms were used to passivate dangling bonds on the surface of the quantum dots; these atoms have modified nuclear charges of 0.5 and 1.5 to terminate surface O^{2-} and Zn^{2+}, respectively. The pseudohydrogen capping scheme leads to a well-defined bandgap and stable QD geometry. Replacing a Zn^{2+} lattice site with an Al^{3+} dopant was performed such that the total charge of the quantum dot remained neutral. Adding an additional electron to the ZnO QD resulted in a e^-:ZnO QD with a total charge of -1. Excited-state energies and oscillator strengths were calculated with the linear-response time-dependent density functional theory (TDDFT)[132] at the PBE1PBE/LANL2DZ level of theory, consistent with previous literature reports. Absorption spectra were obtained by dressing excited-state peaks with Gaussian functions with a broadening constant of 0.16 eV. To capture the broad shape of the first several frontier orbitals, an isosurface value of 0.007 was used for all orbital plots.

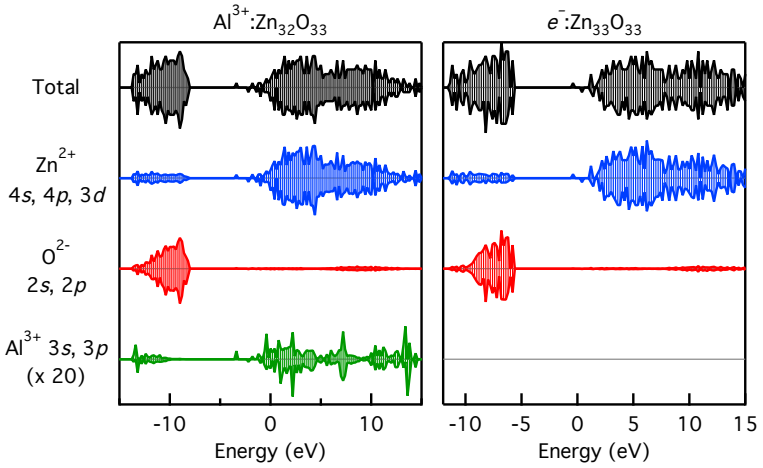

Figure 4.1. Total and projected density of states (DOS) for an e^-:$Zn_{33}O_{33}$ QD (right) and Al^{3+}:$Zn_{32}O_{33}$ QD (left) with an Al^{3+} dopant in the central lattice position. Positive and negative values represent the spin-up and spin-down DOS, respectively. Note the 20× magnification of the Al^{3+} projected DOS.

4.3 Results and Discussion

Figure 4.1 shows density of states (DOS) plots for the e^-:$Zn_{33}O_{33}$ QD and the Al^{3+}:$Zn_{32}O_{33}$ QD with an Al^{3+} dopant in the central lattice position obtained using one-electron orbitals from a ground state DFT calculation. The conduction band (CB) consists primarily of Zn^{2+} $4s$ and $4p$ character, and the valence band (VB) consists of mainly O^{2-} $2p$ character. The Al^{3+} dopant, which replaces a Zn^{2+} lattice position, is similar in character to the Zn^{2+} in the Al^{3+}:$Zn_{32}O_{33}$ DOS with the exception that the Al^{3+} contributions to the VB are deeper than the Zn^{2+} contributions; as a result, the valence band edge drops by ∼2 eV. In $Zn_{33}O_{33}$, the VB is completely full, and any additional electrons are added to the CB, as is the case for e^-:$Zn_{33}O_{33}$, in which the added e^-_{CB} occupies a state ∼5 eV above the valence band edge. In the Al^{3+}:$Zn_{32}O_{33}$ QD, the Al^{3+} dopant is a shallow donor that introduces an additional electron ∼4 eV above the valence band edge. While the added e^-_{CB} in e^-:$Zn_{33}O_{33}$ and

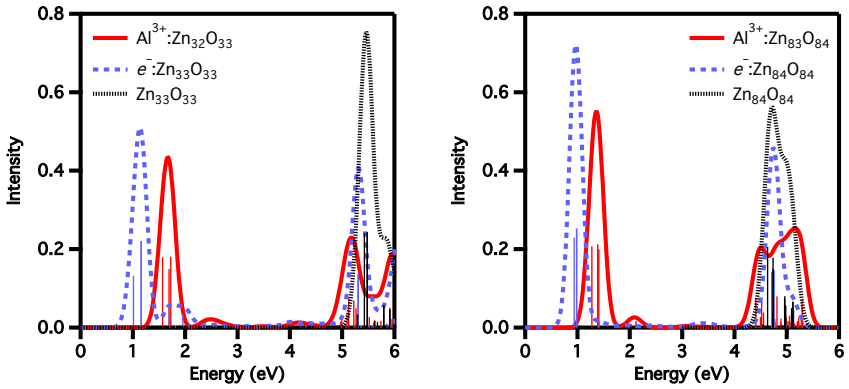

Figure 4.2. Absorption spectra of $Zn_{33}O_{33}$ QDs (left) and $Zn_{84}O_{84}$ QDs (right) containing a single Al^{3+} dopant (red solid line), a single added e^-_{CB} (blue dashed line), and a neutral, undoped QD (black dotted line). All spectra were computed at the TD-PBE1PBE/LANL2DZ level of theory. Vertical lines correspond to TDDFT excited-state energies and oscillator strengths. TDDFT peaks are dressed with Gaussian functions with a broadening parameter of 0.16 eV.

Al^{3+}:$Zn_{32}O_{33}$ is predominantly Zn^{2+} in character, the e^-_{CB} state in Al^{3+}:$Zn_{32}O_{33}$ also consists of Al^{3+} character, which serves to lower its energy by ∼1 eV compared to the e^-_{CB} state in e^-:$Zn_{33}O_{33}$. Despite small shifts in the band-edge potentials, these n-type Al^{3+}:$Zn_{32}O_{33}$ and e^-:$Zn_{33}O_{33}$ QDs exhibit similar electronic structures, and therefore the added electron due to the Al^{3+} dopant is nearly identical to the added electron found in the charged e^-:$Zn_{33}O_{33}$ QD.

Figure 4.2 shows electronic absorption spectra for $Zn_{33}O_{33}$ (1.2-nm diameter) and $Zn_{84}O_{84}$ (1.8-nm diameter) QDs obtained from linear-response TDDFT calculations. Spectra are included for neutral, undoped ZnO, Al^{3+}:ZnO, and e^-:ZnO QDs. All the QDs show characteristic VB to CB transitions starting at approximately 5.1 eV for the strongly quantum-confined 1.2-nm diameter QDs, and 4.3 eV for the 1.8-nm diameter QDs, where quantum confinement is more relaxed. In contrast to the ZnO QDs, in which only VB to CB transitions are observed, the n-type ZnO QDs display a sharp, lower-energy peak around 1.0 eV (1.1 eV) for the e^-:$Zn_{33}O_{33}$ (e^-:$Zn_{84}O_{84}$)

and 1.6 eV (1.4 eV) for the Al^{3+}:$Zn_{32}O_{33}$ (Al^{3+}:$Zn_{83}O_{84}$). The lowest-energy large peak for each of the n-type ZnO QDs consist of three electronic transitions—two of which are degenerate for the e^-:ZnO, and no degeneracies for the Al^{3+}:ZnO. A weak shoulder is also observed around 0.5–0.7 eV above the first peaks in the Al^{3+}:ZnO and e^-:ZnO spectra. As the QDs increase in size, the lower energy peaks for the different n-type ZnO QDs begin to approach each other energetically. In the 1.2-nm diameter QDs, they differ by around 0.5 eV. In the larger, 1.8-nm diameter QDs, they differ by 0.4 eV. The shoulders to the right of these peaks also decrease with increasing QD diameter, though less so for the Al^{3+}:ZnO QD.

The calculated spectra can be understood by treating the e^-_{CB} as a quantum mechanical particle in a spherical potential.[40,41] The electron is confined to the QD with a constant potential inside the QD, and a relatively large potential outside the QD. This quantum mechanical model is analytically tractable and has been solved in many a graduate textbook. The one-electron wave function, solved in spherical coordinates, is found to be a product of the spherical harmonic function $Y_l^m(\theta,\phi)$ and a spherical Bessel function of the first kind $j_n(r)$,

$$\Psi(r,\theta,\phi) = A_{n\ell} j_\ell(\beta_{n\ell} r/a) Y_\ell^m(\theta,\phi), \tag{4.1}$$

where $A_{n\ell}$ is a normalization constant, j_ℓ is the ℓ-th spherical Bessel function of the first kind, and $\beta_{n\ell}$ is the n-th zero of the ℓ-th spherical Bessel function. The spherical harmonic function simultaneously satisfies eigenvalue equations for the angular momentum and angular momentum projection operators, respectively

$$\hat{L}^2 Y_l^m(\theta,\phi) = l(l+1) Y_l^m(\theta,\phi), \qquad \hat{L}_z Y_l^m(\theta,\phi) = m Y_l^m(\theta,\phi) \tag{4.2}$$

where l is the angular quantum number and m is the projection of the angular momentum. In this model, the electron has energy levels that go according to only the

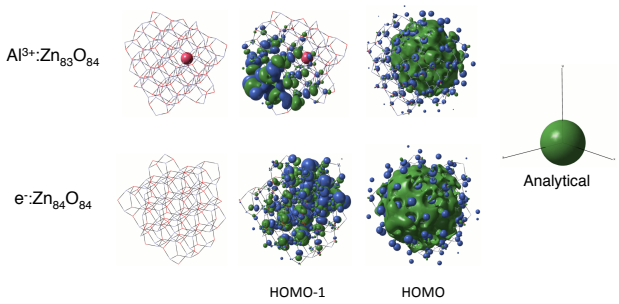

Figure 4.3. Structure of e^-:$Zn_{84}O_{84}$ and Al^{3+}:$Zn_{83}O_{84}$ QDs. For the Al^{3+}:$Zn_{83}O_{84}$, the Al^{3+} dopant is indicated by the magenta sphere. HOMO-1 and HOMO orbitals are shown for each QD, showing the valence band edge of the QD (HOMO-1), as well as the conduction band edge, which is occupied in both QDs (HOMO). The analytically-derived S-type spherical harmonic is plotted for comparison, as predicted using the particle in a spherical potential quantum model.

n and l quantum numbers of the wave function

$$E_{n,l} = \frac{\beta_{n,l}^2 \hbar^2}{2m_e^* R^2} \tag{4.3}$$

where R is the radius of the sphere, m_e^* is the effective mass of the electron, and $\beta_{n\ell}$ is again the n-th zero of the ℓ-th spherical Bessel function. Computation of these zeros has no general formula and must be done numerically. The wave functions for the particle-in-a-sphere are closely related to the solutions for the particle in a Coulombic potential (e.g., a hydrogen atom), with the only major difference being that the potential for the particle in a sphere goes as $\frac{1}{r^2}$, whereas the hydrogenic solutions go as $\frac{1}{r}$. The angular dependence is identical between the two models, and so the shape of the orbitals will look identical for a given radius R. Based on this model, QDs with CB electrons have been termed "artificial atoms", as they display s-, p-, d-,... type orbitals, referred to as S-, P-, D-,... type "super" orbitals.[130]

Figures 4.3 to 4.5 show the frontier and neighboring molecular orbitals (MOs) for

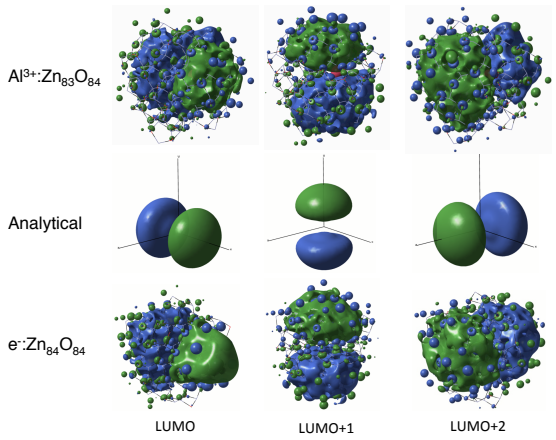

Figure 4.4. The first three unoccupied orbitals of the conduction band are shown for both e^-:$Zn_{84}O_{84}$ and Al^{3+}:$Zn_{83}O_{84}$ QDs. Analytical P-type spherical harmonics are plotted for comparison.

the Al^{3+}:$Zn_{83}O_{84}$ and the charged e^-:$Zn_{84}O_{84}$ QDs obtained from DFT. These are, to our knowledge, the first-ever published images of DFT-generated atom-like super orbitals in II-IV semiconducting QDs, supporting the treatment of CB electrons as S-, P-, D-,... type electrons arising from the spherical potential model. Figure 4.3 shows the highest-occupied molecular orbital (HOMO) and HOMO-1 for these two QDs, which reveal the difference in character between the bottom edge of the CB and the top edge of the VB for each QD, respectively. The HOMO-1 orbitals are localized to the lattice of the QD, as expected for bonding MOs, and show p-type character as expected from the DOS in Figure 4.1. The HOMO, which describes the free CB electron, shows S-type super orbital character, analogous to the analytic s-type spherical harmonic that is plotted for comparison. Only the spin-up MOs are given, but the filling of the orbitals follows similar to the filling of hydrogen-like orbitals, where opposite spin electron pairs fill each spatial MO. Once the S-type super orbitals are filled, the P-type super orbitals are filled, and so on. Because of the nearly centrosymmetric character of the QD, and the resemblance of the super

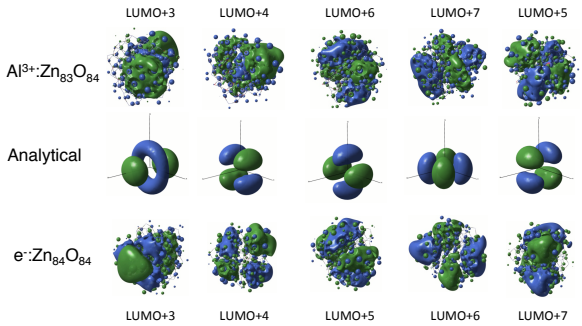

Figure 4.5. The lowest unoccupied molecular orbitals (LUMOs 3–7) corresponding to D-type super orbitals are shown. Analytically derived D-type spherical harmonics are plotted for comparison.

orbitals to the atomic orbitals, it is natural to expect that the doped QDs will show similar spectral properties as the hydrogen atoms they resemble. Figures 4.4 and 4.5 show the continued atom-like behavior of the first eight lowest unoccupied molecular orbitals (LUMOs) in both Al^{3+}:ZnO and e^{-}:ZnO QDs, which reveal their P- and D-type super orbital character.

Given this atomistic model of the CB states, we can begin to interpret the absorption spectra of the Al^{3+}:ZnO and e^{-}:ZnO QDs in Figure 4.2. Indeed, the spectral similarities become apparent once we compare their transition moment integrals. The transition moment integral for a transition from an initial state n to a final state l is given by the expression

$$\mu_{ln} = \langle \Psi_l | \, \hat{\mu} \, | \Psi_n \rangle. \tag{4.4}$$

For electrons moving in a centrosymmetric potential—for example the hydrogen atom or the "extra" electron in a quantum dot—the transition moment will be non-zero as long as the integral is symmetric; this is the well-known *Laporte rule*. The electron resides in an S-type super orbital, which has gerade (g) symmetry. The transition moment operator, $\hat{\mu}$, has ungerade (u) symmetry. Thus s–p transitions evaluate as $g \times u \times u = g$, and are allowed by symmetry. Contrasted with D-type super orbitals,

which have g symmetry, the transition moment integral evaluates as $g \times u \times g = u$, which is zero. Thus s–d transitions are forbidden in a centrosymmetric environment.

For both the Al^{3+}:ZnO and the e^-:ZnO QDs, the extra electron resides in the S-type super orbital (see the HOMO in Figure 4.3). The strong transitions around 1 to 2 eV correspond to S–P transitions, which the Laporte rule says is symmetry allowed. If the QDs were perfectly centrosymmetric, we would observe three degenerate S–P transitions. However, the QDs themselves are not perfectly centrosymmetric: the ZnO dots have C_{3v} symmetry, whereas the Al^{3+}:ZnO has none. For this reason, we see two S–P transitions for the e^-:ZnO, where the higher energy transition consists of two degenerate transitions from S to P_x and P_y. In the Al^{3+}:ZnO, there is no such symmetry, and we see three unique S–P transitions. The broken symmetry of the QDs also serves to explain the weak higher-energy shoulders next to these peaks, corresponding to weakly allowed S–D transitions. As the QDs increase in size, the ZnO dots become more spherical, and the effects of the centrosymmetric environment become more pronounced. As a result, the S–D transitions decrease in intensity. While the Al^{3+}:ZnO approaches spherical symmetry as it gets larger, it does so much more slowly due to the Al^{3+} impurity; as a result, the weakly allowed S–D transitions persist. The higher energy of the Al^{3+}:ZnO S–P transitions may be accounted for by the higher potential of the Al^{3+} center, as opposed to the ZnO structure. The electron has a greater Coloumbic attraction to the Al^{3+} center, of which the electron has a non-zero probability of occupying in the S-type orbital, as opposed to the P-type orbitals, which have a node at the Al^{3+} center. Thus it requires more energy for the electron to transition from S to P.

The reduction of symmetry in the Al^{3+}:ZnO may also explain the decrease in absorption intensity for the S–P transitions compared to the e^-:ZnO. Absorption intensity is proportional to the magnitude of the transition moment integral. For the reasons mentioned earlier, the Al^{3+}:ZnO QD's reduced symmetry weakly allows otherwise forbidden transitions (S–D), and it also decreases otherwise allowed transitions

(S–P). The argument is that the transition moment integral is maximized with a fully *gerade* function. On the other hand, the transition moment integral is minimized with a fully *ungerade* function. Thus for the Al^{3+}:ZnO, broken symmetry allows neither a fully *gerade* nor *ungerade* transition moment integral. As a result, we see increased intensity for otherwise forbidden transitions relative to the e^-:ZnO, and decreased intensity for otherwise allowed transitions relative to the e^-:ZnO.

In contrast to the *n*-type QDs, the neutral, undoped ZnO QD lacks these transitions due to its unoccupied S-type orbital. The only transitions observed are VB to CB transitions. It is interesting to note the trends in absorption intensity for the three systems. The uncharged ZnO has the strongest VB $\rightarrow$ CB transitions, followed by the charged e^-:ZnO, and finally the Al^{3+}:ZnO, which has the weakest transitions. These so-called bleaching trends, which have been observed in experiment,[102,126] may be understood by considering their respective density of states. For each system, the VB consists of mostly oxygen $2s$, $2p$ character and the CB consists of mainly zinc $4s$, $4p$, $3d$. Because band-to-band intensities are proportional to the density of states within these bands, introducing an extra electron into the ZnO reduces the density of states involved in band-to-band transitions by occupying an otherwise vacant position in the CB. Similarly, adding an Al^{3+} dopant removes a zinc state in the valence band edge (replaced by p states deeper than the valence band edge), reducing the density of states available for band-to-band transitions. By this argument, we expect that as the concentration of Al^{3+} increases, the electronic transition intensity should decrease.

4.4 Conclusion

In this work we present a theoretical comparison of two different *n*-type ZnO QDs, which contain an added electron in the conduction band. The two QD types include: Al^{3+}:ZnO whose added electron originates via aliovalent doping with Al^{3+}, which introduces a e^-_{CB} while maintaining a neutral charge on the QD; and e^-:ZnO whose

added electron can be introduced via photochemical reduction[101,107,123,124] or chemical techniques[108] resulting in a QD with a single negative charge. We find that in general both systems have similar electronic absorption spectra, with most of the general features accounted for by the quantum mechanical model of the particle in a spherical potential. That is to say, the added electron occupies an S-type orbital, and has three (near-degenerate) strong transitions to P-type orbitals, analogous to *s*–*p* transitions in hydrogen atoms. While both QD systems have similar spherical symmetry, they are not perfectly centrosymmetric, with the Al^{3+}:ZnO having the greatest extent of broken symmetry. This is evidenced by the off-center Al^{3+}:ZnO S-type orbital seen in Figure 4.3, compared to the e^-:ZnO S-type orbital. This results in three non-degenerate *s*–*p* transitions for the Al^{3+}:ZnO, compared to the e^-:ZnO, which has a degeneracy in its S–P transitions. Additionally, the reduced symmetry in Al^{3+}:ZnO lowers (raises) the intensity of S–P (S–D) transitions relative to e^-:ZnO that would otherwise be allowed (forbidden) in a centrosymmetric system. Finally, doping with Al^{3+} introduces a positively charged center in the Al^{3+}:ZnO QD, which must be overcome in S–P type transitions. Because the P-type orbitals have a node at the Al^{3+} center, additional energy to overcome the Coulombic attraction between the electron and the Al^{3+} center results in a higher energy transition relative to e^-:ZnO.

Three generalizations can be made. First, broken symmetry of the aliovalently-doped Al^{3+}:ZnO reduces the absorption intensity of allowed transitions relative to e^-:ZnO. With low dopant concentrations and in the large QD limit, the Al^{3+}:ZnO and the e^-:ZnO should show near-identical spectra as they both approach spherical symmetry. Second, broken symmetry in the Al^{3+}:ZnO allows for transitions that would otherwise be forbidden in a centrosymmetric environment. This is corollary to the first point: as the Al^{3+}:ZnO QD gets larger, or has a lower dopant concentration, its centrosymmetric symmetry increases and its absorption spectrum matches that of e^-:ZnO. Finally, increased dopant concentration in Al^{3+}:ZnO, where Al^{3+} acts as an ionized shallow donor, results in higher energy transitions relative to e^-:ZnO, on

account of the increased Coulombic attraction between the added electrons and the Al^{3+} centers. Thus comparing spectra for aliovalently doped and photochemically charged ZnO QDs must take into account size of the QDs and the concentration of dopants when comparing the number of free electrons in the QD.

Chapter 5

EFFECT OF EXCITED STATE STRUCTURAL RELAXATION ON MID-GAP EXCITATIONS IN CO^{2+}-DOPED ZNO QUANTUM DOTS

The unique mid-gap excited states of Co^{2+}-doped ZnO quantum dots have given rise to new applications in photocatalysis, sensing, magneto-optics, and magneto-electronics. However, the electronic characteristics of these mid-gap transitions are not fully understood, and the uncertain interplay between these transitions has led to disagreement in the literature. In this chapter, mid-gap excited states of Co^{2+}-doped ZnO quantum dots are analyzed using linear response time-dependent density functional theory and the effective mass theory with a focus on the geometry relaxation in the donor-type photoionization excited state. Relaxation of the excited-state geometry lowers the charge-transfer transition energy to be in the vicinity of the prominent spin-allowed $^4A_2 \rightarrow {}^4T_1$ Co^{2+} *d*–*d* transition that gives this material its characteristic color. For large quantum dots, the excited-state population distribution between this Co^{2+} *d*–*d* excited state and the charge-transfer excited state can be tuned by thermal energy, resulting in a unique temperature dependence of the luminescence and photoconductivity.

5.1 Introduction

Semiconducting materials doped with transition metal ions have attracted broad interest due to their applications in photocatalysis, photovoltaics, and spin electronics.[3–5,10–13,17,22,24] For Co^{2+}-doped ZnO (Co^{2+}:ZnO), these applications are strongly influenced by the material's complex electronic structure, which derives from the fact

that the Co^{2+} $3d$ levels are located within the band gap of the ZnO semiconductor host. This feature gives rise to new spectral bands in the visible energy region, including ligand-field (d–d) transitions centered at the dopant, and charge-transfer (CT) bands. These CT bands, frequently referred to as donor- and acceptor-type photoionization transitions, involve the promotion of a localized Co^{2+} d electron into a delocalized conduction-band (CB) orbital, referred to as metal-to-ligand charge transfer ($ML_{CB}CT$), or promotion of a valence-band (VB) electron into a localized Co^{2+} d orbital, referred to here as a ligand-to-metal charge transfer ($L_{VB}MCT$) transition.[35] However, the electronic characteristics of these mid-gap transitions are not fully understood, and the uncertain assignment of the energies of these transitions in Co^{2+}:ZnO has led to disagreement in the literature.

The electronic structure of Co^{2+}-doped ZnO has been investigated extensively at both the fundamental level and in relation to potential spin-based electronics applications.[133–136] Despite extensive research, the characteristics and interplay of its dopant-centered mid-gap electronic excited states remain unclear. Kanai and co-workers first reported room-temperature mid-gap photoconductivity in Co^{2+}:ZnO following Co^{2+} d–d excitation to the broad and structured $^4A_2 \rightarrow {}^4T_1(P)$ band centered at ∼2.0 eV.[137] From this observation, it was concluded that the Co^{2+} $^4T_1(P)$ manifold must reside "near or in the conduction band of ZnO" so that the photoexcited Co^{2+} d electron can relax to the $ML_{CB}CT$ band and give rise to the observed photocurrent. This observation is not easily reconciled with subsequent observations of photoluminescence from the same d–d band,[138,139] which might suggest instead that the Co^{2+} $^4A_2 \rightarrow {}^4T_1(P)$ d–d transition lies below the $ML_{CB}CT$ threshold.[139] Recent studies of Co^{2+}:ZnO epitaxial films have identified the source of this discrepancy by showing a strong dependence of d–d photoconductivity on both temperature and Co^{2+} concentration, leading to a picture in which the $^4T_1(P)$ excited state is slightly above the $ML_{CB}CT$ state at low Co^{2+} concentrations (∼0.8%) but below the $ML_{CB}CT$ state at higher concentrations (∼11%), allowing the former to show d–d photoconductivity but not the latter.[140,141]

For all concentrations, the *d*–*d* photoconductivity is thermally activated, with an activation barrier for electron ionization to the ZnO CB that depends on the Co^{2+} concentration. These results illustrate the complexity of the electronic structure of this experimentally well-studied material.

A number of theoretical efforts have been carried out to understand the electronic structure of Co^{2+}:ZnO as well, including the energies and characteristics of its mid-gap excited states.[142–145] Excitations in condensed matter are often approximated as the difference in orbital energies for the occupied and unoccupied (or virtual) orbitals obtained from ground-state density functional theory (DFT) calculations.[143,146] This method gives reasonable results for systems with moderate correlation and small electron-hole binding energies. Linear response time-dependent density functional theory (TDDFT) provides a more accurate assessment of excited-state energies and wave functions, and TDDFT has been applied recently to describe the excited-state electronic structures of Co^{2+}:ZnO quantum dots (QDs).[35,90] These TDDFT studies predict the Co^{2+} *d*–*d* excitation to be located below the $ML_{CB}CT$ band in these QDs, but neglect the important role played by nuclear relaxation upon electronic excitation. Addressing the role of structural relaxation on the excited state may provide a better understanding of the mid-gap transitions, and hence, the physical properties of this important material.

In this work, we present a theoretical analysis of the excited-state structural relaxation pathways, energy levels, and mechanisms governing the photoconductivity and luminescence in Co^{2+}:ZnO QDs following ligand-field excitations. The results account for the explicit role of nuclear relaxation in the *d*–*d* and $ML_{CB}CT$ excited states.

5.2 Methodology

All calculations were performed with the development version of the Gaussian program.[93] Nanocrystal electronic structures were obtained with the PBE1PBE hybrid

DFT functional.[94–96] The Los Alamos double-ζ pseudo-core potential (LANL2DZ)[97,99,147] and the associated basis set were used for the ZnO lattice with the Zn ($4s$, $3d$) and O ($1s$, $2s$, $2p$) atomic orbitals treated with explicit basis functions. Cobalt dopants were modeled with the Los Alamos valence triple-ζ pseudo-core potential (LANL2TZ) and basis set.[148] The electronic excited-state energies and wave functions of Co^{2+}:ZnO QDs were calculated using TDDFT within the linear response framework. Absorption spectra were obtained by dressing the excited-state peaks resulting from the TDDFT calculation with Gaussian functions having a broadening constant of 0.16 eV to best fit the experimental data. Nearly spherical wurtzite ZnO nanocrystals, $Zn_{21}O_{21}$ (diameter ∼0.7 nm), $Zn_{33}O_{33}$ (diameter ∼1.2 nm), and $Zn_{84}O_{84}$ (diameter ∼2.0 nm) were constructed according to the previously published scheme.[35,90] The dangling bonds on the surface of the nanocrystals were passivated with pseudo-hydrogen atoms having modified nuclear charges of 0.5 and 1.5 to terminate surface O^{2-} and Zn^{2+} ions, respectively. Excited-state geometry optimizations were performed within the TD-PBE1PBE/LANL2DZ level of theory, following the excited-state gradients.

5.3 Results and Discussion

Figure 5.1a shows the density of states (DOS) diagram calculated for a $Zn_{32}CoO_{33}$ QD showing a filled VB and empty CB separated by a gap of $E_g \sim 5.8$ eV, larger than the bulk band gap of ∼3.4 eV due to quantum confinement. Also shown in the DOS diagram is the contribution of the Co^{2+} $3d$ electrons. In the pseudotetrahedral crystal field of wurtzite ZnO, the Co^{2+} $3d$ electrons with the same spin are split by symmetry into two lower energy d_e and three higher energy d_{t_2} orbitals, whereas exchange interactions lead to the splitting between electrons with different spins. The ground state of Co^{2+} is a high-spin d^7 ($S = \frac{3}{2}$) configuration. Whereas, all of the Co^{2+} spin-up $3d$ levels are covalently delocalized into the VB of the semiconductor, the spin-down electrons are much more localized appearing ∼1 eV above the edge of the ZnO VB. These results agree well with experimental photoemission data.[149–151]

The new states introduced into the ZnO band gap by the Co^{2+} dopant give rise to new, lower-energy excitations as seen in the absorption spectra in Figure 5.1c. These new transitions are characterized in the schematic in Figure 5.1b, and have been previously well characterized.[35,140] Figure 5.1c shows the absorption spectrum for a $Zn_{32}CoO_{33}$ QD (3% Co^{2+}:ZnO) and a $Zn_{31}Co_2O_{33}$ QD (6% Co^{2+}:ZnO) of 1.2 nm diameter calculated with the linear response TDDFT approach,[152] compared to that of a pure $Zn_{33}O_{33}$ QD. The two lowest-energy absorption bands (at ∼0.8 and ∼1.85 eV) correspond to the Co^{2+} $^4A_2 \rightarrow {}^4T_1$(F) and $^4A_2 \rightarrow {}^4T_1$(P) ligand-field transitions, respectively. These transitions have non-zero oscillator strengths as a result of hybridization (covalency) with the ZnO lattice. The excitation energies are essentially independent of QD diameter, whereas the oscillator strengths are dependent on the dopant concentration. The shoulder in the higher mid-gap energy region (starting at ∼4.1 eV) results from the $ML_{CB}CT$ transitions, which split into two sub-bands, MLCT1 and MLCT2. These two sub-$ML_{CB}CT$ bands correspond to excitations of Co^{2+} d_e and d_{t_2} electrons to the ZnO CB, respectively. For detailed characteristics of these transitions, we refer readers to our previous theoretical work on the absorption spectra of doped ZnO QDs.[35,38] For the $Zn_{32}CoO_{33}$ QD of 1.2 nm diameter, the highest *d*–*d* and the lowest $ML_{CB}CT$ vertical excitations are separated by ∼2.3 eV. This amount of energy cannot be compensated by room-temperature thermal activation. As a result, theoretical predictions of the vertical excitations of smaller QDs cannot explain the photoconductivity following excitation to the $^4T_1$ *d*–*d* excited state.

As the QD diameter increases, the energetic separation between the Co^{2+} *d*-*d* and $ML_{CB}CT$ bands will change possibly leading to an energetic crossover. The Co^{2+} *d*-*d* excitation is localized and independent of QD diameter. The $ML_{CB}CT$ band intrinsically depends on the CB levels, which decrease in energy with increasing QD diameter due to quantum confinement. As a result, the energetic separation between the Co^{2+} *d*-*d* and $ML_{CB}CT$ bands will decrease as the QD diameter increases. This phenomenon can be understood using the effective mass approximation for a spherical

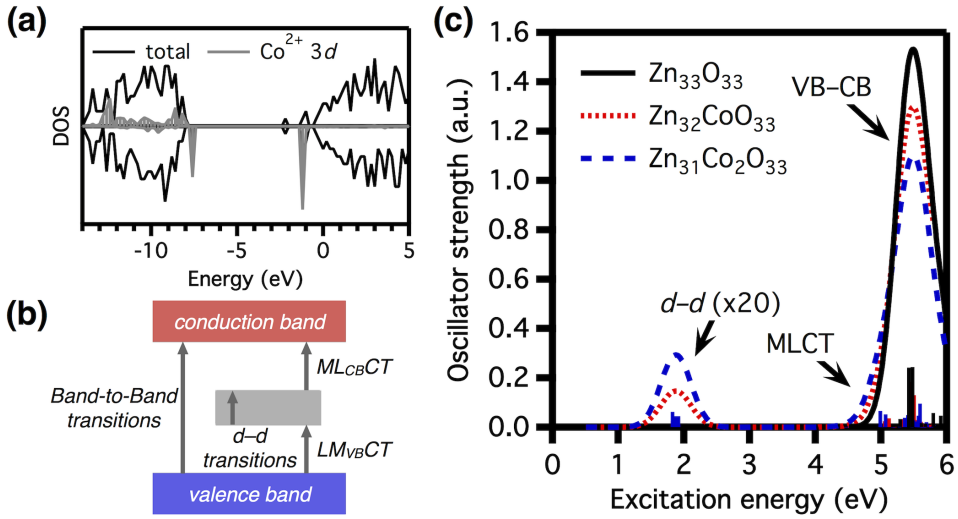

Figure 5.1. (a) Density of states (DOS) diagram calculated for a $CoZn_{32}O_{33}$ QD. The shaded region shows the Co^{2+} $3d$ contribution to the DOS diagram magnified by 5×. Spin up, positive density values; spin down, negative density values. (b) Schematic illustration of the optical transitions observed in Co^{2+}:ZnO. Note that, experimentally, the $L_{VB}MCT$ and $ML_{CB}CT$ transition energies do not sum to the band-to-band transition energy as they are depicted because of large electron-electron repulsion effects at the Co^{2+} dopant. (c) TDDFT absorption spectra of a pure $Zn_{33}O_{33}$ QD (solid black curve), a $Zn_{32}CoO_{33}$ QD with one Co^{2+} dopant (dotted red curve), and a $Zn_{31}Co_2O_{33}$ QD with two Co^{2+} dopants (dashed blue curve). The $^4A_2 \rightarrow {}^4T_1(P)$ bands at ∼2 eV are magnified 20 fold. The line shape functions were obtained by fitting the calculated spectral lines with Gaussian functions having a line broadening parameter of 0.16 eV.

QD.[35,41] In the absorption spectrum, energy shifts of the $ML_{CB}CT$ band, ΔE_{MLCT}, and the band-to-band excitonic transition, ΔE_{EXC}, compared to those in bulk ZnO, take on the approximate relationship

$$\frac{\Delta E_{MLCT}}{\Delta E_{EXC}} \approx \frac{m_e^{*-1}}{m_e^{*-1} + m_h^{*-1}}, \tag{5.1}$$

where m_e^* and m_h^* are the effective masses (in units of electron mass) of the electron and hole in Co^{2+}:ZnO. The effective mass of the electron has been approximated to be 0.59 and 0.72 for MLCT1 and MLCT2, respectively, in Co^{2+}:ZnO.[35]

Equation (5.1) can be used to extrapolate the energy of the $ML_{CB}CT$ band to the bulk limit. Figure 5.2 shows the extrapolation using Equation (5.1) of the MLCT1 absorption transition to the bulk band gap limit of 3.4 eV for ZnO. The validity of Equation (5.1) is confirmed by calculations on QDs with different diameters. In the same figure, the *d*–*d* absorption is also plotted. This transition energy appears fixed, independent of QD diameter, consistent with its highly localized orbital nature. At the bulk band gap limit of 3.4 eV, the MLCT1 excitations still occur much higher in energy than the *d*–*d* transitions—almost 40 times k_BT at room temperature without structural relaxation. By taking into account the nuclear relaxation of the excited state, the energy difference between the $ML_{CB}CT$ and $^4T_1$ *d*–*d* bands is still 10 times k_BT at room temperature. An energy level scheme like this would be consistent with photoluminescence from the *d*–*d* excited state back to the ground state, while ruling out the possibility of photoconductivity. Experimentally, however, photoconductivity was observed in 4% Co^{2+}:ZnO epitaxial films following $^4A_2 \rightarrow {}^4T_1(P)$ excitation even at 27 K.[140] This observation implies that a relaxation pathway must exist for the *d*–*d* excited state population to be transferred to the $ML_{CB}CT$ excited state.

We hypothesize that a $ML_{CB}CT$ relaxation pathway could possibly arise from electron-nuclear coupling, which causes geometry relaxation on the excited-state potential energy surface (PES). Such a relaxation pathway will make vertical absorption transition energies different from the equilibrium excited-state energies relevant to the population thermalization of the experimental observations. To test this hypothesis, the excited-state structures were fully optimized at the TD-PBE1PBE level of theory. Figure 5.3 shows the changes in the excited-state geometries after the lattice relaxes to minimize the excited-state energy. The MLCT1 transitions formally promote an electron from Co^{2+} to the CB of ZnO, resulting in a charge state approaching Co^{3+} ($d_{t_2}^2$ configuration), and should induce a contraction of the Co–O bonds in this excited state. Our TDDFT results show that all Co–O bonds shorten by ∼0.1 Å in this MLCT1 excited state relative to the ground state, lowering the overall MLCT1

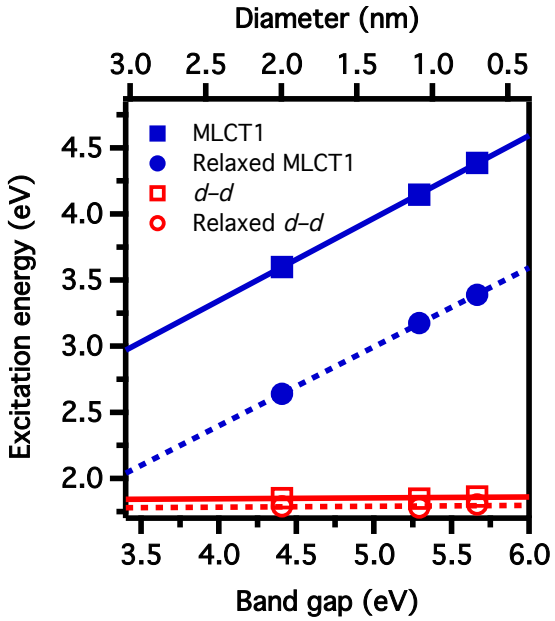

Figure 5.2. Calculated MLCT1 (□, ◯) and Co^{2+} *d*–*d* (■, ●) transition energies for Co^{2+}:ZnO QDs of decreasing diameter (2.0, 1.2, and 0.7 nm from left to right), plotted against the first excitonic transition energy and extrapolated to the bulk band gap limit of 3.4 eV. For the MLCT1 and *d*–*d* transitions, the excitation energies at the ground-state geometry (solid lines) and at the optimized excited-state geometry (dashed lines) are included.

energy by ∼1 eV. By comparison, the nuclear relaxation in the *d*–*d* excited state is much smaller, corresponding to substantially less energy stabilization (∼0.05 eV in the 1.2 nm QD). For the small QDs considered here (diam. = 0.7, 1.2, and 2.0 nm), the fully relaxed minima of the MLCT1 and *d*–*d* excited states are still energetically well separated, attributed to the large quantum confinement energies in these very small nanocrystals. From Equation (5.1), relaxation of this quantum confinement by increasing the QD diameter to approach the bulk limit will shift the MLCT1 excited state downward toward the *d*–*d* excited state. As shown in Figure 5.2, the MLCT1 electronic energies in their fully optimized excited-state geometries follow the prediction of the effective mass theory in Equation (5.1), whereas the *d*–*d* excited-state

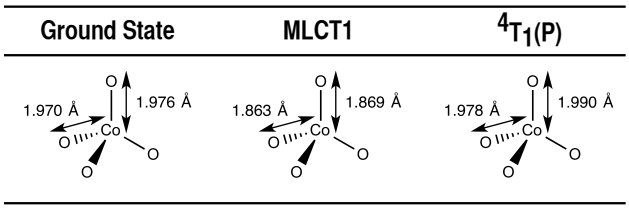

Figure 5.3. A comparison of the MLCT and Co^{2+} *d*–*d* excited-state geometries for a $Zn_{32}CoO_{33}$ QD before and after relaxation of the lattice to the respective excited-state minimum.

energies are fixed, independent of quantum confinement. The MLCT1 electronic origin is predicted to red shift to ∼2.0 eV at the bulk band gap limit of 3.4 eV, slightly higher (∼0.15 eV) in energy than the vertical *d*–*d* transitions and in generally good agreement with the energy of ∼0.1 eV estimated from experiment.[140,141]

The energies presented above relate to relaxation of the *d*–*d* and $ML_{CB}CT$ excited states along their independent nuclear reorganization coordinates, which are shown schematically in Figure 5.3. Thermally activated transitions between these two excited states, as seen experimentally,[140,141] arise from local lattice vibrations that connect these two geometries. Figure 5.4 shows the *d*–*d* and MLCT1 excited-state PESs of the ∼2.0 nm QD ($Zn_{84}O_{84}$) plotted along the MLCT1 nuclear relaxation coordinate, represented by the average Co–O bond length, $R(\text{Co–O}_{\text{avg}})$. In the equilibrium geometry of the ground state, $R(\text{Co–O}) = 1.972$ Å. In the relaxed *d*–*d* excited state, R(Co–O) shows a ∼0.01 Å deviation from the ground state bond length. In the relaxed MLCT1 state, however, R(Co–O) contracts to 1.86–1.87 Å and results in a nuclear reorganization energy of ∼0.5 eV. This large nuclear reorganization is responsible for the broad spectral distribution of the $ML_{CB}CT$ transition intensities observed experimentally.[140,141] Figure 5.4 also plots the MLCT1 PESs estimated for different degrees of quantum confinement using the effective mass approximation of Equation (5.1). In the bulk limit, the MLCT1 PES crosses that of the $^4T_1(P)$ *d*–*d* excited state. Thermal population of this MLCT1 PES will favor charge separation

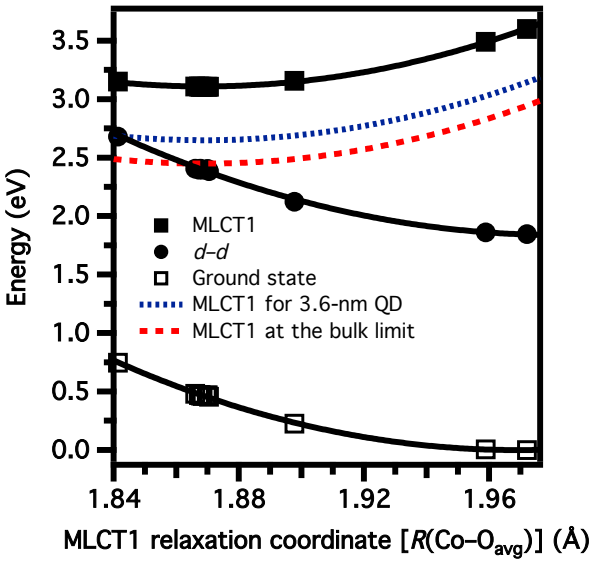

Figure 5.4. Potential energy surfaces of the ground, *d*–*d*, and MLCT1 excited states for a $Zn_{83}CoO_{84}$ QD (diam. ∼2.0 nm) plotted along the effective MLCT1 nuclear reorganization coordinate, represented here as $R(\text{Co–O}_{\text{avg}})$.

and reduce *d*–*d* luminescence. Equation (5.2) describes the relationship between the shift in the $ML_{CB}CT$ energy and the photoexcited electron's effective mass,[35]

$$\Delta E_{\text{MLCT}} \approx \frac{\hbar^2\pi^2}{2r^2}\left[\frac{1}{m_e^*}\right] - \frac{1.8e^2}{\varepsilon r} \tag{5.2}$$

where the Coulomb interaction between the photogenerated CB electron and localized hole has been neglected. Using an effective mass of $m_e^* = 0.59$ in Equation (5.2), we compute a critical QD diameter of ∼3.6 nm at which the $ML_{CB}CT$ PES will cross the Co^{2+} $^4T_1(P)$ PES at the $ML_{CB}CT$ equilibrium geometry.

5.4 Conclusion

Figure 5.4 is helpful for interpreting the experimental observations related to photoconductivity and luminescence quenching in Co^{2+}:ZnO. In small QDs, quantum

confinement leads to higher-energy $ML_{CB}CT$ excited states that are not thermally accessible from the $^4T_1(P)$ state. In large QDs and bulk Co^{2+}:ZnO, these states are shifted closer to the *d*–*d* excited state. In all cases, excited-state nuclear relaxation stabilizes the $ML_{CB}CT$ excited state by ∼0.5 eV, bringing it much closer to the *d*–*d* excited-state energy. Photoluminescence from the $^4T_1(P)$ state thus becomes more favorable with increasing quantum confinement and lower temperature, whereas *d*–*d* photoconductivity shows the opposite trends. These computational results complement recent experimental interpretations and furthermore provide new insights into possible mechanisms for tuning the interplay between the delocalized $ML_{CB}CT$ photoionization excited states and the localized ligand-field excited states of Co^{2+}:ZnO, which may be of interest for photocatalytic reactions or other photoinduced charge separation applications.

Chapter 6

TRANSITION STATE SEARCH USING A GUIDED DIRECT INVERSION IN THE ITERATIVE SUBSPACE METHOD

A transition state optimization method using a guided energy-represented direct inversion in the iterative subspace (gEn-DIIS) algorithm is introduced and compared with the quasi-Newton rational function optimization (RFO) method. A hybrid technique that employs a combination of RFO and guided DIIS methods at various stages of convergence is presented. A set of test molecules is optimized for comparison using the hybrid method with gEn-DIIS and the traditional RFO methods. The gEn-DIIS method presented here exhibits fast optimization and is shown to be advantageous for difficult optimizations where the reaction path is flat. The work presented in this chapter is reproduced with permission from May, J. W.; Lehner, J. D.; Frisch, M. J.; Li, X. *J. Chem. Theory Comput.* **2012**, *8*, 5175–5179.

6.1 Introduction

Molecular geometry optimization underlies any computational chemistry study by providing characteristic stationary point structures and energies on potential energy surfaces (PESs). The valleys or minima along the PES correspond to reactants, intermediates, and products. The reaction valley connecting two minima of the potential energy surface can be represented by the so-called reaction path, and first-order saddle points (where the second-order energy variation is positive with respect to all the coordinates except one along which the variation is negative) give rise to transition

states (TS). Well-characterized TS structures are essential for computing reaction barriers and reaction rates. Unfortunately, the landscape of the PES is not known during an optimization, thus requiring the use of various tools for exploring the PES and locating the stationary points. Among the most widely used tool in optimization is the Newton-Raphson method and its many variations,[153] including the rational function optimization (RFO)[154,155] and the trust radius method (TRM).[156–162] These techniques make use of the gradient and the Hessian of the PES to get information regarding the slope and local curvature at a given point along the PES. However, explicit computation of the Hessian can be unworkable for larger systems.

Least-squares minimization schemes such as the direct inversion in the iterative subspace (DIIS),[163,164] have proven efficient at converging wave functions[163–167] and molecular geometries.[168,169] As applied to geometry optimization, the DIIS method computes a new geometry closer to the stationary point by interpolating/extrapolating a set of position vectors obtained from previous steps such that the estimated error associated with the new position is at a minimum. The error from each step is usually estimated from the RFO step (RFO-DIIS),[169] $\Delta\mathbf{x} = -(\mathbf{H} - \lambda\mathbf{I})^{-1} \cdot \mathbf{g}$, but alternate methods have used an energy representation (En-DIIS)[170,171] of the local PES in the vicinity of previously computed points to estimate the error. Furthermore, a hybrid optimization scheme that combines the benefits of RFO, RFO-DIIS, and En-DIIS has been shown to give fast and smooth convergence for optimizing to a minimum.[170]

Unlike a geometry minimization, in which all coordinates are treated equally, a TS search identifies a particular linear combination of coordinates, the reaction pathway, along which the energy is to be maximized. While the methods outlined above can successfully locate minima on a PES, the success of a TS optimization strongly depends on the researcher's chemical intuition in providing a suitable initial guess for the structure. This difficulty arises from the small radius of the quadratic region about the stationary point compared to that of an equilibrium structure.[153] Additionally, an accurate Hessian matrix is required and must contain an eigenvector with

a negative eigenvalue that corresponds to the reaction pathway. For small systems in which movement along only a single coordinate gives rise to the TS, coordinate driving[172,173] and eigenvector following[154,174–176] algorithms have proven successful. Linear and quadratic synchronous transit (LST and QST)[177,178] and synchronous transit-guided quasi-Newton (STQN)[179] methods have provided a means for determining a TS starting structure by initially finding the maximum point along a path interpolated between the reactant and product minima. Path optimization[180] or chain-of-states methods[181] such as the elastic band theory[182] have been successful at not only locating TS structures, but also elucidating the reaction path connecting the reactant and product molecules. The nudged elastic band (NEB) method[183–187] and the growing strings method[188,189] both minimize the energy of a series of points (referred to as images) along an interpolated pathway connecting two minima. The cost of the many energy and derivative calculations required to minimize all the images makes these methods undesirable for larger systems. More recently, Jensen has proposed the use of empirical force fields for generating PESs of the reactant and product molecules and identifying the minimum along the seam of their intersection.[190]

In this work, we introduce a guided energy-represented DIIS (gEn-DIIS) method for TS search. We also propose a hybrid optimization scheme that makes use of the RFO, RFO-DIIS, and En-DIIS methods at various stages of the optimization. We employ a weighting factor in the DIIS optimization to rapidly reduce the error along the reaction pathway. This guided DIIS method continues to benefit from the speed of local search methods while making use of the unique nature of the TS structure.

6.2 Methodology

Within the RFO scheme, the optimization step taken in the DIIS method can be written as

$$\mathbf{R}_{k+1} = \mathbf{R}_k^* + \Delta\mathbf{R}_k^* = \sum_{i=1}^{k} c_i \mathbf{R}_i - \sum_{i=1}^{k} c_i (\mathbf{H} - \xi)^{-1} \cdot \mathbf{g}_i \tag{6.1}$$

In Equation (6.1), the first and second terms, $\mathbf{R}_k^* = \sum_{i=1}^{k} c_i \cdot \mathbf{R}_i$ and $\Delta\mathbf{R_k}^* = -\sum_{i=1}^{k} c_i(\mathbf{H}-\xi)^{-1} \cdot \mathbf{g}_i$, are the linear and quadratic steps obtained from extrapolation/interpolation of the previous vectors and RFO optimization steps, respectively. The set of coefficients $\{c_i\}$ minimize an error function in the multi-dimensional least-squares framework. In the context of geometry optimization, the error function can be a measure of energy ΔE, gradient $\mathbf{g}$, or optimization step $\Delta\mathbf{R}$. The DIIS scheme can be written in matrix form as

$$\begin{pmatrix} a_{1,1} & \cdots & a_{1,k} & 1 \\ \vdots & \ddots & \vdots & \vdots \\ a_{k,1} & \cdots & a_{k,k} & 1 \\ 1 & \cdots & 1 & 0 \end{pmatrix} \begin{pmatrix} c_1 \\ \vdots \\ c_k \\ \lambda \end{pmatrix} = \begin{pmatrix} 0 \\ \vdots \\ 0 \\ 1 \end{pmatrix} \tag{6.2}$$

where λ is the Lagrangian multiplier that satisfies the constraint $\sum_{i=1}^{k} c_i = 1$. With no constraint on the sign of c_i, the DIIS solution gives rise to either extrapolation or interpolation in the search space. When the molecular geometry is far from convergence, extrapolations can lead to erroneously large steps away from the optimized geometry. To ensure optimization stability, an enforced interpolation constraint, $c_i > 0$, is added when solving Equation (6.2) (for further details, see Ref. 166).

In our previous work,[167,171] we derived an energy-represented least squares minimization method where the error function is defined as

$$f = \frac{1}{2} \sum_{i,j,=1}^{k} c_i c_j \left[\frac{1}{2} \left(\mathbf{g}_i^T \cdot \mathbf{H}^{-1} \cdot \mathbf{g}_i + \mathbf{g}_j^T \cdot \mathbf{H}^{-1} \cdot \mathbf{g}_j \right) + \left(\mathbf{R}_i^T \cdot \mathbf{g}_j + \mathbf{R}_j^T \cdot \mathbf{g}_i - \mathbf{R}_i^T \cdot \mathbf{g}_i - \mathbf{R}_j^T \cdot \mathbf{g}_j \right) \right] \tag{6.3}$$

In Equation (6.3), the first set of terms in the bracket gives rise to energy errors of the search space relative to the minimum of the local quadratic surface. The second set of terms describes variations in energy for changes of coordinate and gradient vectors

within the search space. As the error function in Equation (6.3) is quadratic with respect to the $\{c_i\}$, minimization can be performed in a least squares sense using Equation (6.2), where

$$a_{i,j} = \frac{1}{2}\left(\mathbf{g}_i^T \cdot \mathbf{H}^{-1} \cdot \mathbf{g}_i + \mathbf{g}_j^T \cdot \mathbf{H}^{-1} \cdot \mathbf{g}_j\right) + \left(\mathbf{R}_i^T \cdot \mathbf{g}_j + \mathbf{R}_j^T \cdot \mathbf{g}_i - \mathbf{R}_i^T \cdot \mathbf{g}_i - \mathbf{R}_j^T \cdot \mathbf{g}_j\right) \tag{6.4}$$

An optimization scheme using Equations (6.1) to (6.4) will be referred to as En-DIIS. This method has consistently shown smooth and fast optimization for locating local minimum structures.[167] When the subject of interest is a transition state instead of a minimum, one of the eigenvalues of the Hessian needs to be of negative sign. In other words, the optimizer searches for the maximum along one and only one vector (the reaction path), while minimizing the energy along the remaining coordinates. In order to maintain the correct optimization direction, the TS search scheme introduced here is performed in the eigenspace of the Hessian, where the number of negative eigenvalues can be verified as the optimization proceeds. The gradient and coordinate vectors may be transformed using the Hessian eigenvectors as such

$$\mathbf{H} = \mathbf{C} \cdot \epsilon \cdot \mathbf{C}^\dagger \tag{6.5}$$

$$\tilde{\mathbf{g}}_i = \mathbf{C}^T \cdot \mathbf{g}_i \tag{6.6}$$

$$\tilde{\mathbf{R}}_i = \mathbf{C}^T \cdot \mathbf{R}_i \tag{6.7}$$

where ϵ is a diagonal matrix containing the force constants. In the normal coordinate system, Equation (6.4) becomes

$$\tilde{a}_{i,j} = \frac{1}{2}\left(\tilde{\mathbf{g}}_i^T \cdot \epsilon^{-1} \cdot \tilde{\mathbf{g}}_i + \tilde{\mathbf{g}}_j^T \cdot \epsilon^{-1} \cdot \tilde{\mathbf{g}}_j\right) + \left(\tilde{\mathbf{R}}_i^T \cdot \tilde{\mathbf{g}}_j + \tilde{\mathbf{R}}_j^T \cdot \tilde{\mathbf{g}}_i - \tilde{\mathbf{R}}_i^T \cdot \tilde{\mathbf{g}}_i - \tilde{\mathbf{R}}_j^T \cdot \tilde{\mathbf{g}}_j\right) \tag{6.8}$$

There are several advantages to using Equation (6.8) for a TS search. The opti-

mization direction can be well maintained by choosing the correct sign of the eigenvalues ϵ at each step. In addition, the weight of each normal mode in the least-squares minimization scheme can be controlled. Inspired by the nature of the TS search, we propose the following equation as a guided optimization scheme that weighs the reaction path (the eigenvector with a negative eigenvalue) heavier than the rest of the coordinates within the least-squares framework:

$$\tilde{a}_{i,j} = \frac{1}{2} \sum_{\epsilon_\mu<0} S \cdot \Big(\tilde{g}_{\mu,i} \cdot \epsilon_\mu^{-1} \cdot \tilde{g}_{\mu,i} + \tilde{g}_{\mu,j} \cdot \epsilon_\mu^{-1} \cdot \tilde{g}_{\mu,j} + \tilde{R}_{\mu,i} \cdot \tilde{g}_{\mu,j} + \tilde{R}_{\mu,j} \cdot \tilde{g}_{\mu,i} - \tilde{R}_{\mu,i} \cdot \tilde{g}_{\mu,i} - \tilde{R}_{\mu,j} \cdot \tilde{g}_{\mu,j} \Big) + \sum_{\epsilon_\nu>0} \Big(\tilde{g}_{\nu,i} \cdot \epsilon_\nu^{-1} \cdot \tilde{g}_{\nu,i} + \tilde{g}_{\nu,j} \cdot \epsilon_\nu^{-1} \cdot \tilde{g}_{\nu,j} + \tilde{R}_{\nu,i} \cdot \tilde{g}_{\nu,j} + \tilde{R}_{\nu,j} \cdot \tilde{g}_{\nu,i} - \tilde{R}_{\nu,i} \cdot \tilde{g}_{\nu,i} - \tilde{R}_{\nu,j} \cdot \tilde{g}_{\nu,j} \Big) \tag{6.9}$$

In Equation (6.9), μ and ν index eigenvectors/eigenvalues of the Hessian and S is the weighting factor for the reaction path. The first sum collects errors associated with the reaction path with $\epsilon_\mu < 0$, whereas, the second sum evaluates the remaining vectors associated with a downhill minimization. When $S > 1$, the optimizer prioritizes locating the reaction path vector over minimizing the coordinates that are orthogonal to the reaction path. The following test cases will show that this method quickly locates the transition vector while minimizing the remaining coordinates.

6.3 Benchmark and Discussion

Optimizations were carried out on an SGI Atlix 450 workstation (Intel dual core-Itanium 1.6 GHz with 48 GB of RAM) using the development version of the GAUSSIAN program[131] with the addition of the guided En-DIIS algorithm presented here for TS optimization. For all methods tested here, the optimization is considered converged when the maximum component of the gradient vector is less than 4.5×10^{-4} a.u., the root mean square (RMS) gradient is less than 3×10^{-4} a.u., the maximum component of the displacement is less than 1.8×10^{-3} a.u., and the RMS

displacement is less than 1.2×10^{-3} a.u. The following optimization strategies are used in the benchmark tests: (1) the analytical Hessian is computed at the first step, and subsequent Hessians are updated using Bofill's weigted update of the Powell and Murtagh-Sargent method;[191] (2) if there is more than one negative eigenvalue associated with the initial geometry, the RFO approach is used until only one negative force constant remains; (3) when the RMS gradient is greater than 10^{-3} a.u., the weight factor S in Equation (6.9) is set to be equal to the total number of nuclear degrees of freedom; and (4) when the RMS gradient is less than 10^{-3} a.u., and the optimization step is considered to be in the quadratic region of the PES, standard RFO-DIIS,[168,169] without any weighting factor ($S = 1$), is used until convergence is reached. For all test cases considered below, the weighting factor S in Equation (6.9) was set equal to the number of nuclear degrees of freedom so as to weight the error along the reaction path equally with the combined weight of all the other coordinates. Alternate values of S were also considered, and revealed this to be the optimal choice for the weighting factor.

Table 6.1 lists TS optimization performance using the guided En-DIIS method. For all small molecule test cases, the method is able to successfully locate the TS. The final TS structures and imaginary frequencies are in excellent agreement with those obtained using the RFO approach. While the guided En-DIIS method exhibits consistently excellent performance on these well-studied test cases, the next two test cases are considered challenging for a TS search algorithm.

The TS (structure given in Figure 6.1) in the electrocyclic ring opening of [12]annulene (cyclododecahexane) is associated with a relatively flat reaction path (small absolute value of the negative force constant at the TS). Additionally, the PES of multiple coordinates that are perpendicular to the reaction path are also very flat (with two positive eigenvalues less than 10^{-2} a.u.). Such conditions can often *frustrate* a TS search algorithm. Figure 6.1 compares the TS optimization of [12]annulene using the algorithm introduced above to the traditional RFO method. In this TS search, the

Table 6.1. Comparison of the computational costs for Quasi-Newton RFO and guided En-DIIS transition state optimization methods on selected test molecules at the HF/3-21G level of theory.

		RFO		gEn-DIIS	
	E^a (au)	N^b	ν (cm^{-1})	N^b	ν (cm^{-1})
$CH_3CHO \rightarrow CH_2CHOH$	–151.913 10	8	–2513.0	7	–2513.0
$H_2CO \rightarrow H_2 + CO$	–113.050 03	6	–2213.0	6	–2213.3
$SiH_2 + H_2 \rightarrow SiH_4$[c]	–289.565 03	8	–1714.9	7	–1714.5
$H_3CO \rightarrow H_2COH$[c]	–113.621 92	12	–1721.9	15	–1720.9
$CH_3 + HF \rightarrow CH_4 + F$[c]	–138.779 63	5	–2897.5	5	–2897.6
$CH_3CH_2F \rightarrow CH_2CH_2 + HF$	–176.984 53	13	–2094.5	14	–2094.0
Diels-Alder reaction[c,d]	–231.603 21	6	–818.2	6	–818.2
Claisen rearrangement[c,e]	–267.238 59	18	–763.2	17	–763.3
Ene reaction[d,f]	–193.942 54	23	–1690.2	29	–1689.6

[a] Final energy. [b] Number of optimization steps. [c] Initial structures taken from Ref. 179.
[d] $CH_2CH_2 + CH_2CHCHCH_2 \rightarrow C_6H_{10}$ [e] $CH_2CHCH_2OCHCH_2 \rightarrow CH_2CHCH_2CH_2CHO$
[f] $CH_2CH_2 + CH_2CHCH_3 \rightarrow CH_2CHCH_2CH_2CH_3$

guided En-DIIS method exhibits multiple large oscillations, which seem uncharacteristic because DIIS is known to have smooth optimization behavior.[167,171] When the reaction path vector is weighed heavier in the minimization scheme, as in the guided En-DIIS approach, the optimal conditions are not satisfied for optimizing the remaining coordinates. As a result, the total energy and total RMS gradient can exhibit large oscillations due to non-optimal pathways for the majority of coordinates during the early stage of optimization. However, hidden in such seemingly unproductive oscillations is the algorithm minimizing errors associated with the most important transition state vector and climbing uphill along the reaction path coordinate. Figure 6.2 shows the total RMS force and the inset shows the value of the force of the

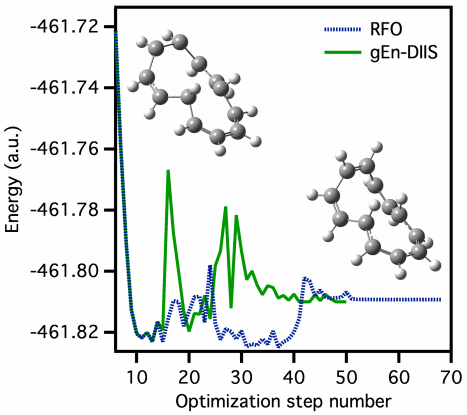

Figure 6.1. Comparison of transition state optimization methods for the electrocyclic ring opening of [12]annulene at the B3LYP/3-21G level of theory. The structure on the left corresponds to the initial structure used in the RFO and guided En-DIIS (gEn-DIIS) optimizations and the structure on the right corresponds to the optimized transition state structure obtained from the gEn-DIIS method.

TS vector at each optimization step. While the total RMS force seems unstable with large oscillations, the force of the TS vector is minimized towards the maximum using the guided En-DIIS method. Figure 6.1 also suggests that the RFO method takes on a different TS optimization pathway than that of the guided En-DIIS approach. As the guided En-DIIS does not choose to fully optimize the majority of coordinates during the early stage of the optimization process, the total energy never reaches as low as that of the RFO approach until the end due to the non-optimal minimization pathways for non-reaction-path coordinates. For TS optimization, this happens to be an ideal situation because optimizing the non-reaction-path coordinates when the TS vector is still undetermined or unstable is often unproductive. In this test case, the guided En-DIIS shows a speed-up of 30% compared to RFO.

While most TS search methods show success on small test cases, large molecules with many nuclear degrees of freedom are often of great difficulty. Figure 6.3 shows the TS structure of the proton diffusion pathway in a 1.2 nm CdSe nanocrystal.

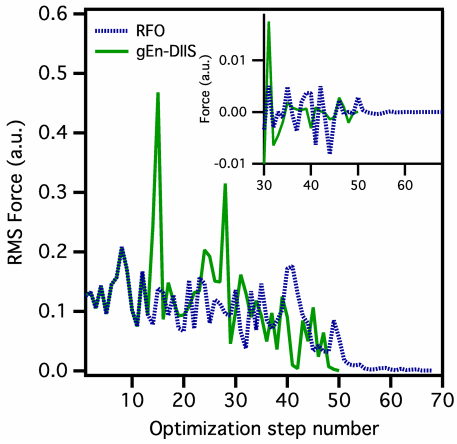

Figure 6.2. Root-mean-square (RMS) of the force for the transition state optimization of the elctrocyclic ring opening of [12]annulene at the B3LYP/3-21G level of theory. Inset: Value of the first element of the gradient corresponding to the force along the reaction pathway of this transition state optimization.

Due to strongly coupled reaction paths and an extremely flat PES (with six positive eigenvalues less than 10^{-3} a.u.) at the TS associated with the proton, RFO converged to a second-order saddle point after 70 optimization steps. On the other hand, the guided En-DIIS method converges to the TS structure after 66 optimization steps, again exhibiting fast and stable optimization for a difficult case.

6.4 Conclusion

In this work, we introduced a guided energy-represented DIIS method for molecular TS optimization. During the early stage of optimization, the errors arising from the TS vector are weighed heavier in the least-squares minimization scheme. This approach leads to quick stabilization of the transition vector before the full optimization of the non-reaction coordinates begins. Test cases show that this method exhibits fast optimization to locate the TS. In difficult cases where the reaction path is flat (a small absolute value of the force constant), this method is particularly advantageous

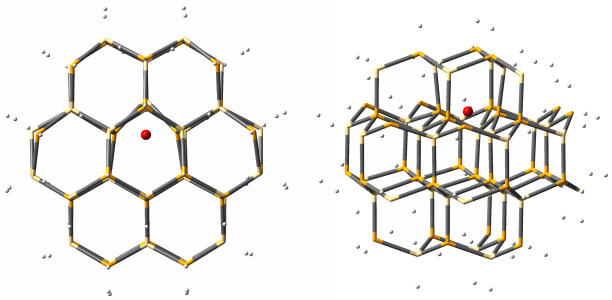

Figure 6.3. Transition state structure of a proton diffusion pathway in a 1.2 nm CdSe nanocrystal optimized using the guided En-DIIS method at the PBE1PBE/LANL2DZ level of theory. The position of the diffused hydrogen atom is given by the red dot.

because of its ability to stabilize the reaction coordinate in a multi-dimensional system. Lastly, it should be noted that the method presented here, in which a weighting factor is used to guide the optimization along a desired pathway, could be used in any optimization method that is carried out in the normal coordinate system, including the RFO approach.

BIBLIOGRAPHY

[1] Beaulac, R.; Schneider, L.; Archer, P. I.; Bacher, G.; Gamelin, D. R. Light-Induced Spontaneous Magnetization in Doped Colloidal Quantum Dots; *Science* **2009**, *325*, 973–976.

[2] Fernández-Rossier, J.; Aguado, R. Mn-doped II-VI quantum dots: artificial molecular magnets; *Phys. Status Solidi C* **2006**, *3*, 3734–3739.

[3] Loss, D.; DiVincenzo, D. P. Quantum computation with quantum dots; *Phys. Rev. A* **1998**, *57*, 120–126.

[4] Žutić, I.; Fabian, J.; Sarma, S. D. Spintronics: Fundamentals and applications; *Rev. Mod. Phys.* **2004**, *76*, 323–410.

[5] Osterloh, F. E. Inorganic Materials as Catalysts for Photochemical Splitting of Water; *Chem. Mater.* **2008**, *20*, 35–54.

[6] Liu, W. K.; Salley, G. M.; Gamelin, D. R. Spectroscopy of photovoltaic and photoconductive nanocrystalline Co^{2+}-doped ZnO electrodes; *J. Phys. Chem. B* **2005**, *109*, 14486–14495.

[7] Kittilstved, K. R.; Liu, W. K.; Gamelin, D. R. Electronic structure origins of polarity-dependent high-T_C ferromagnetismin oxide-diluted magnetic semiconductors; *Nat. Mater.* **2006**, *5*, 291–297.

[8] Nozik, A. J.; Beard, M. C.; Luther, J. M.; Law, M.; Ellingson, R. J.; Johnson, J. C. Semiconductor Quantum Dots and Quantum Dot Arrays and Applications of Multiple Exciton Generation to Third-Generation Photovoltaic Solar Cells; *Chem. Rev.* **2010**, *110*, 6873–6890.

[9] Mora-Seró, I.; Giménez, S.; Fabregat-Santiago, F.; Gómez, R.; Shen, Q.; Toyoda, T.; Bisquert, J. Recombination in Quantum Dot Sensitized Solar Cells; *Acc. Chem. Res.* **2009**, *42*, 1848–1857.

[10] Kramer, I. J.; Sargent, E. H. Colloidal Quantum Dot Photovoltaics: A Path Forward; *ACS Nano* **2011**, *5*, 8506–8514.

[11] Ip, A. H.; Thon, S. M.; Hoogland, S.; Voznyy, O.; Zhitomirsky, D.; Debnath, R.; Levina, L.; Rollny, L. R.; Carey, G. H.; Fischer, A.; Kemp, K. W.; Kramer, I. J.; Ning, Z.; Labelle, A. J.; Chou, K. W.; Amassian, A.; Sargent, E. H. Hybrid Passivated Colloidal Quantum Dot Solids; *Nat. Nanotechnol.* **2012**, *7*, 577–582.

[12] Kamat, P. V. Quantum Dot Solar Cells. The Next Big Thing in Photovoltaics; *J. Phys. Chem. Lett.* **2013**, *4*, 908–918.

[13] Zhu, H.; Song, N.; Lian, T. Charging of Quantum Dots by Sulfide Redox Electrolytes Reduces Electron Injection Efficiency in Quantum Dot Sensitized Solar Cells; *J. Am. Chem. Soc.* **2013**, *135*, 11461–11464.

[14] Beaulac, R.; Archer, P. I.; Ochsenbein, S. T.; Gamelin, D. R. Mn^{2+}-Doped CdSe Quantum Dots: New Inorganic Materials for Spin-Electronics and Spin-Photonics; *Adv. Func. Mater.* **2008**, *18*, 3873–3891.

[15] Hetsch, F.; Zhao, N.; Kershaw, S. V.; Rogach, A. L. Quantum dot field effect transistors; *Mater. Today* **2013**, *16*, 312–325.

[16] Hanson, R.; Kouwenhoven, L. P.; Petta, J. R.; Tarucha, S.; Vandersypen, L. M. K. Spins in few-electron quantum dots; *Rev. Mod. Phys.* **2007**, *79*, 1217–1265.

[17] Awschalom, D. D.; Bassett, L. C.; Dzurak, A. S.; Hu, E. L.; Petta, J. R. Quantum Spintronics: Engineering and Manipulating Atom-Like Spins in Semiconductors; *Science* **2013**, *339*, 1174–1179.

[18] Norris, D. J.; Efros, A. L.; Erwin, S. C. Doped Nanocrystals; *Science* **2008**, *319*, 1776–1779.

[19] Pradhan, N.; Goorskey, D.; Thessing, J.; Peng, X. An Alternative of CdSe Nanocrystal Emitters: Pure and Tunable Impurity Emissions in ZnSe Nanocrystals; *J. Am. Chem. Soc.* **2005**, *127*, 17586–17587.

[20] Beaulac, R.; Archer, P. I.; Gamelin, D. R. Luminescence in colloidal Mn^{2+}-doped semiconductor nanocrystals; *J. Solid State Chem.* **2008**, *181*, 1582–1589.

[21] Serpone, N.; Lawless, D.; Disdier, J.; marie Herrmann, J. Spectroscopic, Photoconductivity, and Photocatalytic Studies of $Ti0_2$ Colloids: Naked and with the Lattice Doped with Cr^{3+}, Fe^{3+}, and V^{5+} Cations; *Langmuir* **1994**, *10*, 643–652.

[22] Wolf, S. A.; Awschalom, D. D.; Buhrman, R. A.; Daughton, J. M.; von Molnár, S.; Roukes, M. L.; Chtchelkanova, A. Y.; Treger, D. M. Spintronics: A Spin-Based Electronics Vision for the Future; *Science* **2001**, *294*, 1488–1495.

[23] Kudo, A.; Sekizawa, M. Photocatalytic H_2 evolution under visible light irradiation on Ni-doped ZnS photocatalyst; *Chem. Commun.* **2000**, *15*, 1371–1372.

[24] Zou, Z.; Ye, J.; Sayama, K.; Arakawa, H. Direct Splitting of Water Under Visible Light Irradiation with an Oxide Semiconductor Photocatalyst; *Nature* **2001**, *414*, 625–627.

[25] Kato, H.; Kudo, A. Visible-Light-Response and Photocatalytic Activities of TiO_2 and $SrTiO_3$ Photocatalysts Codoped with Antimony and Chromium; *J. Phys. Chem. B* **2002**, *106*, 5029–5034.

[26] Whitaker, K. M.; Ochsenbein, S. T.; Polinger, V. Z.; Gamelin, D. R. Electron confinement effects in the EPR spectra of colloidal n-type ZnO quantum dots; *J. Phys. Chem. C* **2008**, *112*, 14331–14335.

[27] Ochsenbein, S. T.; Feng, Y.; Whitaker, K. M.; Badaeva, E.; Liu, W. K.; Li, X.; Gamelin, D. R. Charge-controlled magnetism in colloidal doped semiconductor nanocrystals; *Nat. Nano.* **2009**, *4*, 681–687.

[28] Hayoun, R.; Whitaker, K. M.; Gamelin, D. R.; Mayer, J. M. Electron Transfer Between Colloidal ZnO Nanocrystals; *J. Am. Chem. Soc.* **2011**, *133*, 4228–4231.

[29] Schrauben, J. N.; Hayoun, R.; Valdez, C. N.; Braten, M.; Fridley, L.; Mayer, J. M. Titanium and Zinc Oxide Nanoparticles Are Proton-Coupled Electron Transfer Agents; *Science* **2012**, *336*, 1298–1301.

[30] Norberg, N. S.; Kittilstved, K. R.; Amonette, J. E.; Kukkadapu, R. K.; Schwartz, D. A.; Gamelin, D. R. Synthesis of colloidal Mn^{2+}: ZnO quantum dots and high-T_C ferromagnetic nanocrystalline thin films; *J. Am. Chem. Soc.* **2004**, *126*, 9387–9398.

[31] Johnson, C. A.; Kittilstved, K. R.; Kaspar, T. C.; Droubay, T. C.; Chambers, S. A.; Salley, G. M.; Gamelin, D. R. Mid-gap electronic states in $Zn_{1-x}Mn_xO$; *Phys. Rev. B* **2010**, *82*, 115202.

[32] Gilliland, S. G.; Sans, J. A.; Sanchez-Royo, J. F.; Almonacid, G.; Segura, A. Charge-transfer absorption band in $Zn_{1-x}M_xO$ (M: Co, Mn) investigated by means of photoconductivity, Ga doping, and optical measurements under pressure; *Appl. Phys. Lett.* **2010**, *96*, 241902.

[33] Godlewski, M.; Wojcik-Glodowska, A.; Guziewicz, E.; Yatsunenko, S.; Zakrzewski, A.; Dumont, Y.; Chikoidze, E.; Phillips, M. R. Optical properties of manganese doped wide band gap ZnS and ZnO; *Opt. Mater.* **2009**, *31*, 1768–1771.

[34] Phan, T.-L.; Yu, S. C.; Vincent, R.; Bui, H. M.; Thanh, T. D.; Lam, V. D.; Lee, Y. P. Influence of Mn doping on structural, optical, and magnetic properties of $Zn_{1x}Mn_xO$ nanorods; *J. Appl. Phys.* **2010**, *108*, 044910–044917.

[35] Badaeva, E.; Isborn, C. M.; Feng, Y.; Ochsenbein, S. T.; Gamelin, D. R.; Li, X. Theoretical Characterization of Electronic Transitions in Co^{2+}- and Mn^{2+}-Doped ZnO Nanocrystals; *J. Phys. Chem. C* **2009**, *113*, 8710–8717.

[36] Feng, Y.; Badaeva, E.; Gamelin, D. R.; Li, X. Excited-State Double Exchange in Manganese-Doped ZnO Quantum Dots: A Time-Dependent Density-Functional Study; *J. Phys. Chem. Lett.* **2010**, *1*, 1927–1931.

[37] Norberg, N. S.; Dalpian, G. M.; Chelikowsky, J. R.; Gamelin, D. R. Energetic pinning of magnetic impurity levels in quantum-confined semiconductors; *Nano Lett.* **2006**, *6*, 2887–2892.

[38] Badaeva, E.; May, J. W.; Ma, J.; Gamelin, D. R.; Li, X. Characterization of Excited-State Magnetic Exchange in Mn^{2+}-Doped ZnO Quantum Dots Using Time-Dependent Density Functional Theory; *J. Phys. Chem. C* **2011**, *115*, 20986–20991.

[39] Kasap, S., Capper, P., Eds. *Springer Handbook of Electronic and Photonic Materials;* Springer, 2006.

[40] Brus, L. E. A Simple Model for the Ionization Potential, Electron Affinity, and Aqueous Redox Potentials of Small Semiconductor Crystallites; *J. Chem. Phys.* **1983**, *79*, 5566–5571.

[41] Brus, L. E. Electron Electron and Electron-Hole Interactions in Small Semiconductor Crystallites - the Size Dependence of the Lowest Excited Electronic State; *J. Chem. Phys.* **1984**, *80*, 4403–4409.

[42] Brus, L. Electronic Wave Functions in Semiconductor Clusters: Experiment and Theory; *J. Phys. Chem.* **1986**, *90*, 2555–2560.

[43] Anderson, P. W. In *Magnetism*; Rado, G. T., Suhl, H., Eds., Vol. 1; Academic Press: New York, NY, 1963; p 25.

[44] Anderson, P. W. Theory of Magnetic Exchange Interactions:Exchange in Insulators and Semiconductors; *Solid State Phys.* **1963**, *14*, 99–214.

[45] Anderson, P. W.; Hasegawa, H. Considerations on Double Exchange; *Phys. Rev.* **1955**, *100*, 675–681.

[46] Furdyna, J. K. Diluted magnetic semiconductors; *J. Appl. Phys.* **1988**, *64*, R29–R64.

[47] Furdyna, J. K.; Kossut, J. *Diluted Magnetic Semiconductors;* Academic Press: New York, 1988.

[48] Beaulac, R.; Gamelin, D. R. Two-center formulation of Mn^{2+}-electron *s–d* exchange coupling in bulk and quantum-confined diluted magnetic semiconductors; *Phys. Rev. B* **2010**, *82*, 224401.

[49] Beaulac, R.; Feng, Y.; May, J. W.; Badaeva, E.; Gamelin, D. R.; Li, X. Orbital pathways for Mn^{2+}-carrier *sp–d* exchange in diluted magnetic semiconductor quantum dots; *Phys. Rev. B* **2011**, *84*, 195324.

[50] Goodenough, J. B. *Magnetism and the Chemical Bond;* John Wiley & Sons: New York, NY, 1963.

[51] Weihe, H.; Güdel, H. U. Quantitative Interpretation of the Goodenough-Kanamori Rules: A Critical Analysis; *Inorg. Chem.* **1997**, *36*, 3632–3639.

[52] Mabbs, F. E.; Machin, D. J. *Magnetism and Transition Metal Complexes;* Dover Publications, Inc.: Mineola, NY, 1973.

[53] Kolesnik, S.; Dabrowski, B.; Wiren, Z. Q.; Kepa, H.; Giebultowicz, T. M.; Brown, C. M.; Lëao, J.; Furdyna, J. K. Determination of antiferromagnetic interactions in Zn(Mn)O, Zn(Co)O, and Zn(Mn)Te by inelastic neutron scattering; *J. Appl. Phys.* **2006**, *99*, 08M122.

[54] Zener, C. Interaction between the d-Shells in the Transition Metals. II. Ferromagnetic Compounds of Manganese with Perovskite Structure; *Phys. Rev.* **1951**, *82*, 403–405.

[55] Fischer, S. A.; May, J. W.; Lingerfelt, D. B.; Li, X. Non-adiabatic Molecular Dynamics Investigation of Charge Transfer State Formation in Mn^{2+}-Doped ZnO Quantum Dots (unpublished), **2014**.

[56] Chambers, S. A. Ferromagnetism in doped thin-film oxide and nitride semiconductors and dielectrics; *Surf. Sci. Rep.* **2006**, *61*, 345–381.

[57] Chambers, S. A.; Droubay, T. C.; Wang, C. M.; Rosso, K. M.; Heald, S. M.; Schwartz, D. A.; Kittilstved, K. R.; Gamelin, D. R. Ferromagnetism in oxide semiconductors; *Mater. Today* **2006**, *9*, 28–35.

[58] Coey, J. M. Dilute magnetic oxides; *Curr. Opin. Solid St. M.* **2006**, *10*, 83–92.

[59] Dietl, T. Origin of ferromagnetic response in diluted magnetic semiconductors and oxides; *J. Phys.–Condens. Mat.* **2007**, *19*, 165204.

[60] Kossut, J.; Gaj, J. A. *Intorduction to the Physics of Diluted Magnetic Semiconductors;* Springer-Verlag: Berlin, 2010.

[61] Jonker, B. T.; Park, Y. D.; Bennett, B. R.; Cheong, H. D.; Kioseoglou, G.; Petrou, A. Robust electrical spin injection into a semiconductor heterostructure; *Phys. Rev. B* **2000**, *62*, 8180–8183.

[62] Ohno, Y.; Young, D. K.; Beschoten, B.; Matsukura, F.; Ohno, H.; Awschalom, D. D. Electrical spin injection in a ferromagnetic semiconductor heterostructure; *Nature* **1999**, *402*, 790–792.

[63] Harris, J. H.; Nurmikko, A. V. Formation of the Bound Magnetic Polaron in (Cd,Mn)Se; *Phys. Rev. Lett.* **1983**, *51*, 1472–1475.

[64] Seufert, J.; Bacher, G.; Scheibner, M.; Forchel, A.; Lee, S.; Dobrowolska, M.; Furdyna, J. K. Dynamical Spin Response in Semimagnetic Quantum Dots; *Phys. Rev. Lett.* **2002**, *88*, 027402.

[65] Kittilstved, K. R.; Norberg, N. S.; Gamelin, D. R. Chemical manipulation of High-T_C ferromagnetism in ZnO diluted magnetic semiconductors; *Phys. Rev. Lett.* **2005**, *94*, 147209.

[66] Spaldin, N. A. Search for ferromagnetism in transition-metal-doped piezoelectric ZnO; *Phys. Rev. B* **2004**, *69*, 125201.

[67] Sharma, P.; Gupta, A.; Rao, K. V.; Owens, F. J.; Sharma, R.; Ahuja, R.; Guillen, J. M. O.; Johansson, B.; Gehring, G. A. Ferromagnetism above room temperature in bulk and transparent thin films of Mn-doped ZnO; *Nat. Mater.* **2003**, *2*, 673–677.

[68] Sato, K.; Katayama-Yoshida, H. Ferromagnetism in a transition metal atom doped ZnO; *Physica E* **2001**, *10*, 251–255.

[69] Maouche, D.; Ruterana, P.; Louail, L. Carrier-mediated ferromagnetism in N co-doped (Zn,Mn)O-based diluted magnetic semiconductors; *Phys. Lett. A* **2007**, *365*, 231–234.

[70] Wang, Q.; Sun, Q.; Jena, P.; Kawazoe, Y. Carrier-mediated ferromagnetism in N codoped (Zn,Mn)O $(10\bar{1}0)$ thin films; *Phys. Rev. B* **2004**, *70*, 052408.

[71] Petit, L.; Schulthess, T. C.; Svane, A.; Szotek, Z.; Temmerman, W. M.; Janotti, A. Electronic structure of transition-metal impurities in p-type ZnO; *Phys. Rev. B* **2006**, *73*, 045107.

[72] Petit, L.; Schulthess, T. C.; Svane, A.; Temmerman, W. M.; Szotek, Z.; Janotti, A. Valency Configuration of Transition Metal Impurities in ZnO; *J. Electron. Mater.* **2006**, *35*, 556–561.

[73] Bawendi, M. G.; Steigerwald, M. L.; Brus, L. E. The Quantum Mechanics of Larger Semiconductor Clusters ("Quantum Dots"); *Annu. Rev. Phys. Chem.* **1990**, *41*, 477–496.

[74] Mizokawa, T.; Nambu, T.; Fujimori, A.; Fukumura, T.; Kawasaki, M. Electronic structure of the oxide-diluted magnetic semiconductor $Zn_{1-x}Mn_xO$; *Phys. Rev. B* **2002**, *65*, 085209.

[75] Chanier, T.; Virot, F.; Hayn, R. Chemical trend of exchange coupling in diluted magnetic II-VI semiconductors: Ab initio calculations; *Phys. Rev. B* **2009**, *79*, 205204.

[76] Hass, K. C.; Larson, B. E.; Ehrenreich, H.; Carlsson, A. E. Magnetic interactions in diluted magnetic semiconductors; *J. Magn. Magn. Mater.* **1986**, *54-57*, 1283–1284.

[77] Heiman, D.; Shapira, Y.; Foner, S. Exchange energy for conduction electrons in (ZnMn)Se derived from spin-flip Raman scattering and magnetization; *Solid State Commun.* **1984**, *51*, 603–606.

[78] Sellers, I. R.; Oszwaldowski, R.; Whiteside, V. R.; Eginligil, M.; Petrou, A.; Žutić, I.; Chou, W.-C.; Fan, W. C.; Petukhov, A. G.; Kim, S. J.; Cartwright, A. N.; McCombe, B. D. Robust magnetic polarons in type-II (Zn,Mn)Te/ZnSe magnetic quantum dots; *Phys. Rev. B* **2010**, *82*, 195320.

[79] Abolfath, R. M.; Petukhov, A. G.; Žutić, I. Piezomagnetic Quantum Dots; *Phys. Rev. Lett.* **2008**, *101*, 207202.

[80] Oszwaldowski, R.; Žutić, I.; Petukhov, A. G. Magnetism in Closed-Shell Quantum Dots: Emergence of Magnetic Bipolarons; *Phys. Rev. Lett.* **2011**, *106*, 177201.

[81] Kisi, E. H.; Elcombe, M. M. u parameters for the wurtzite structure of ZnS and ZnO using powder neutron diffraction; *Acta Crystallogr. C* **1989**, *45*, 1867–1870.

[82] Xu, Y.-N.; Ching, W. Y. Electronic, optical, and structural properties of some wurtzite crystals; *Phys. Rev. B* **1993**, *48*, 4335–4351.

[83] Bacher, G. Optical Spectroscopy on Epitaxially Grown II-VI Single Quantum Dots; *Top. Appl. Phys.* **2003**, *90*, 147–184.

[84] Schwartz, D. A.; Norberg, N. S.; Nguyen, Q. P.; Parker, J. M.; Gamelin, D. R. Magnetic quantum dots: Synthesis, spectroscopy, and magnetism of Co^{2+}- and Ni^{2+}-doped ZnO nanocrystals; *J. Am. Chem. Soc.* **2003**, *125*, 13205–13218.

[85] Norris, D. J.; Yao, N.; Charnock, F. T.; Kennedy, T. High-Quality Manganese-Doped ZnSe Nanocrystals; *Nano Lett.* **2001**, *1*, 3–7.

[86] Archer, P. I.; Santangelo, S. A.; Gamelin, D. R. Direct observation of *sp–d* exchange interactions in colloidal Mn^{2+}- and Co^{2+}-doped CdSe quantum dots; *Nano Lett.* **2007**, *7*, 1037–1043.

[87] Haranath, D.; Sahai, S.; Joshi, A. G.; Gupta, B. K.; Shanker, V. Investigation of confinement effects in ZnO quantum dots; *Nanotechnology* **2009**, *20*, 425701.

[88] Senger, R. T.; Bajaj, K. K. Optical properties of confined polaronic excitons in spherical ionic quantum dots; *Phys. Rev. B* **2003**, *68*, 045313.

[89] Wood, A.; Giersig, M.; Hilgendorff, M.; Vilas-Campos, A.; Lis-Marzan, L. M.; Mulvaney, P. Size effects in ZnO: The cluster to quantum dot transition; *Aust. J. Chem.* **2003**, *56*, 1051–1057.

[90] Badaeva, E.; Feng, Y.; Gamelin, D. R.; Li, X. Investigation of pure and Co^{2+}-doped ZnO quantum dot electronic structures using the density functional theory: choosing the right functional; *New J. Phys.* **2008**, *10*, 055013.

[91] Huang, X. Y.; Lindgren, E.; Chelikowsky, J. R. Surface passivation method for semiconductor nanostructures; *Phys. Rev. B* **2005**, *71*, 165328.

[92] Wang, L.-W.; Li, J. First-principles thousand-atom quantum dot calculations; *Phys. Rev. B* **2004**, *69*, 153302.

[93] Gaussian Development Version Revision H.01. Frisch, M. J.; Trucks, G. W.; Schlegel, H. B.; Scuseria, G. E.; Robb, M. A.; Cheeseman, J. R.; Scalmani, G.; Barone, V.; Mennucci, B.; Petersson, G. A.; Nakatsuji, H.; Caricato, M.; Li, X.; Hratchian, H. P.; Izmaylov, A. F.; Bloino, J.; Zheng, G.; Sonnenberg, J. L.; Hada, M.; Ehara, M.; Toyota, K.; Fukuda, R.; Hasegawa, J.; Ishida, M.; Nakajima, T.; Honda, Y.; Kitao, O.; Nakai, H.; Vreven, T.; J. A. Montgomery, J.; Peralta, J. E.; Ogliaro, F.; Bearpark, M.; Heyd, J. J.; Brothers, E.; Kudin, K. N.; Staroverov, V. N.; Kobayashi, R.; Normand, J.; Raghavachari, K.; Rendell, A.; Burant, J. C.; Iyengar, S. S.; Tomasi, J.; Cossi, M.; Rega, N.; Millam, J. M.; Klene, M.; Knox, J. E.; Cross, J. B.; Bakken, V.; Adamo, C.; Jaramillo, J.; Gomperts, R.; Stratmann, R. E.; Yazyev, O.; Austin, A. J.; Cammi, R.; Pomelli, C.; Ochterski, J. W.; Martin, R. L.; Morokuma, K.; Zakrzewski, V. G.; Voth, G. A.; Salvador, P.; Dannenberg, J. J.; Dapprich, S.; Parandekar, P. V.; Mayhall, N. J.; Daniels, A. D.; Farkas, O.; Foresman, J. B.; Ortiz, J. V.; Cioslowski, J.; Fox, D. J.

[94] Adamo, C.; Barone, V. Toward reliable density functional methods without adjustable parameters: The PBE0 model; *J. Chem. Phys.* **1999**, *110*, 6158–6170.

[95] Perdew, J. P.; Burke, K.; Ernzerhof, M. Generalized Gradient Approximation Made Simple; *Phys. Rev. Lett.* **1996**, *77*, 3865–3868.

[96] Perdew, J. P.; Burke, K.; Ernzerhof, M. Generalized Gradient Approximation Made Simple [Phys. Rev. Lett. 77, 3865 (1996)]; *Phys. Rev. Lett.* **1997**, *78*, 1396–1396.

[97] Hay, P. J.; Wadt, W. R. Ab initio effective core potentials for molecular calculations. Potentials for the transition metal atoms Sc to Hg; *J. Chem. Phys.* **1985**, *82*, 270–283.

[98] Hay, P. J.; Wadt, W. R. Ab initio effective core potentials for molecular calculations. Potentials for K to Au including the outermost core orbitals; *J. Chem. Phys.* **1985**, *82*, 299–310.

[99] Wadt, W. R.; Hay, P. J. Ab initio effective core potentials for molecular calculations. Potentials for main group elements Na to Bi; *J. Chem. Phys.* **1985**, *82*, 284–298.

[100] May, J. W.; McMorris, R. J.; Li, X. Ferromagnetism in *p*-Type Manganese-Doped Zinc Oxide Quantum Dots; *J. Phys. Chem. Lett.* **2012**, *3*, 1374–1380.

[101] Haase, M.; Weller, H.; Henglein, A. Photochemistry and Radiation Chemistry of Colloidal Semiconductors. 23. Electron Storage on ZnO Particles and Size Quantization; *J. Am. Chem. Soc.* **1988**, *92*, 482–487.

[102] Shim, M.; Guyot-Sionnest, P. n-type colloidal semiconductor nanocrystals; *Nature* **2000**, *407*, 981–983.

[103] Wang, C.; Shim, M.; Guyot-Sionnest, P. Electrochromic Nanocrystal Quantum Dots; *Science* **2001**, *291*, 2390–2392.

[104] Roest, A. L.; Kelly, J. J.; Vanmaekelbergh, D.; Meulenkamp, E. A. Staircase in the Electron Mobility of a ZnO Quantum Dot Assembly due to Shell Filling; *Phys. Rev. Lett.* **2002**, *89*, 036801.

[105] Yu, D.; Wang, C.; Guyot-Sionnest, P. n-Type Conducting CdSe Nanocrystal Solids; *Science* **2003**, *300*, 1277–1280.

[106] Guyot-Sionnest, P. Charging colloidal quantum dots by electrochemistry (review); *Microchim. Acta* **2008**, *160*, 309–314.

[107] Liu, W. K.; Whitaker, K. M.; Kittilstved, K. R.; Gamelin, D. R. Stable photogenerated carriers in magnetic semiconductor nanocrystals; *J. Am. Chem. Soc.* **2006**, *128*, 3910–3911.

[108] Valdez, C. N.; Braten, M.; Soria, A.; Gamelin, D. R.; Mayer, J. M. Effect of Protons on the Redox Chemistry of Colloidal Zinc Oxide Nanocrystals; *J. Am. Chem. Soc.* **2013**, *135*, 8492–8495.

[109] Cohn, A. W.; Kittilstved, K. R.; Gamelin, D. R. Tuning the Potentials of "Extra" Electrons in Colloidal *n*-Type ZnO Nanocrystals via Mg^{2+} Substitution; *J. Am. Chem. Soc.* **2012**, *134*, 7937–7943.

[110] Cohn, A. W.; Janssen, N.; Mayer, J. M.; Gamelin, D. R. Photocharging ZnO Nanocrystals: Picosecond Hole Capture, Electron Accumulation, and Auger Recombination; *J. Phys. Chem. C* **2012**, *116*, 20633–20642.

[111] Wehrenberg, B. L.; Guyot-Sionnest, P. Electron and Hole Injection in PbSe Quantum Dot Films; *J. Am. Chem. Soc.* **2003**, *125*, 7806–7807.

[112] Léger, Y.; Besombes, L.; Fernández-Rossier, J.; Maingault, L.; Mariette, H. Electrical Control of a Single Mn Atom in a Quantum Dot; *Phys. Rev. Lett.* **2006**, *97*, 107401.

[113] White, M. A.; Weaver, A. L.; Beaulac, R.; Gamelin, D. R. Electrochemically Controlled Auger Quenching of Mn^{2+} Photoluminescence in Doped Semiconductor Nanocrystals; *ACS Nano* **2011**, *5*, 4158–4168.

[114] Peng, B.; Liang, W.; White, M. A.; Gamelin, D. R.; Li, X. Theoretical Evaluation of Spin-Dependent Auger De-Excitation in Mn^{2+}-Doped Semiconductor Nanocrystals; *J. Phys. Chem. C* **2012**, *116*, 11223–11231.

[115] Gaussian Development Version Revision H.12+. Frisch, M. J.; Trucks, G. W.; Schlegel, H. B.; Scuseria, G. E.; Robb, M. A.; Cheeseman, J. R.; Scalmani, G.; Barone, V.; Mennucci, B.; Petersson, G. A.; Nakatsuji, H.; Caricato, M.; Li, X.; Hratchian, H. P.; Izmaylov, A. F.; Bloino, J.; Zheng, G.; Sonnenberg, J. L.; Liang, W.; Hada, M.; Ehara, M.; Toyota, K.; Fukuda, R.; Hasegawa, J.; Ishida, M.; Nakajima, T.; Honda, Y.; Kitao, O.; Nakai, H.; Vreven, T.; J. A. Montgomery, J.; Peralta, J. E.; Ogliaro, F.; Bearpark, M.; Heyd, J. J.; Brothers, E.; Kudin, K. N.; Staroverov, V. N.; Keith, T.; Kobayashi, R.; Normand, J.; Raghavachari, K.; Rendell, A.; Burant, J. C.; Iyengar, S. S.; Tomasi, J.; Cossi, M.; Rega, N.; Millam, J. M.; Klene, M.; Knox, J. E.; Cross, J. B.; Bakken, V.; Adamo, C.; Jaramillo, J.; Gomperts, R.; Stratmann, R. E.; Yazyev, O.; Austin, A. J.; Cammi, R.; Pomelli, C.; Ochterski, J. W.; Martin, R. L.; Morokuma, K.; Zakrzewski, V. G.; Voth, G. A.; Salvador, P.; Dannenberg, J. J.; Dapprich, S.; Parandekar, P. V.; Mayhall, N. J.; Daniels, A. D.; Farkas, O.; Foresman, J. B.; Ortiz, J. V.; Cioslowski, J.; Fox, D. J.

[116] Zeng, R.; Rutherford, M.; Xie, R.; Zou, B.; Peng, X. Synthesis of Highly Emissive Mn-Doped ZnSe Nanocrystals without Pyrophoric Reagents; *Chem. Mater.* **2010**, *22*, 2107–2113.

[117] Beaulac, R.; Ochsenbein, S. T.; Gamelin, D. R. In *Semiconductor Quantum Dots*; Klimov, V. I., Ed.; CRC Press, 2 ed., 2010; chapter 11, pp 397–453.

[118] Oszwałdowski, R.; Žutić, I.; Petukhov, A. G. Magnetism in Closed-Shell Quantum Dots: Emergence of Magnetic Bipolarons; *Phys. Rev. Lett.* **2011**, *106*, 177201.

[119] Oszwałdowski, R.; Stano, P.; Petukhov, A. G.; Žutić, I. Spin Ordering in Magnetic Quantum Dots: From Core-halo to Wigner Molecules; *Phys. Rev. B* **2012**, *86*, 201408.

[120] Austing, D. G.; Sasaki, S.; Tarucha, S.; Reimann, S. M.; M., K.; Manninen, M. Ellipsoidal Deformation of Vertical Quantum Dots; *Phys. Rev. B* **1999**, *60*, 11514.

[121] Osterloh, F. E. Inorganic materials as catalysts for photochemical splitting of water; *Chem. Mater.* **2007**, *20*, 35–54.

[122] Minami, T. Transparent conducting oxide semiconductors for transparent electrodes; *Semicond. Sci. Techno.* **2005**, *20*, S35.

[123] Shim, M.; Guyot-Sionnest, P. Organic-capped ZnO nanocrystals: synthesis and n-type character; *J. Am. Chem. Soc.* **2001**, *123*, 11651–11654.

[124] Wood, A.; Giersig, M.; Mulvaney, P. Fermi level equilibration in quantum dot-metal nanojunctions; *J. Phys. Chem. B* **2001**, *105*, 8810–8815.

[125] Buonsanti, R.; Llordes, A.; Aloni, S.; Helms, B. A.; Milliron, D. J. Tunable infrared absorption and visible transparency of colloidal aluminum-doped zinc oxide nanocrystals; *Nano letters* **2011**, *11*, 4706–4710.

[126] Schimpf, A. M.; Ochsenbein, S. T.; Buonsanti, R.; Milliron, D. J.; Gamelin, D. R. Comparison of extra electrons in colloidal n-type Al^{3+}-doped and photochemically reduced ZnO nanocrystals; *Chem. Commun.* **2012**, *48*, 9352–9354.

[127] van Dijken, A.; Meulenkamp, E. A.; Vanmaekelbergh, D.; Meijerink, A. Influence of adsorbed oxygen on the emission properties of nanocrystalline ZnO particles; *J. Phys. Chem. B* **2000**, *104*, 4355–4360.

[128] Liu, W. K.; Whitaker, K. M.; Smith, A. L.; Kittilstved, K. R.; Robinson, B. H.; Gamelin, D. R. Room-temperature electron spin dynamics in free-standing ZnO quantum dots; *Phys. Rev. Lett.* **2007**, *98*, 186804.

[129] Vanmaekelbergh, D.; Liljeroth, P. Electron-conducting quantum dot solids: novel materials based on colloidal semiconductor nanocrystals; *Chem. Soc. Rev.* **2005**, *34*, 299–312.

[130] Roest, A. L.; Germeau, A.; Kelly, J. J.; Vanmaekelbergh, D.; Allan, G.; Meulenkamp, E. A. Long-Range Transport in an Assembly of ZnO Quantum Dots: The Effects of Quantum Confinement, Coulomb Repulsion and Structural Disorder; *ChemPhysChem* **2003**, *4*, 959–966.

[131] Gaussian Development Version Revision H.21. Frisch, M. J.; Trucks, G. W.; Schlegel, H. B.; Scuseria, G. E.; Robb, M. A.; Cheeseman, J. R.; Scalmani, G.; Barone, V.; Mennucci, B.; Petersson, G. A.; Nakatsuji, H.; Caricato, M.; Li, X.; Hratchian, H. P.; Izmaylov, A. F.; Bloino, J.; Zheng, G.; Sonnenberg, J. L.; Liang, W.; Hada, M.; Ehara, M.; Toyota, K.; Fukuda, R.; Hasegawa, J.; Ishida, M.; Nakajima, T.; Honda, Y.; Kitao, O.; Nakai, H.; Vreven, T.; J. A. Montgomery, J.; Peralta, J. E.; Ogliaro, F.; Bearpark, M.; Heyd, J. J.; Brothers, E.; Kudin, K. N.; Staroverov, V. N.; Keith, T.; Kobayashi, R.; Normand, J.; Raghavachari, K.; Rendell, A.; Burant, J. C.; Iyengar, S. S.; Tomasi, J.; Cossi, M.; Rega, N.; Millam, J. M.; Klene, M.; Knox, J. E.; Cross, J. B.; Bakken, V.; Adamo, C.; Jaramillo, J.; Gomperts, R.; Stratmann, R. E.; Yazyev, O.; Austin, A. J.; Cammi, R.; Pomelli, C.; Ochterski, J. W.; Martin, R. L.; Morokuma, K.; Zakrzewski, V. G.; Voth, G. A.; Salvador, P.; Dannenberg, J. J.; Dapprich, S.; Parandekar, P. V.; Mayhall, N. J.; Daniels, A. D.; Farkas, O.; Foresman, J. B.; Ortiz, J. V.; Cioslowski, J.; Fox, D. J.

[132] Dreuw, A.; Head-Gordon, M. Single-reference ab initio methods for the calculation of excited states of large molecules; *Chem. Rev.* **2005**, *105*, 4009–4037.

[133] Song, C.; Geng, K. W.; Zeng, F.; Wang, X. B.; Shen, Y. X.; Pan, F.; Xie, Y. N.; Liu, T.; Zhou, H. T.; Fan, Z. Giant Magnetic Moment in an Anomalous Ferromagnetic Insulator: Co-Doped ZnO; *Phys. Rev. B* **2006**, *73*, 024405.

[134] Yao, T.; Yan, W.; Sun, Z.; Pan, Z.; Xie, Y.; Jiang, Y.; Ye, J.; Hu, F.; Wei, S. Magnetic Property and Spatial Occupation of Co Dopants in $Zn_{0.98}Co_{0.02}O$ Nanowires; *J. Phys. Chem. C* **2009**, *113*, 14114–14118.

[135] Xu, M.; Zhao, H.; Ostrikov, K.; Duan, M. Y.; Xu, L. X. Effect of Doping with Co and/or Cu on Electronic Structure and Optical Properties of ZnO; *J. Appl. Phys.* **2009**, *105*, 043708.

[136] Azam, A. Fabrication of Co-Doped ZnO Nanorods for Spintronic Devices; *Met. Mater. Int.* **2013**, *19*, 845–850.

[137] Kanai, Y. Optical Absorption and Conduction Due to Co^{2+} in ZnO Crystals; *J. Phys. Soc. Japan* **1968**, *24*, 956.

[138] Lommens, P.; Smet, P. F.; de Mello Donegá, C.; Meijerink, A.; Piraux, L.; Michotte, S.; Mátéfi-Tempfli, S.; Poelman, D.; Hens, Z. Photoluminescence Properties of Co^{2+}-doped ZnO Nanocrystals; *J. Lumin.* **2006**, *118*, 245–250.

[139] Schultz, H.-J.; Thiede, M. Optical Spectroscopy of $3d^7$ and $3d^8$ Impurity Configurations in a Wide-Gap Semiconductor (ZnO:Co, Ni, Cu); *Phys. Rev. B* **1987**, *35*, 18–34.

[140] Johnson, C. A.; Kaspar, T. C.; Chambers, S. A.; Salley, G. M.; Gamelin, D. R. Sub-band-gap photoconductivity in Co^{2+}-doped ZnO; *Phys. Rev. B* **2010**, *81*, 125206.

[141] Johnson, C. A.; Cohn, A.; Kaspar, T.; Chambers, S. A.; Salley, G. M.; Gamelin, D. R. Visible-light photoconductivity of $Zn_{1-x}Co_xO$ and its dependence on Co^{2+} concentration; *Phys. Rev. B* **2011**, *84*, 125203.

[142] Koidl, P. Optical Absorption of Co^{2+} in ZnO; *Phys. Rev. B* **1977**, *15*, 2493–2499.

[143] Walsh, A.; Da Silva, J. L. F.; Wei, S. H. Theoretical Description of Carrier Mediated Magnetism in Cobalt Doped ZnO; *Phys. Rev. Lett.* **2008**, *100*, 256401.

[144] Lany, S.; Raebiger, H.; Zunger, A. Magnetic Interactions of Cr-Cr and Co-Co Impurity Pairs in ZnO within a Band-Gap Corrected Density Functional Approach; *Phys. Rev. B* **2008**, *77*, 241201(R).

[145] Sarsari, I. A.; Pemmaraju, C. D.; Salamati, H.; Sanvito, S. ManyBody Quasiparticle Spectrum of Co-Doped ZnO: A GW Perspective; *Phys. Rev. B* **2013**, *87*, 245118.

[146] Gopal, P.; Spaldin, N. A. Magnetic Interactions in Transition-metal-doped ZnO: An Ab Initio Study; *Phys. Rev. B* **2006**, *74*, 094418.

[147] Dunning, T. H.; Hay, P. J. Modern Theoretical Chemistry; Plenum: New York, 1977; Vol. 2; pp 1–28.

[148] Roy, L. E.; Hay, P. J.; Martin, R. L. Revised Basis Sets for the LANL Effective Core Potentials; *J. Chem. Theor. Comput.* **2008**, *4*, 1029–1031.

[149] Kobayashi, M.; Ishida, Y.; Hwang, J. I.; Mizokawa, T.; Fujimori, A.; Mamiya, K.; Okamoto, J.; Takeda, Y.; Okane, T.; Saitoh, Y.; Muramatsu, Y.; Tanaka, A.; Saeki, H.; Tabata, H.; Kawai, T. Characterization of Magnetic Components

in the Diluted Magnetic Semiconductor $Zn_{1-x}Co_xO$ by X-Ray Magnetic Circular Dichroism; *Phys. Rev. B* **2005**, *72*, 201201(R).

[150] Wi, S. C.; Kang, J. S.; Kim, J. H.; Cho, S. B.; Kim, B. J.; Yoon, S.; Suh, B. J.; Han, S. W.; Kim, K. H.; Kim, K. J.; Kim, B. S.; Song, H. J.; Shin, H. J.; Shim, J. H.; Min, B. I. Electronic Structure of $Zn_{1-x}Co_xO$ Using Photoemission and X-Ray Absorption Spectroscopy; *Appl. Phys. Lett.* **2004**, *84*, 4233–4235.

[151] Kaspar, T. C.; Droubay, T.; Heald, S. M.; Nachimuthu, P.; Wang, C. M.; Shutthanandan, V.; Johnson, C. A.; Gamelin, D. R.; Chambers, S. A. Lack of ferromagnetism in *n*-type cobalt-doped ZnO epitaxial thin films; *New J. Phys.* **2008**, *10*, 055010.

[152] Stratmann, R. E.; Scuseria, G. E.; Frisch, M. J. An Efficient Implementation of Time-dependent Density-functional Theory for the Calculation of Excitation Energies of Large Molecules; *J. Chem. Phys.* **1998**, *109*, 8218–8224.

[153] Hratchian, H. P.; Schlegel, H. B. Finding minima, transition states, and following reaction pathways on ab initio potential energy surfaces; In *Theory and Applications of Computational Chemistry: The First 40 Years*; Dykstra, C. E., Kim, K. S., Frenking, G., Scuseria, G. E., Eds.; Elsevier, 2005; pp 195–259.

[154] Banerjee, A.; Adams, N.; Simons, J.; Shepard, R. Search for stationary points on surfaces; *J. Phys. Chem.* **1985**, *89*, 52–57.

[155] Simons, J.; Nichols, J. Electronic roles of active site residues in the catalysis and inhibition of carbonic anhydrase; *Int. J. Quant. Chem.* **1990**, *24*, 263–276.

[156] Schlegel, H. B. Geometry Optimization on Potential Energy Surfaces; In *Modern Electronic Structure Theory*; Yarkony, D. R., Ed.; World Scientific: Singapore, 1995; p 459.

[157] Schlegel, H. B. Geometry Optimization; In *Encyclopedia of Computational Chemistry*; Schleyer, P. v. R., Allinger, N. L., Killman, P. A., Clark, T., Schaefer, H. F., Gasteiger, J., Schreiner, P. R., Eds.; Wiley: Chichester, U. K., 1998; Vol. 2; p 1136.

[158] Fletcher, R. *Practical Methods of Optimization;* Wiley: Chichester, U. K., 1981.

[159] Murray, W.; Wright, M. H. *Practical Optimization;* Academic: New York, 1981.

[160] Powell, M. J. D., Ed. *Nonlinear Optimization;* Academic: New York, 1982.

[161] Dennis, J. E.; Schnabel, R. B. *Numerical Methods for Unconstrained Optimization and Nonlinear Equations;* Prentice Hall: Upper Saddle River, New Jersey, 1983.

[162] Scales, L. E. *Introduction to Nonlinear Optimization;* Macmillam: Basingstoke, England, 1985.

[163] Pulay, P. Convergence acceleration of iterative sequences. the case of scf iteration; *Chem. Phys. Lett.* **1980**, *73*, 393–398.

[164] Pulay, P. Improved SCF convergence acceleration; *J. Comput. Chem.* **1982**, *3*, 556–560.

[165] Cances, E.; Bris, C. L. Can we outperform the DIIS approach for electronic structure calculations?; *Int. J. Quant. Chem.* **2000**, *79*, 82–90.

[166] Kudin, K. N.; Scuseria, G. E.; Cances, E. A black-box self-consistent field convergence algorithm: One step closer; *J. Chem. Phys.* **2002**, *116*, 8255–8261.

[167] Li, X.; Millam, J. M.; Scuseria, G. E.; Frisch, M. J.; Schlegel, H. B. Density matrix search using direct inversion in the iterative subspace as a linear scaling alternative to diagonalization in electronic structure calculations; *J. Chem. Phys.* **2003**, *119*, 7651.

[168] Csaszar, P.; Pulay, P. Geometry Optimization by Direct Inversion in the Iterative Subspace; *J. Mol. Struct.* **1984**, *114*, 31–34.

[169] Farkas, Ö.; Schlegel, H. B. Methods for optimizing large molecules - Part III. An improved algorithm for geometry optimization using direct inversion in the iterative subspace (GDIIS); *Phys. Chem. Chem. Phys.* **2002**, *4*, 11–15.

[170] Li, X.; Frisch, M. J. Energy-Represented Direct Inversion in the Iterative Subspace within a Hybrid Geometry Optimization Method; *J. Chem. Theor. Comput.* **2006**, *2*, 835–839.

[171] Moss, C. L.; Li, X. First order simultaneous optimization of molecular geometry and electronic wave function; *J. Chem. Phys.* **2008**, *129*, 114102.

[172] Hirsch, M.; Quapp, W. Improved RGF method to find saddle points; *J. Comput. Chem.* **2002**, *23*, 887–894.

[173] Crehuet, R.; Bofill, J. M.; Anglada, J. M. A new look at the reduced-gradient-following path; *Theor. Chem. Acc.* **2002**, *107*, 130–139.

[174] Simons, J.; Jorgensen, P.; Taylor, H.; Ozment, J. Walking on potential energy surfaces; *J. Phys. Chem.* **1983**, *87*, 2745–2753.

[175] Cerjan, C. J.; Miller, W. H. On finding transition states; *J. Chem. Phys.* **1981**, *75*, 2800–2806.

[176] Nichols, J.; Taylor, H.; Schmidt, P.; Simons, J. Walking on potential energy surfaces; *J. Chem. Phys.* **1990**, *92*, 340–346.

[177] Halgren, T. A.; Lipscomb, W. N. Synchronous-Transit Method for Determining Reaction Pathways and Locating Molecular Transition-States; *Chem. Phys. Lett.* **1977**, *49*, 225–232.

[178] Bell, S.; Crighton, J. S. Locating transition states; *J. Chem. Phys.* **1984**, *80*, 2464–2475.

[179] Peng, C.; Schlegel, H. B. Combining synchronous transit and quasi-newton methods to find transition states; *Israel J. Chem.* **1993**, *33*, 449–454.

[180] Ayala, P. Y.; Schlegel, H. B. A combined method for determining reaction paths, minima, and transition state geometries; *J. Chem. Phys.* **1997**, *107*, 375–384.

[181] Pratt, L. R. A statistical method for identifying transition states in high dimensional problems; *J. Chem. Phys.* **1986**, *85*, 5045–5048.

[182] Elber, R.; Karplus, M. A Method for Determining Reaction Paths in Large Molecules - Application to Myoglobin; *Chem. Phys. Lett.* **1987**, *139*, 375–380.

[183] Henkelman, G.; Uberuaga, B. P.; Jonsson, H. A climbing image nudged elastic band method for finding saddle points and minimum energy paths; *J. Chem. Phys.* **2000**, *113*, 9901–9904.

[184] Henkelman, G.; Jonsson, H. Improved tangent estimate in the nudged elastic band method for finding minimum energy paths and saddle points; *J. Chem. Phys.* **2000**, *113*, 9978–9985.

[185] Maragakis, P.; Andreev, S. A.; Brumer, Y.; Reichman, D. R.; Kaxiras, E. Adaptive nudged elastic band approach for transition state calculation; *J. Chem. Phys.* **2002**, *117*, 4651–4658.

[186] Trygubenko, S. A.; Wales, D. J. A doubly nudged elastic band method for finding transition states; *J. Chem. Phys.* **2004**, *120*, 2082–2094.

[187] Chu, J.-W.; Trout, B. L.; Brooks, B. R. A super-linear minimization scheme for the nudged elastic band method; *J. Chem. Phys.* **2003**, *119*, 12708–12717.

[188] Peters, B.; Heyden, A.; Bell, A. T.; Chakraborty, A. A growing string method for determining transition states: Comparison to the nudged elastic band and string methods; *J. Chem. Phys.* **2004**, *120*, 7877–7886.

[189] Goodrow, A.; Bell, A.; Head-Gordon, M. Development and application of a hybrid method involving interpolation and *ab initio* calculations for the determination of transition states; *J. Chem. Phys.* **2008**, *129*, 174109.

[190] Jensen, F. Using force fields methods for locating transition structures; *J. Chem. Phys.* **2003**, *119*, 8804–8808.

[191] Bofill, J. M. Updated Hessian matrix and the restricted step method for locating transition structures; *J. Comput. Chem.* **1994**, *15*, 1–11.

[192] Uddin, J.; Scuseria, G. E. Theoretical study of ZnO phases using a screened hybrid density functional; *Phys. Rev. B* **2006**, *74*, 245115.

[193] Göpel, W.; Pollmann, J.; Ivanov, I.; Reihl, B. Angle-resolved photoemission from polar and nonpolar zinc oxide surfaces; *Phys. Rev. B* **1982**, *26*, 3144–3150.

[194] Gaussian 09 Revision D.01. Frisch, M. J.; Trucks, G. W.; Schlegel, H. B.; Scuseria, G. E.; Robb, M. A.; Cheeseman, J. R.; Scalmani, G.; Barone, V.; Mennucci, B.; Petersson, G. A.; Nakatsuji, H.; Caricato, M.; Li, X.; Hratchian, H. P.; Izmaylov, A. F.; Bloino, J.; Zheng, G.; Sonnenberg, J. L.; Hada, M.; Ehara, M.; Toyota, K.; Fukuda, R.; Hasegawa, J.; Ishida, M.; Nakajima, T.; Honda, Y.; Kitao, O.; Nakai, H.; Vreven, T.; Jr., J. A. M.; Peralta, J. E.; Ogliaro, F.; Bearpark, M.; Heyd, J. J.; Brothers, E.; Kudin, K. N.; Staroverov, V. N.; Kobayashi, R.; Normand, J.; Raghavachari, K.; Rendell, A.; Burant, J. C.; Iyengar, S. S.; Tomasi, J.; Cossi, M.; Rega, N.; Millam, J. M.; Klene, M.; Knox, J. E.; Cross, J. B.; Bakken, V.; Adamo, C.; Jaramillo, J.; Gomperts, R.; Stratmann, R. E.; Yazyev, O.; Austin, A. J.; Cammi, R.; Pomelli, C.; Ochterski, J. W.; Martin, R. L.; Morokuma, K.; Zakrzewski, V. G.; Voth, G. A.; Salvador, P.; Dannenberg, J. J.; Dapprich, S.; Daniels, A. D.; Farkas, O.; Foresman, J. B.; Ortiz, J. V.; Cioslowski, J.; Fox, D. J.

Appendix A

A PSEUDOHYDROGEN CAPPING SCHEME FOR THE SURFACE PASSIVATION OF QUANTUM DOTS

Experimentally, colloidal quantum dots (QDs) are capped with surface ligands such as dodecylamine (DDA) or trioctylphosphine oxide (TOPO). These ligands prevent the agglomeration of the QD structures into a large mass of material. Computationally, such bulky ligands are intractable due to their long, floppy side chains with many degrees of freedom. However, the need for a surface capping scheme is readily apparent in the electronic structure of an uncapped QD whose geometry is that of the experimentally-determined crystal structure. Such QD structures exhibit unphysical states within their band gap region due to the presence of unpassivated surface charges or dangling bonds. This appendix presents a method for terminating surface dangling bonds and providing a surface capping scheme that yields the correct electronic structure of a QD while having minimal impact on the computational cost.

Figure A.1 shows the density of states (DOS) diagrams for a $Zn_{33}O_{33}$ QD whose geometry is that of the experimentally-determined crystal structure. In the upper panel, the DOS is shown for an uncapped QD, and in the lower panel, the DOS is shown for a pseudohydrogen capped QD. The band gap of these d_{QD} 1.2 nm QDs is expected to be larger than the bulk value of 3.4 eV due to quantum confinement. However, in the uncapped QD, an energy gap in the band structure is not present. Comparing these DOS diagrams to the experimentally measured X-ray photoelectron spectrum (XPS) in Figure A.2 reveals that the uncapped QD's electronic structure does not resemble that of experiment. The pseudohydrogen capped QD shows a band gap of $\sim$6 eV, which is larger than the bulk value as expected. Additionally, the DOS

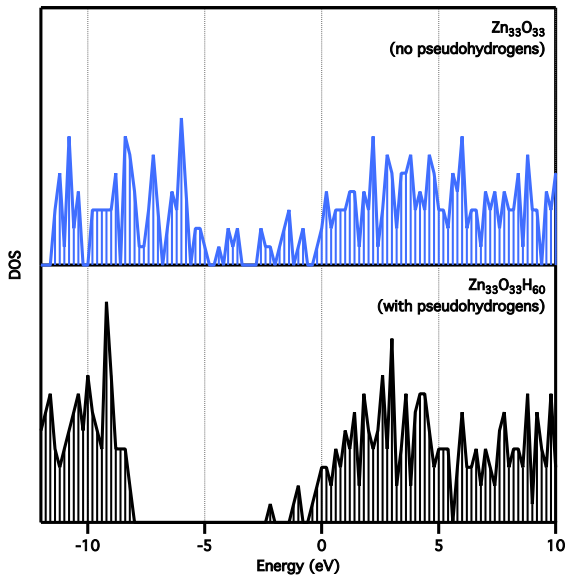

Figure A.1. Density of states (DOS) diagrams for a $Zn_{33}O_{33}$ QD whose surface is not passivated with pseudohydrogen capping ligands (top) and a $Zn_{33}O_{33}$ QD whose surface is completely passivated with pseudohydrogen capping ligands (bottom).

reproduces the XPS spectrum in Figure A.2 with good agreement.

Without allowing the surface states to reorganize themselves via a geometry optimization, the unpassivated surface states place themselves into the band gap of the semiconductor resulting in an unphysical electronic structure. Consequently, a full geometry optimization of the uncapped QD drastically reduces the symmetry, a property often worth maintaining for practical purposes. A full geometry optimization of the pseudohydrogen capped QD results in very little distortion of the QD lattice from the crystal structure with changes in bond lengths and angles of no more than 3% compared to the crystal structure.[90]

Following the work of Wang and Li[92] and Chelikowsky et. al,[91] the pseudohydrogen capping scheme implemented here makes use of simple covalent bond arguments. A tetrahedrally coordinated surface atom with a formal valence charge of m would

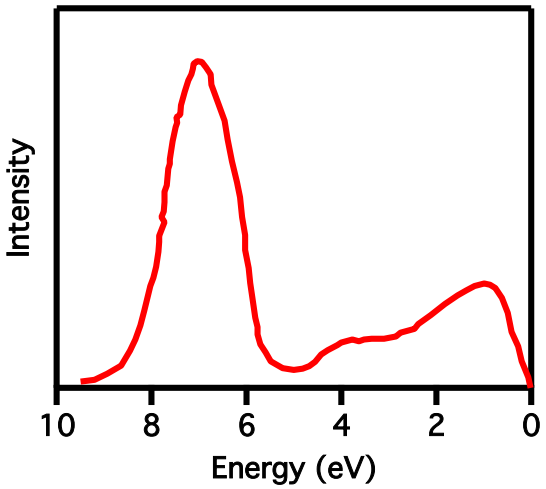

Figure A.2. Experimental photoemission spectrum for bulk ZnO. Adapted from Refs. 192, 193.

contribute $m/4$ electrons to each bond. To terminate each bond, an atom providing $(8-m)/4$ electrons would need to bond with the surface atom. A surface atom with a formal valence of m is bound to a hydrogen atom whose nuclear charge is $q = (8-m)/4$. The values of m and q for the various QD structures considered in this work are summarized in Table A.1 below.

An example calculation involving a Cd_6Se_6 quantum dot structure is presented below. As of Gaussian09 Revision D.01,[194] support for non-integer was implemented via use of the `massage` keyword in the route section and the `znuc` function in the `massage` input. This input must be provided for each atom whose nuclear charge is to be modified and must adhere to the following convention:

`[atom number] znuc [nuclear charge]`,

where `[atom number]` specifies the atom according to the *molecule specification* section, and `[nuclear charge]` is the value of Z for the given atom. Note that the `znuc`

Table A.1. Summary of psedo-hydrogen parameters for QD structures studied in this work.

QD Type	Ion	m	q
CdSe	Cd^{2+}	2	+1.5
	Se^{2-}	6	+0.5
ZnO	Zn^{2+}	2	+1.5
	O^{2-}	6	+0.5
ZnSe	Zn^{2+}	2	+1.5
	Se^{2-}	6	+0.5

function does not modify the number of electrons, thus, care should be taken to ensure that your system maintains its desired overall charge after applying the modified nuclear charges. The Gaussian09 input file for a $Cd_6Se_6H^*_{18}$ QD with pseudohydrogen capping ligands is

```
#p pbe1pbe/lanl2dz massage

zinc oxide quantum dot with pseudohydrogen atoms: Zn6O6H18;

0 1
 Zn01                8.12350000   15.94635700   26.01900000
 Zn02                6.49880000   13.13229400   26.01900000
 Zn03                9.74820000   13.13229400   26.01900000
 Zn04                6.49880000   15.00833600   28.62090000
 Zn05                9.74820000   15.00833600   28.62090000
 Zn06                8.12350000   12.19427300   28.62090000
 O07                 8.12350000   15.94635700   28.00737200
 O08                 6.49880000   13.13229400   28.00737200
 O09                 9.74820000   13.13229400   28.00737200
 O10                 6.49880000   15.00833600   25.40547200
 O11                 9.74820000   15.00833600   25.40547200
 O12                 8.12350000   12.19427300   25.40547200
 H13                 8.12350000   17.56149700   25.45952500
 H14                 5.10031400   12.32465600   25.45914100
```

```
 H15                11.14668600   12.32465600   25.45914100
 H16                 6.40701000   15.06210800   30.31443900
 H17                 5.10356200   15.81200000   28.05558500
 H18                11.14343800   15.81200000   28.05558500
 H19                 9.83999000   15.06210800   30.31443900
 H20                 8.12350000   10.58339400   28.05691900
 H21                 8.12350000   12.08752500   30.31468200
 H22                 8.12350000   16.92884600   28.36263900
 H23                 5.64774600   12.64082600   28.36181700
 H24                10.59925400   12.64082600   28.36181700
 H25                 5.64066900   15.50264100   25.73958400
 H26                 6.43174400   15.04664500   24.36697400
 H27                10.60633100   15.50264100   25.73958400
 H28                 9.81525600   15.04664500   24.36697400
 H29                 8.12350000   12.11960500   24.36673700
 H30                 8.12350000   11.20243100   25.73518500

13 znuc 1.5
14 znuc 1.5
15 znuc 1.5
16 znuc 1.5
17 znuc 1.5
18 znuc 1.5
19 znuc 1.5
20 znuc 1.5
21 znuc 1.5
22 znuc 0.5
23 znuc 0.5
24 znuc 0.5
25 znuc 0.5
26 znuc 0.5
27 znuc 0.5
28 znuc 0.5
29 znuc 0.5
30 znuc 0.5
```

The nuclear repulsion energy obtained for this structure using Gaussian09 Revision D.01 is 1480.56997 hartree and the total electronic energy is −858.63846 hartree.

Appendix B

AN OVERVIEW OF THE DENSITY OF STATES ANALYSIS

The total density of states (DOS) is simply a histogram of molecular orbitals (MOs) whose energy falls within a bin. The energy is plotted along the x-axis and the number of MOs that fall within that energy range are plotted along the y-axis. An example of such a plot is provided in Figure B.1. However, to obtain the partial DOS, a population analysis must be performed. The partial DOS figures presented in this dissertation make use of the Mulliken population analysis. An example of how the Mulliken analysis is used to generate the partial DOS is provided below.

Consider a molecule consisting of atoms A and B each having a $1s$ orbital:

$$A - B. \tag{B.1}$$

For this system, $\left|\phi_{1s}^{A}\right\rangle$ describes the $1s$ atomic orbital (AO) on atom A and $\left|\phi_{1s}^{B}\right\rangle$ describes the $1s$ AO on atom B. One MO to originate from this system would be

$$\left|\psi_1\right\rangle = \frac{1}{\sqrt{2}}\Big(c_1\left|\phi_{1s}^{A}\right\rangle - c_2\left|\phi_{1s}^{B}\right\rangle\Big), \tag{B.2}$$

where c_1 and c_2 are the MO coefficients. The overlap integral of this MO is

$$\begin{aligned}\left\langle\psi_1 \mid \psi_1\right\rangle &= \frac{1}{2}\Big(c_1^{*}\left\langle\phi_{1s}^{A}\right| - c_2^{*}\left\langle\phi_{1s}^{B}\right|\Big)\Big(c_1\left|\phi_{1s}^{A}\right\rangle - c_2\left|\phi_{1s}^{B}\right\rangle\Big) \\ &= \frac{1}{2}\Big(|c_1|^2\left\langle\phi_{1s}^{A} \mid \phi_{1s}^{A}\right\rangle + |c_2|^2\left\langle\phi_{1s}^{B} \mid \phi_{1s}^{B}\right\rangle - c_1^{*}c_2\left\langle\phi_{1s}^{A} \mid \phi_{1s}^{B}\right\rangle - c_2^{*}c_1\left\langle\phi_{1s}^{B} \mid \phi_{1s}^{A}\right\rangle\Big),\end{aligned} \tag{B.3}$$

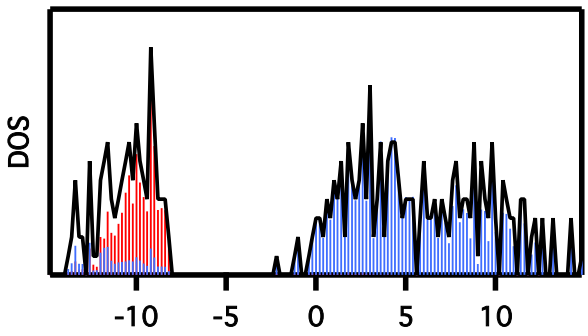

Figure B.1. Density of states (DOS) diagram for a $Zn_{33}O_{33}$ QD showing the partial DOS analysis: Zn^{2+} s, p, d in blue, O^{2-} s, p in red.

where $\langle \phi_{1s}^{A} \mid \phi_{1s}^{A} \rangle$, $\langle \phi_{1s}^{B} \mid \phi_{1s}^{B} \rangle$, $\langle \phi_{1s}^{A} \mid \phi_{1s}^{B} \rangle$, and $\langle \phi_{1s}^{B} \mid \phi_{1s}^{A} \rangle$ are overlap matrix elements. The contribution of atom A's $1s$ AO to the first MO is obtained by summing together the following terms:

$$f_{\psi_1}^{A_{1s}} = \frac{1}{2}\Big(|c_1|^2 \langle \phi_{1s}^{A} \mid \phi_{1s}^{A} \rangle + \frac{1}{2} c_1^* c_2 \langle \phi_{1s}^{A} \mid \phi_{1s}^{B} \rangle - \frac{1}{2} c_2^* c_1 \langle \phi_{1s}^{B} \mid \phi_{1s}^{A} \rangle \Big), \tag{B.4}$$

where the Mulliken analysis assumes that the contribution of the cross terms can be divided equally with half originating from atom A and the other half originating from atom B. Similarly, for the contribution from atom B,

$$f_{\psi_1}^{B_{1s}} = \frac{1}{2}\Big(|c_2|^2 \langle \phi_{1s}^{B} \mid \phi_{1s}^{B} \rangle + \frac{1}{2} c_1^* c_2 \langle \phi_{1s}^{A} \mid \phi_{1s}^{B} \rangle - \frac{1}{2} c_2^* c_1 \langle \phi_{1s}^{B} \mid \phi_{1s}^{A} \rangle \Big). \tag{B.5}$$

The partial DOS is then generated by summing the contribution of a given AO type for all MOs in the specified energy bin and plotting count (f) versus energy.

Appendix C

PARTICLE IN A SPHERICAL POTENTIAL

According the the Brus model,[40–42] the wave function of a conduction band electron may be approximated using the particle in a spherical potential model. In this model, the Hamiltonian is given in spherical polar coordinates as

$$-\frac{\hbar^2}{2m_e}\left[\frac{1}{r^2}\frac{\partial}{\partial r}\left(r^2\frac{\partial\psi}{\partial r}\right)+\frac{1}{r^2\sin\theta}\frac{\partial}{\partial\theta}\left(\sin\theta\frac{\partial\psi}{\partial\theta}\right)+\frac{1}{r^2\sin^2\theta}\left(\frac{\partial^2\psi}{\partial\phi^2}\right)\right]+V\psi=E\psi. \tag{C.1}$$

Solutions to this equation when $V=0$ for $r<R$ and $V=\infty$ for $r>R$ (R being the radius of the spherical potential) consist of a radial and angular component

$$\psi_{n\ell m}(r,\theta,\phi)=A_{n\ell}j_\ell(\beta_{n\ell}r/R)Y_\ell^m(\theta,\phi), \tag{C.2}$$

where $A_{n\ell}$ is a normalization constant, j_ℓ is the ℓ-th spherical Bessel function of the first kind, and $\beta_{n\ell}$ is the n-th zero of the ℓ-th spherical Bessel function (these zeros can only be determined numerically). The energy eigenvalues are given by

$$E_{n\ell}=\frac{\beta_{n\ell}\hbar^2}{m_eR^2}. \tag{C.3}$$

Due to the boundary conditions

$$\begin{aligned} n&=1,2,\ldots\\ \ell&=0,1,2,\ldots\\ m&=-\ell,-\ell+1,\ldots,0,\ldots,\ell-1,\ell, \end{aligned} \tag{C.4}$$

that is, ℓ runs independently of n unlike in the case of the hydrogen atom. Wave functions and energy eigenvalues for the first few quantum states are provided in Table C.1.

n	ℓ	m	$A_{n\ell}$	$j_\ell(r)$	$\beta_{n\ell}$	$Y_\ell^m(\theta,\phi)$	$E_{n\ell}$ $(\hbar^2/m_eR^2)$
1	0	0	$\frac{1}{\sqrt{2\pi R}}$	$\frac{\sin(r)}{r}$	π	$\left(\frac{1}{4\pi}\right)^{\frac{1}{2}}$	4.93480
1	1	0	$\frac{6.51010}{R^{3/2}}$	$\frac{\sin(r)}{r^2} - \frac{\cos(r)}{r}$	4.49341	$\left(\frac{3}{4\pi}\right)^{\frac{1}{2}} \cos\theta$	10.09537
1	1	±1				$\mp\left(\frac{3}{8\pi}\right)^{\frac{1}{2}} \sin\theta e^{\pm i\phi}$	
1	2	0				$\left(\frac{5}{16\pi}\right)^{\frac{1}{2}} (3\cos^2\theta - 1)$	
1	2	±1	$\frac{8.54265}{R^{3/2}}$	$\left(\frac{3}{r^3} - \frac{1}{r}\right)\sin(r) - \frac{3}{r^2}\cos(r)$	5.76346	$\mp\left(\frac{15}{8\pi}\right)^{\frac{1}{2}} \sin\theta\cos\theta e^{\pm i\phi}$	16.60874
1	2	±2				$\mp\left(\frac{15}{32\pi}\right)^{\frac{1}{2}} \sin^2\theta e^{\pm 2i\phi}$	
2	0	0	$\frac{1}{\sqrt{2\pi R}}$	$\frac{\sin(r)}{r}$	2π	$\left(\frac{1}{4\pi}\right)^{\frac{1}{2}}$	19.73921
2	1	0	$\frac{11.01631}{R^{3/2}}$	$\frac{\sin(r)}{r^2} - \frac{\cos(r)}{r}$	7.72525	$\left(\frac{3}{4\pi}\right)^{\frac{1}{2}} \cos\theta$	29.83974
2	1	±1				$\mp\left(\frac{3}{8\pi}\right)^{\frac{1}{2}} \sin\theta e^{\pm i\phi}$	

Table C.1. Wave functions for the first few conduction band electrons in a spherical nanostructure. The wave function is constructed according to Equation (C.2) and the energy is calculated using Equation (C.3).

VITA

Joseph W. May was born in Phoenix, AZ in 1987. In 2002, he moved with his family to Central Point, OR, where he completed his high school education. In 2009, he earned a bachelor of science degree in biochemistry *magna cum laude* from Southern Oregon University in Ashland, OR. Afterwards, he joined the research lab of Professor Xiaosong Li in 2009 at the University of Washington, where he earned a doctor of philosophy in chemistry in 2014.